

A Dissertation

entitled

Physically/Electrically Enhanced Microwave & Millimeter Wave Front-ends
with Modern Manufacturing Technologies

by

Osama Hussein

Submitted to the Graduate Faculty as partial fulfillment of the requirements for the
Doctor of Philosophy Degree in Engineering

Dr. Vijay Devabhaktuni, Committee Chair

Dr. Khair Al Shamaileh, Committee Member

Dr. Daniel Georgiev, Committee Member

Dr. Raghav Khanna, Committee Member

Dr. Junghwan Kim, Committee Member

Dr. Amanda C. Bryant-Friedrich, Dean
College of Graduate Studies

The University of Toledo

August 2020

Copyright 2020, Osama Hussein

This document is copyrighted material. Under copyright law, no parts of this document may be reproduced without the expressed permission of the author.

An Abstract of
Physically/Electrically Enhanced Microwave & Millimeter Wave Front-ends
with Modern Manufacturing Technologies

by
Osama Hussein

Submitted to the Graduate Faculty as partial fulfillment of the requirements for the
Doctor of Philosophy Degree in Engineering

The University of Toledo
August 2020

The growing demand toward designing miniaturized microwave and millimeter wave (mm-wave) front-ends with enhanced electrical performance (e.g., low losses, wideband functionality, high selectivity, etc.) is becoming of utmost importance. In addition, enabling functionalities such as selection/rejection of specific frequency channels (i.e., filtering), power division, and amplification is essential for any wireless system. This dissertation proposes new design methodologies for various front-ends using different manufacturing technologies. The proposed designs are verified by full-wave EM simulations and experimental results of passive front-ends at microwave and millimeter wave frequencies. The aim is to enhance their electrical and physical characteristics without degrading their intended performance. The developed designs are essential to the upcoming wireless technologies such as fifth generation (5G) mobile communication and satellite systems.

The first proposed component is a substrate integrated waveguide (SIW) bandpass filter (BPF). The design procedure starts by varying the width between the metallic walls of via-holes according to a truncated Fourier series to achieve a desired pass-band/stopband performance. The theory of rectangular waveguide is used to establish the optimization framework and obtain the series coefficients under predefined physical constraints. Two types of end-terminations are studied, namely, with and without

SIW-to-microstrip transitions. The proposed design methodology is systematic and results in single-layered structures. For verification purposes, several Ku-band BPFs with different fractional bandwidths (FBWs) are designed, simulated, and measured. Simulated and measured results are in close proximity with passband matching and transmission losses better than -15 dB and -2.5 dB, respectively. The proposed methodology allows for designing BPFs with predefined wideband or narrowband functionality by modifying the underlying physical constraints and optimization parameters.

The second proposed component is a highly-selective SIW filtering Wilkinson power divider (WPD). The design procedure is accomplished by replacing the uniform transmission lines in each arm of the conventional divider with width-varied arms governed by a truncated Fourier series. Even-mode analysis is adopted to obtain the Fourier-varying transmission lines with predefined bandwidth; whereas three isolation resistors are optimized in the odd-mode analysis to achieve proper isolation and output ports matching over the frequency range of interest. The half-mode (HM) SIW structure is used to cut the PD size by 50%. For verification purposes, a 2-way equal-split filtering WPD is designed and simulated. The obtained results show that the input and output ports matching as well as the isolation between the output ports are below -13 dB; whereas the transmission parameters are around -6 dB across the operating band. Such results adjoined with compact size show that the proposed PD will be a competitive candidate for microwave and millimeter wave application.

Next, an impedance-varying multi-way microstrip WPD with bandwidth redefinition characteristics is proposed. The microstrip WPD finds many applications due to its convenient electrical performance, which is characterized by high isolation between its output ports and perfect matching at all ports. However, such performance is realized only at a very small fraction of bandwidth. Hence, the proposed impedance-varying WPD aims to broaden the bandwidth without increasing the circuitry size

or fabrication complexity. Quarter-wave matching uniform transmission lines in the conventional design are replaced with non-uniform transmission lines (NTLs) governed by a truncated Fourier series. Compactness is achieved by incorporating only one quarter-wave wideband NTL transformer, with a length computed at the center frequency, in each arm. For verification purposes, 3- and 4-way WPDs are designed and simulated. In addition, a wideband 3-way WPD operating over 4–10 GHz band is fabricated and measured. Results show input and output ports matching and isolation below -15 dB, and transmission parameters in the range of $[-4.9, -6.2]$ dB across the operating band of the 3-way and WPD.

The last proposed component is a miniaturized coplanar waveguide (CPW) matching transformers implemented on flexible substrates. The signal trace and the adjacent ground planes in the conventional CPW structure are width-modulated along the propagation path of the electromagnetic wave while maintaining a constant ground-trace separation. Validation is carried out by designing and simulating single-, multi-, and wide-band transformers operating at 1.0 GHz, 0.9, 3.6, 5.4 GHz, and 1–3 GHz, respectively. Full-wave simulation results verify the proposed design procedure which show input port matching values below -23 dB for single- and multi-frequency transformers, whereas they are below -15 dB for the wideband one. In addition, insertion losses are better than -0.25 dB for all designed transformers.

The proposed designs are targeting the less congested higher frequency bands, specifically, super high frequency (SHF) band. Moving toward higher frequencies enables higher data rates, supports more connected wireless devices, and leads to more miniaturized front-ends.

For my parents and my wife

Acknowledgments

I would like to thank my advisor, Prof. Vijay Devabhaktuni, for his continuous support and recommendations that led this research to a successful conclusion.

I wish to show my gratitude to my friend and co-advisor Dr. Khair Al shamileh for his persistent help and support during my Ph.D. journey.

I am very grateful to Prof. Nihad Dib for his expert assistance and fruitful discussions throughout the course of this research.

Also, I want to thank all my friends and colleagues in the computer-aided design (CAD) lab at the University of Toledo for their support and encouragement throughout my degree.

Finally, my deepest gratitude to my parents, my siblings, and my wife for their support, patience, and love. They kept me going on and this work would not have been possible without their unconditional support.

Contents

Abstract	iii
Acknowledgments	vii
Contents	viii
List of Tables	xi
List of Figures	xii
List of Abbreviations	xvi
List of Symbols	xviii
1 Introduction	1
1.1 Research Challenges and Motivation	1
1.1.1 Bandpass Filters	3
1.1.2 Power Dividers/Combiners	4
1.1.3 Transmission Line Mediums for Microwave and Millimeter-wave Applications	5
1.2 Research Objectives and Contributions	7
1.3 Literature Review	8
1.3.1 Progress in SIW Filters	9
1.3.2 Progress in SIW Power Dividers	10
1.3.3 Progress in Wideband Microstrip WPDs	12

1.3.4	Progress in Front-ends on Flexible Substrates	13
1.4	Organization	13
2	E-wall Varied SIW Bandpass Filters	15
2.1	Operation Principles	16
2.1.1	Frequency Region of Interest	19
2.2	E-wall varied SIW transmission lines Design	20
2.3	SIW Bandpass Filtering with Fourier-varying Via-hole Walling	27
2.3.1	Filter Design without Matching Networks	27
2.3.2	Filter Design with Klopfenstein Matching Network	30
2.4	Simulations and Measurements	32
2.5	Conclusion	36
3	E-wall Varied HMSIW Filtering Wilkinson Power Divider	38
3.1	WPD Design	39
3.1.1	Even-odd Analysis	39
3.1.2	Odd-odd Analysis	41
3.2	Results	42
3.3	Conclusion	44
4	Impedance-varying N-way Microstrip Wilkinson Power Divider	47
4.1	N -way Microstrip WPD Design	48
4.1.1	Even-mode Analysis	49
4.1.2	Odd-mode Analysis	52
4.2	Results	54
4.2.1	Analytical Results	54
4.2.2	Simulations and Measurements	57
4.3	Conclusions	60

5 Coplanar Waveguide Transformers for RF Circuitries on Flexible Substrates	64
5.1 CPW Matching Transformers Design	65
5.2 Results	68
5.3 Conclusion	70
6 Conclusions and Future Work	71
6.1 Summary	71
6.2 Impact on Different Disciplines	74
6.3 Future Work	76
6.4 Research Publications and Outcomes	79
References	80
A Losses in Microstrip, CPW, and SIW lines	96
B Quality Factor Calculations	101

List of Tables

2.1	List of Optimization Parameters	29
2.2	List of Physical Dimensions of the SIW BPFs	29
2.3	Optimized Fourier Series Coefficients and the Corresponding Objective Function Error Value	36
2.4	Comparison between the Proposed BPFs and Other State-of-the-art SIW BPFs	37
3.1	Optimized Fourier Series Coefficients and the Corresponding Objective Function Error Value	41
3.2	List of Physical Dimensions of the HMSIW WPD	43
3.3	Comparison between the Proposed filtering PD and Other State-of-the-art SIW PDs	46
4.1	Fourier Coefficients for the Impedance-varying Profiles of Three 3-Way WPD Examples	56
4.2	Fourier Coefficients for the Impedance-varying Profiles of Three 4-Way WPD Examples	56
4.3	Comparison between Electrical and Physical properties of the Proposed NTLs N -Way WPDs and recent Wideband Power Dividers	63

List of Figures

1-1	A block diagram of a basic superheterodyne receiver. Blue modules represents the RF front-end part.	2
1-2	Cell phone RF front-end modules market: 2016 – 2022 [2].	3
1-3	A schematic diagram of a conventional SIW transmission line.	6
1-4	Applications enabled by using flexible substrates: (a) foldable smartphone, (b) communication PCB, and (c) wearable monitoring device [10]	7
2-1	A schematic diagram of a conventional SIW structure.	16
2-2	Frequency Region of interest for the SIW in the plane of d/λ_c and s/λ_c [69].	20
2-3	A schematic diagram of the proposed SIW-based structure with varying via-hole walling without SIW-to-microstrip transitions. White, grey and black colors represent the substrate, metal and via-holes, respectively. . .	21
2-4	A schematic diagram of the proposed SIW-based structure with varying via-hole walling with SIW-to-microstrip transitions. White, grey and black colors represent the substrate, metal and via-holes, respectively.	21
2-5	S -parameters of a conventional SIW structure: (a) without SIW-to-microstrip transition, and (b) with a Klopfenstein tapered SIW-to-microstrip transition.	22
2-6	Cutoff frequency and width variations at the center of each SIW segment vs. physical length. Solid blue and dotted red represent f_c and $w_{eff(x)}/2$, respectively.	23
2-7	Simulated versus analytical Z_0 based on expressions (2.13) and (2.19) plotted for different w_{eff} and h (units in mm).	26

2-8	Analytical results of three SIW-based BPFs with different passbands. Blue dotted, red dashed, and green solid lines represent passbands of 13.8–14.2 GHz, 13.5–14.5 GHz, and 12.5–15.5 GHz, respectively.	30
2-9	Width-varying profiles of the BPFs as a function of the normalized length.	31
2-10	Width-varying profiles of the BPFs as a function of the normalized length.	31
2-11	Simulations and measurement of the designed SIW-based BPF with a FBW of 5.8% and 14 GHz center frequency.	33
2-12	Simulations and measurement of the designed SIW-based BPF with a FBW of 2.5% and 12 GHz center frequency.	34
2-13	Simulations and measurements of the designed HMSIW-based BPF with a FBW of 2.5% and 12 GHz center frequency	35
2-14	Photographs of the three fabricated BPFs: (a) prototype 1, (b) prototype 2, and (c) prototype 3.	35
3-1	A schematic diagram of the proposed HMSIW-based WPD with varying via-hole walling. White, grey, black and brown colors represent the substrate, metal, via-holes, and isolation resistors, respectively.	39
3-2	The equivalent even-mode circuit of the proposed SIW WPD.	40
3-3	The equivalent odd-mode circuit of the proposed SIW WPD.	41
3-4	Simulated S -Parameters of the designed HMSIW-based filtering PD: (a) S_{11} and S_{21} and (b) S_{22} and S_{23}	43
3-5	Simulated layout of the designed HMSIW-based PD: (a) top view and (b) trimetric view.	44
4-1	Schematic diagrams of N -way WPDs: (a) conventional single-frequency and (b) proposed wideband.	48
4-2	2-way equivalent model of the N -way WPD.	49
4-3	2-way equivalent even-mode circuit of the proposed NTL N -way WPD.	50

4-4	2-way equivalent odd-mode circuit of the proposed NTL N -way WPD. . .	53
4-5	S-parameters (S_{11} and S_{21}) for the wideband NTL matching transformers across the design bands 6-8 GHz, 5-9 GHz, and 4-10 GHz: (a) 3-way case: $Z_s = 150\Omega$, $Z_l = 70.71\Omega$, and (b) 4-way case: $Z_s = 200\Omega$, $Z_l = 86.6\Omega$. . .	55
4-6	Simulated S -parameters of the wideband 3-way WPD with FBW of 57%: (a) input port matching and transmission parameters, and (b) output port matching and isolation parameters.	58
4-7	Simulated S -parameters of the proposed 4-way WPD with a FBW of 57%: (a) input port matching and transmission parameters and (b) output port matching and isolation parameters.	59
4-8	Photograph of the fabricated 3-way WPD structure operating over a band of 4–10 GHz.	60
4-9	Simulated and measured S -parameters of the 3-way WPD with FBW of 86%.	61
4-10	Simulated and measured results of: (a) output ports matching, and (b) isolation of the proposed wideband 3-way WPD.	61
4-11	Measured imbalance of the proposed wideband 3-way WPD: (a) magnitude and (b) phase.	62
4-12	Measured group delays of the proposed 3-way WPD over the 4-10 GHz band.	62
5-1	A CPW impedance matching transformer that matches a load impedance, Z_l , to a source impedance, Z_s : (a) conventional and (b) proposed miniaturized transformers.	65
5-2	Analytical and simulated S -parameters for the single-frequency transformer operating at 1 GHz: (a) S_{11} (b) S_{21}	69

5-3	Analytical and simulated S -parameters for the multi-frequency transformer operating at 0.9, 3.6, 5.4 GHz: (a) S_{11} (b) S_{21}	69
5-4	Analytical and simulated S -parameters for the wideband transformer operating over 1–3 GHz band: (a) S_{11} (b) S_{21}	70
5-5	Signal trace of the proposed transformers: (a) single-frequency, (b) multi-frequency, and (c) wideband.	70
A-1	A schematic diagram of a microstrip line.	96
A-2	A schematic diagram of a CPW.	97
A-3	A schematic diagram of a SIW structure.	99

List of Abbreviations

BPF	bandpass filter
CPW	coplanar waveguide
CSSR	complementary S-shaped resonator
EBG	electromagnetic band-gap
EM	electromagnetic
FBW	fractional bandwidth
GA	genetic algorithm
GPS	global positioning system
HM	Half-mode
HFSS	high frequency structural simulator
IC	integrated circuit
LCP	liquid crystal polymer
LNA	low noise amplifier
MIMO	multiple-input-multiple-output
mm-wave	millimeter wave
LTCC	low temperature co-fired ceramic
NTL	non-uniform transmission line
PA	power amplifier
PCB	printed circuit board
PC	Power combiner
PD	Power divider
Q-factor	quality factor

RF	radio frequency
RWG	rectangular waveguide
SHF	super high frequency
SIC	substrate integrated circuit
SiP	system in package
SIW	substrate integrated waveguide
SMA	subminiature version A
SOLT	short-open-load-thru
<i>S</i> -parameter	scattering parameter
STEM	science, technology, engineering, and math
TE	transverse electric
TEM	transverse electromagnetic
TM	transverse magnetic
VNA	vector network analyzer
WPD	Wilkinson power divider

List of Symbols

α	attenuation constant
β	phase constant
γ	propagation constant
Γ	reflection coefficient
Z_0	characteristic impedance
ϵ	permittivity
μ	permeability
c	speed of light
λ	wavelength
λ_g	guided wavelength
θ	electrical length of a transmission line

Chapter 1

Introduction

With an unprecedented increase of wireless devices' users and their demanding expectations, new compact devices supporting higher data rates must be adopted. Thus, moving toward higher frequencies is indispensable. In the United States, 28.58 trillion megabytes were consumed in 2018, which represents a 82% growth in wireless data consumption compared to 2017 [1]. In addition, 21.5 million new wireless devices were connected to the internet in 2018, which raises the total number of connected devices to 421.7 million [1]. This tremendous surge in connected devices and their data usage, place the onus on RF front-ends designers to build front-ends with compact size, low cost, low loss, and easy integration with other components. Moving toward higher frequency bands, such as super high frequency (SHF) addresses the aforementioned challenges. Specifically, it has the following advantages: 1) supports higher data rates because more bandwidth is available, 2) reduces the interference due to less congestion in these bands, and 3) offers smaller physical area as the size of radio-frequency (RF) components is inversely proportional to the operating frequency.

1.1 Research Challenges and Motivation

With an unprecedented increase of wireless devices' users and their demanding expectations, new compact devices supporting higher data rates must be adopted.

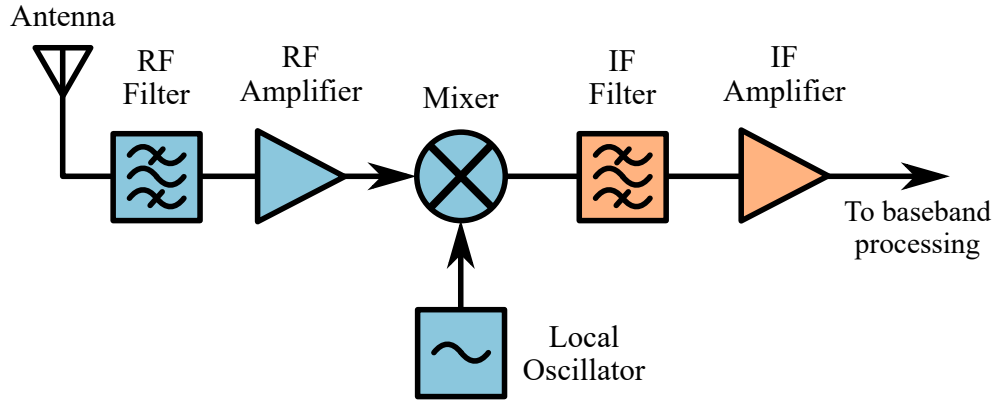


Figure 1-1: A block diagram of a basic superheterodyne receiver. Blue modules represents the RF front-end part.

Thus, moving toward higher frequencies is indispensable. In the United States, 28.58 trillion megabytes were consumed in 2018, which represents a 82% growth in wireless data consumption compared to 2017 [1]. In addition, 21.5 m

The continual growth of connected mobile devices and their data usage have led to more use of the radio spectrum, which causes spectrum scarcity. In order to face this surge demand, modern RF and microwave front-ends should be realized with innovative designs. Such innovations can come from three different sources [2]: 1) Design; by introducing high performance RF components with flexible and cost efficient designs at mm-wave frequency bands. Dual-band front-end modules and filtering power amplifiers/dividers are examples for such designs. 2) Architecture; by combining the functions of several components on a single miniaturized module for system-in-package (SiP) integration. 3) Materials; by developing low-cost mass-producible substrates such as flexible substrates which are excellent candidates for new generations of flexible electronics and 5G applications.

Figure 1-1 illustrates the front-end modules of a basic superheterodyne receiver. These components provide most of the analog signal processing including signal filtering, amplification, and demodulation. In the following subsections, an in-depth discussion on the design challenges of front-ends is presented.

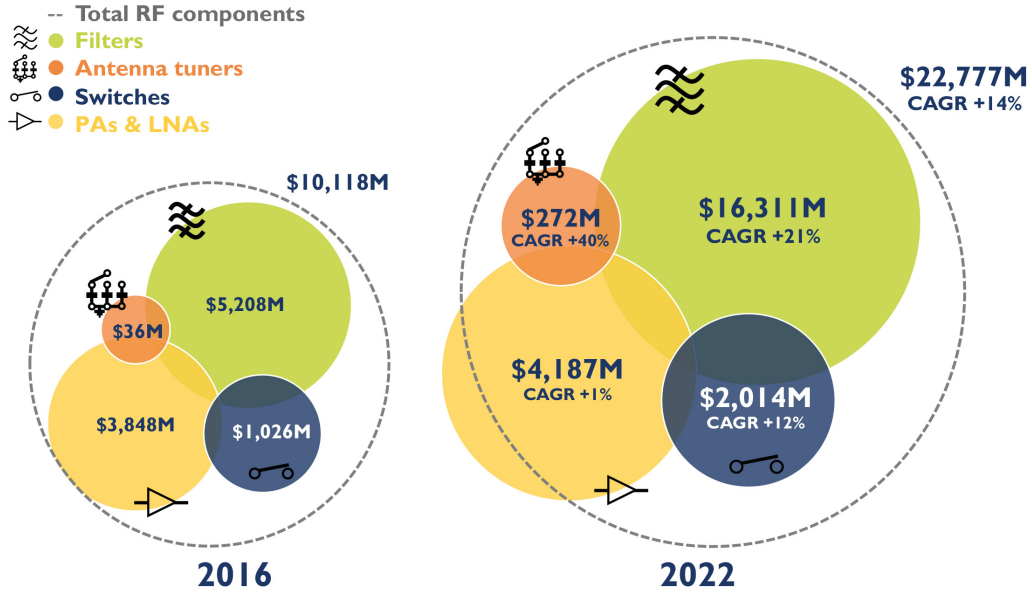


Figure 1-2: Cell phone RF front-end modules market: 2016 – 2022 [2].

1.1.1 Bandpass Filters

Figure 1-2 shows the RF component and front-end module market of 2016 and forecast of 2022 [2]. It can be clearly seen that RF filters are the mostly used components in the RF front-end industry in 2016 representing 51% of the total RF front-ends market of cell phones. Furthermore, RF filters are expected to have a compound annual growth rate of 21% in 2022. This is understandable since such filters enable the desired signals to be selected and unwanted ones to be removed. In addition, as a result of the over crowded EM spectrum, highly selective bandpass filters (BPFs) are essential for future generations of the wireless communication systems. Thus, increasingly sophisticated RF, microwave, and mm-wave BPFs are required to enable the selection/rejection of specific frequency bands. BPFs have been the most useful and popular types for such applications and are the most difficult to design and develop in practice [3]. These challenges have motivated us to design enhanced microwave and mm-wave BPFs.

1.1.2 Power Dividers/Combiners

Power dividers/combiners (PDs/PCs) are widely used fundamental front-end components in a variety of microwave and mm-wave systems where splitting an input signal into smaller signals or combining signals from several ports are necessary. They are widely used in power amplifiers (PAs), mixers, and antenna arrays which are essential modules of any wireless system. It can be seen from Figure 1-2 that PAs and low noise amplifiers (LNAs) represent the second biggest segment with 38% of the total RF cell phone market. The PAs have limitations especially when a high amplification gain is required. To overcome this, a PC is used to combine the individual powers from multiple lower power PAs. Such network has the advantages of: 1) better reliability by avoiding total loss of the transceiver's power in the case of the failure of a single PA [4], 2) less expensive and complex to manufacture moderate-power PAs than high-power PAs, and 3) lower power PAs can be biased to operate in the linear region, resulting in the reduction of the intermodulation distortion and undesired harmonics.

In order to design high performance PDs/PCs for next generation front-ends, high ports matching, low insertion loss, and amplitude and phase balance between the divider's arms as well as to compactness and cost-effectiveness should be fulfilled. The common techniques that serve for this purpose are based on cavities, resonators, or electromagnetic band-gaps (EBGs). However, this comes at the cost of higher passband losses and/or larger physical area. Furthermore, if the structure will be used as a power combiner, the most important specification is the isolation between its output ports. This justifies the extensive use of Wilkinson power dividers/combiners (WPDs/WPCs) which offer high isolation between the output ports due to the use of the resistor. Motivated by the aforementioned challenges, a Ku-band SIW-based filtering power divider and several wideband microstrip-based multi-way WPDs are

designed and optimized.

1.1.3 Transmission Line Mediums for Microwave and Millimeter-wave Applications

One of the key requirements of next generation RF front-ends is the ability to integrate them on a single chip. Compact size, high performance, and low cost of the RF components are necessary to achieve an efficient integration. Hence, choosing the appropriate transmission line is of utmost importance. Based on the operating frequency and fractional bandwidth (FBW), a rectangular waveguide, planar structure (e.g. microstrip, coplanar waveguide), coaxial cable, or a hybrid form of these different technologies can be used. For low cost and compact size applications, planar transmission lines are the winner. On the other hand, the bulky and expensive waveguides are used for applications that require high quality factor (Q-factor), low losses, and high power handling. Hence, introducing a new transmission line that combines the advantages of planar transmission lines and the waveguides is highly desirable. This has led to the development of the concept of substrate integrated circuits (SICs), which allows constructing a nonplanar structure in a planar form [5]. The SICs scheme provides a variety of integration topological interconnects, such as the popular substrate integrated waveguide (SIW), which is a transformed version from the bulky nonplanar waveguide. Thus, the SIW structure can be easily integrated into any planar structure with any planar fabrication technique such as printed circuit board (PCB) and low-temperature co-fired ceramic (LTCC) technologies. This emerging structure can be made with a pair of periodic metallic via-holes that have a specific spacing in which EM waves will be confined as shown in Figure 1-3.

Such SIW structures can mostly preserve the advantages of rectangular waveguides such as high Q-factor and high power capacity. Thus, SIW is one of the best

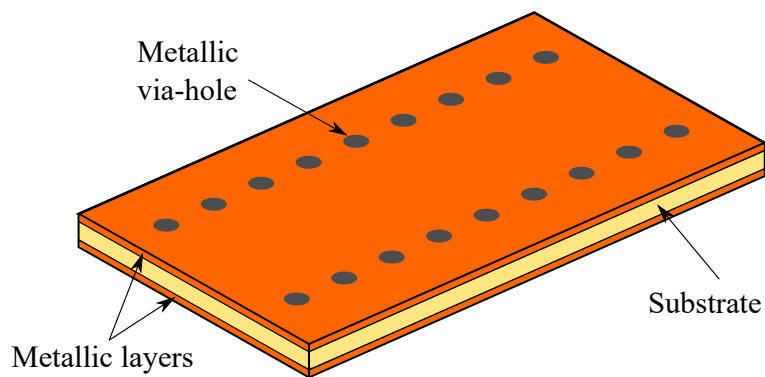


Figure 1-3: A schematic diagram of a conventional SIW transmission line.

candidates for high performance and low cost microwave and mm-wave applications.

In addition to the aforementioned advantages, SIW technology enables the possibility to integrate passive and active components on the same substrate. Thus, facilitating its use for SiP integration [6]. The SiP has several advantages such as reducing the overall size, cost, and production time of the integrated subsystem as well as enabling better electrical performance.

Furthermore, flexible substrates have been used recently for many RF and microwave applications, such as wearable microwave imaging devices, biomedical radars, and ink-jet printed circuits [7–9]. The major advantage of using flexible substrates is their ability to be bent or folded which is a key requirement for some applications such as foldable smartphones and wearable monitoring devices as shown in Figure 1-4 [10]. In addition, they can significantly reduce the weight and size of such devices compared to rigid substrates. Among the flexible substrates, liquid crystal polymer (LCP) gained special attention as a great microwave and mm-wave substrate due to its excellent performance at high frequencies, characterized by the low loss, near hermetic nature, and low cost [11].

well as compact and planar structures.

4. Proposed a novel approach to design compact CPW matching transformers for the implementation on flexible liquid crystal polymer (LCP) substrate. The proposed transformers match predefined source and load impedances at single-, multi-, and wide-band frequency bands.

The developed structures are justified analytically and by professional full-wave EM simulations. Moreover, the proposed designs are further validated by means of fabrications and measurements.

1.3 Literature Review

As mentioned earlier, filters and power dividers/combiners are essential components in almost any front-end RF, microwave, and mm-wave systems such as global positioning system (GPS), fourth and fifth generation cellular networks (4&5G) as well as satellite and radar systems [12–17]. Hence, improved their electrical characteristics without increasing the associated fabrication complexity and size are ongoing research topics. This section presents a literature survey on the front-ends proposed in this dissertation. Section 1.3.1 presents the progress in SIW-based BPFs and describes the recent reported methods that were utilized to obtain such performance. State-of-the-art techniques to design SIW PDs are investigated in Section 1.3.2 in which their advantages and disadvantages are discussed. Section 1.3.3 presents the progress in wideband WPDs based on microstrip lines. Finally, front-ends designed on flexible substrates are introduced in Section 1.3.4.

1.3.1 Progress in SIW Filters

Low cost, compactness, high performance, and mass-producible are the main requirements of modern microwave and millimeter wave systems. In spite of high Q-factor and low losses of the rectangular waveguide, its bulky size as well as tedious and expensive fabrication and assembly limit its application in modern wireless systems. Thus, the SIW, which intertwines the advantages of planar and nonplanar structures, is a favorable candidate for designing microwave and mm-wave front-ends. BPFs have been widely used in many microwave and mm-wave systems [18–21]. SIW-based BPFs, in particular, have attracted a special attention for their contribution in eliminating unwanted transverse-magnetic (TM) propagation modes and out-of-band parasitic responses [3]. Consequently, efforts have been devoted towards developing SIW BPFs with improved electrical properties (e.g., low passband losses, high selectivity) without compromising the physical dimensions and fabrication complexity.

The most common techniques to design SIW-based BPFs is by combining the high-pass characteristics of the SIW structure and the bandstop characteristics of cavities, resonators or EBG. In [22], a planar SIW BPF was proposed by incorporating four SIW cavities fed by 50- Ω microstrip lines. Good passband performance was achieved but upper stopband rejection was achieved over a narrow bandwidth. Chen *et al.* proposed a BPF based on stacked SIW cavities based on LTCC substrates [23]. Although excellent frequency selectivity and wide stopband were obtained, this comes at the expense of increasing fabrication complexity and manufacturing precision. Higher-order modes of cavities were used to achieve wide stopband and dual-band BPFs in [24, 25]. Furthermore, various types of resonators were used to attain bandpass characteristics and introduce transmission zeros in [26–28]. Nevertheless, the resulting physical area, high insertion losses and/or poor stopband rejection were major drawbacks.

In [29], a novel spoof surface plasmon polariton was adopted in the design of

a broadband SIW filter. The bandpass response was realized by means of lowpass characteristics of spoof surface plasmon polariton and the high-pass feature of the SIW. However, the associated structural complexity and stopband characteristics setback its ready acceptance. A trisection filter with a frequency-dependent cross-coupling was proposed in [30]. However, frequency matching was achieved at the expense of the stopband rejection level and passband insertion loss. Folded SIW filter using high permittivity ceramic substrates was proposed in [31]. While this approach promises a compact design and temperature stability, fabrication complexity and unsuitability to high-frequency applications are major disadvantages. Moreover, slow-wave SIW structures were used to design BPFs with size reduction in longitudinal direction by at least 40% [32–34]. Nevertheless, the increasing fabrication complexity and cost are the main drawbacks.

The HMSIW concept combined with Koch fractal shape EBG structures and coplanar waveguide resonators were recently introduced to miniaturize the overall filter area [35, 36]. In addition, quarter- and eighth-mode SIW cavities were used to design BPFs in [37, 38]. Nevertheless, such multilayer designs came at the cost of complex and expensive fabrication process.

1.3.2 Progress in SIW Power Dividers

The PDs/PCs are widely used in a variety of microwave and mm-wave front-end subsystems where a signal needs to be divided or combined. They find applications in PAs, mixers, and antenna feeding systems. Thus, more efforts have been devoted lately towards developing PDs with excellent electrical performance (e.g., low pass-band losses and excellent matching) without compromising the physical features or increasing the fabrication complexity. SIW-based PDs/PCs attracted special attention for mm-wave application as they offer better power handling and lower losses. In [39], a broadband HMSIW WPD was proposed for mm-wave applications. Ring-shaped

SIW WPDs/WPCs implemented on two-layer substrate with several distributed resistors were proposed in [40]. However, the used double layer topology increased the fabrication complexity and cost. Moulay and Djerafi proposed a new ring-shaped configuration, which shows high isolation over a FBW of 18% [41]. Another high isolation wideband PD was proposed in [42]. The structure was implemented with a slot on the upper conductor of the SIW to emulate the matched E-plane arm of the magic-T.

Moreover, combining the bandpass filter and power divider functions on a single component is attracting special attention in order to maintain a compact overall circuit size. Hui *et al.* designed and fabricated a multilayer filtering PD with inductive posts in [43]. Nevertheless, the isolation is not reported and the resulting circuit area is large. Resonators and cavities were used to realize Filtering PDs [44–48]. Nevertheless, the resulting physical area and high insertion losses are major drawbacks. In addition, wideband power dividers/combiners based on resistive layers and absorbing material were proposed in [49, 50], respectively. Nevertheless, such wideband response comes at the cost of weak matching levels and added circuitry size. Moreover, multi-way PDs based on eighth-mode SIW was proposed in [51, 52].

In addition, Gysel power divider, invented by U. Gysel, is a good candidate for high-power application [53]. Similar to WPD, the Gysel PD can achieve high isolation between the output ports and matched condition at all ports. In [54], a broadband Gysel PD implemented with microstrip-to-slotline transitions was proposed. A hybrid structure of HMSIW and microstrip isolation networks was developed in [55]. However, the use of microstrip limit its use for mm-wave applications. Chen *et al.* implemented the Gysel PD completely using SIW lines [56]. Two different typologies were designed and fabricated using multilayer LTCC technology. Nevertheless, high insertion loss and fabrication complexity are the main drawbacks.

1.3.3 Progress in Wideband Microstrip WPDs

As mentioned earlier, WPD finds many applications due to its ease of design and convenient electrical performance which is characterized by a high isolation between its output ports and a perfect matching at all ports. Nevertheless, such a performance is realized only at a small fraction of bandwidth due to the fact that conventional microstrip WPDs support only a single frequency, which limits their utilization to wideband systems. Consequently, broadening the operating bandwidth while maintaining the same desired electrical features are of utmost importance to several emerging applications.

In [57–60], multi-stage wideband WPDs were proposed. However, the added physical dimension is a major drawback. A compact ultra-wideband (UWB) divider was proposed in [61] by replacing the quarter-wave transformers in a two-stage WPD with bridged T-coils. However, the complexity in the design and fabrication process limits its utilization in low profile applications. A novel configuration of a 3-way power divider was proposed in [62] by incorporating two isolation resistors and microstrip coupled lines. Although the resulting structure is planar, the desired response were obtained across a narrow bandwidth. A 3-way unequal split UWB divider employing tapered line transformers instead of the conventional uniform lines was proposed in [63] at the expense of the added circuitry area. In [64–66], multi-way power dividers were proposed by cascading several 2-way WPDs. A 3-way UWB power divider based on broadside coupling via multilayer microstrip/slot transitions was proposed in [67]. A multi-way WPD was realized using offset double-sided parallel-strip lines in [68]. While excellent electrical properties were achieved in such designs, the added fabrication complexity and cost may limit their applications to microwave integrated circuits.

1.3.4 Progress in Front-ends on Flexible Substrates

Flexible substrates are of significant importance for wearable technologies, portable monitoring devices, and flexible organic light-emitting diode display technology. LCP substrate is a widely used flexible substrate that is being explored for high-frequency applications. It has several attractive features characterized by stable dielectric constant, low loss tangent over a wide frequency range, inherent near-hermetic property, and low processing temperature [11]. LCP can be implemented on different transmission line technologies such as the popular microstrip lines [69, 70], CPWs [71, 72], and SIW [73, 74]. Numerous front-ends based on LCP have been reported including antennas [75–77], filters [78, 79], switches [80, 81], and oscillators [82, 83].

1.4 Organization

Chapter 2 presents the theoretical platform of Fourier-varying via-hole walling transmission lines in which the width between the metallic walls is varying according to a truncated Fourier series. Then, these E-wall-varied transmission lines are utilized to design SIW- and HMSIW-based BPFs with and without SIW-to-microstrip transitions. Such BPFs are optimized using genetic algorithm (GA) to obtain the the required frequency response with no added fabrication complexity or cost. The theoretical results of the proposed BPFs are further validated through means of full-wave EM simulations, fabrications, and measurements.

Chapter 3 presents the utilization of the Fourier-varying via-hole transmission lines in the design and realization of highly selective WPD. Mathematical derivations of a compact and planar divider is carried out through the even-/odd-mode analysis. Moreover, the half-mode concept is employed to cut down the size of the PD by 50%. Validations are given through simulated and measured results, in which both are elaborated and compared to verify the design concept.

Chapter 4 presents a general mathematical guidelines to design in-phase equal-split N -way WPD with bandwidth redefinition characteristics. Quarter-wave matching uniform transmission lines in the conventional design are replaced with NTLs governed by a truncated Fourier series. The analysis starts by reducing the multi-way divider to its 2-way equivalent model. Then, even-mode analysis is adopted to obtain NTLs with predefined bandwidth functionalities; whereas several isolation resistors are optimized in the odd-mode analysis to achieve proper isolation and output ports matching over the frequency range of interest. The theoretical results of the proposed design approach are further validated through means of full-wave EM simulations, fabrications, and measurements of 3- and 4-way divider prototypes.

Chapter 5 presents a novel systematic approach to design compact CPW transformers to match predefined source and load impedances for single-, multi-, and wide-band applications. The signal trace and the adjacent ground planes in the conventional CPW structure are width-modulated along the propagation path of the electromagnetic wave while maintaining a constant ground-trace separation. Validation is carried out by designing and simulating single-, multi-, and wide-band transformers. The proposed transformers are optimized for the implementation on flexible liquid crystal polymer (LCP) substrates.

Chapter 6 concludes this dissertation and suggests future research paths that are aligned with the scope of this investigation. It also summarizes the scientific contribution of this study and lists the resulting publications.

Chapter 2

E-wall Varied SIW Bandpass

Filters

Modern microwave and millimeter wave systems require low cost, compact size, high performance, and mass-producible front-ends. In spite of high Q-factor and low losses of the rectangular waveguide, its bulky size and tiresome and expensive fabrication and assembly limit its application in modern wireless systems. Thus, SICs are promising candidates to fulfill the aforementioned requirements as they facilitate interconnects and integrations between planar and non-planar circuits and can be fabricated using the standard fabrication techniques such as PCB and LTCC. SICs make it possible to synthesize a non-planar waveguide in a planar form on a single substrate [5]. Using this concept, the bulky rectangular waveguide is effectively transformed into a planar structure with two parallel metallic rows of via-holes, known as SIW as shown in Figure 2-1. This hybrid integration of planar and rectangular waveguide structures in SIW forms enables the design of high performance front-ends with attractive features such as low cost, compact size, high Q-factor, and high-volume production.

This chapter presents a new representation of conventional SIW transmission lines by varying the locations of the metallic via-holes. These variations are governed by

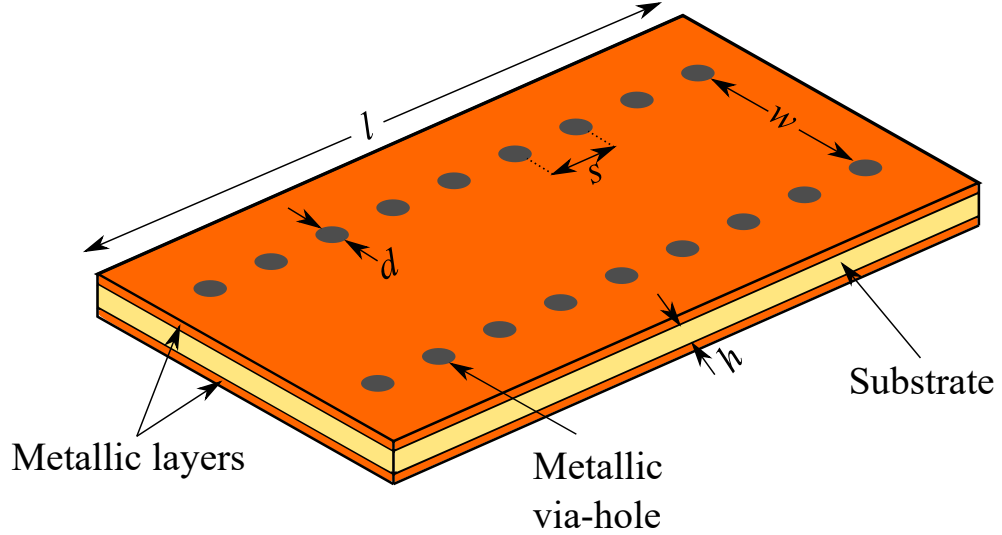


Figure 2-1: A schematic diagram of a conventional SIW structure.

truncated Fourier series expansion and lead to advanced electrical features compared to the uniform SIW structure. At the same time, structural complexity and fabrication cost are kept unaltered.

This chapter is summarized as follows: Section 2.1 presents the basic principles of operation of a SIW. Section 2.2 discusses the proposed theory and the detailed design procedure of E-wall varied SIW transmission lines. Then, Section 2.3 elaborates the design procedure to design BPFs without the use of matching networks (e.g. tapered SIW-to-microstrip transitions), whereas results for BPFs with different operating bandwidths are given in Section 2.4 to validate the underlined concept. Section 2.5 discusses the design of HMSIW-based with SIW-to-microstrip transitions. Finally, conclusions are drawn in Section 2.6.

2.1 Operation Principles

It was found that an SIW structure has the same propagation and dispersion characteristics of a rectangular waveguide filled with the same substrate material provided that an effective width, w_{eff} , is used instead of its actual width, w [84]. Consequently,

various empirical formulas have been proposed to find the optimum w_{eff} that gives the best agreement between rectangular waveguide and its SIW counterpart [85,86]. The first proposed formula found is [84]:

$$w_{\text{eff}} = w - \frac{d^2}{0.95s} \quad (2.1)$$

where w is the width of the SIW transmission line, d is the diameter of the conductive via-holes, and s is the horizontal spacing between any two adjacent via-holes as illustrated in Figure 2-1. This formula is accurate only when s is sufficiently small. In addition, when d increases, a small error will appear, which lead to the proposal for a more accurate empirical formula given by [87]:

$$w_{\text{eff}} = w - 1.08\frac{d^2}{s} + 0.1\frac{d^2}{w} \quad (2.2)$$

It is paramount to mention that 2.2 is very accurate when

$$s/d < 2 \quad (2.3a)$$

$$d/w < 0.2 \quad (2.3b)$$

These conditions ensure avoiding leakage losses between the metallic via-holes. Another simple, yet accurate, expression was proposed in [88] and it is given by:

$$w_{\text{eff}} = \frac{w}{\sqrt{1 + \left(\frac{2w-d}{s}\right) \left(\frac{d}{w-d}\right)^2 - \frac{4w}{5s^4} \left(\frac{d}{w-d}\right)^3}} \quad (2.4)$$

A more recent formula found using a mode-matching approach is given by [89]:

$$w_{\text{eff}} = w - s \left(0.766e^{0.4482\frac{d}{s}} - 1.176e^{-1.214\frac{d}{s}} \right) \quad (2.5)$$

The design of the SIW structure starts by specifying the cut-off frequency, f_c , of the dominant mode, substrate relative permittivity, ϵ_r , s/d , and d/w . Then, w_{eff} can be calculated based on f_c of its rectangular waveguide counterpart given by:

$$w_{eff} = \frac{c}{2f_c\sqrt{\epsilon_r}} \quad (2.6)$$

where c is the speed of light. Finally, the SIW actual width, w , can be calculated based on one of the aforementioned eqs. (2.1), (2.2), (2.4) and (2.5). It can be noted from these equations that the ratios of s/d and d/w are controlling the width equivalency not their absolute values.

The minimization of losses is a vital consideration when designing SIW components. In addition to the conductor and dielectric losses which affect the rectangular waveguide, and thus the SIW, the later has an additional source of losses, namely the radiation loss [90]. This radiation leakage between the metallic via-holes could be neglected if the ratios s/d and d/w are sufficiently small [87]. However, practical considerations for limited machining techniques need to be considered. In SIW structures, similar to rectangular waveguides, conductor and dielectric losses are very high near the cutoff frequency and then decrease and stabilize [91]. Thus, the favorable practical range of operation for the SIW is the same as rectangular waveguide (i.e., $1.25f_c$ to $1.89f_c$). Increasing the substrate thickness, h , reduces conductor losses, but it has no effect on dielectric losses. The latter depends on the loss tangent of the dielectric substrate and the operating frequency, not the SIW geometry [92]. Formulas for the different type of losses are provided in Appendix A.

Because the EM is not completely confined within the SIW, a crosstalk between adjacent SIW transmission lines could occur. In [93], a formula for calculating the

crosstalk based on the SIW geometrical dimensions was derived and it is given by:

$$C = N^2 \left[\frac{\frac{1}{w} \left(\frac{d}{w}\right)^{2.84} \left(\frac{s}{d} - 1\right)^{6.28}}{572 \sqrt{\left(\frac{2w}{\lambda}\right)^2 - 1}} \right]^{1.2732} \quad (2.7)$$

where λ is the wavelength of the SIW line and N is the total number of apertures.

2.1.1 Frequency Region of Interest

As mentioned earlier, the performance of the SIW structure is highly dependent on the geometrical parameters of the structure. In order to ensure that the SIW is operating in the region that has negligible leakage losses and does not present any bandgap effect, the following design rules should be satisfied [90]:

$$s > d \quad (2.8a)$$

$$\alpha_l/k_0 > 1 \times 10^{-4} \quad (2.8b)$$

$$s/\lambda_c < 0.25 \quad (2.8c)$$

$$s/\lambda_c > 0.05 \quad (2.8d)$$

Condition (2.8a) is to make the circuit physically realizable by making the space between the via-holes larger than their diameter, whereas condition (2.8b) ensures negligible leakage losses. A more restrictive condition is $s/d < 2$. The last two constraints limits the practical values of s by an upper limit of $\lambda_c/4$ to avoid any bandgap in the operating bandwidth and a lower limit of $\lambda_c/20$ to minimize the number of the metallic via-holes. The frequency region of interest of the SIW is depicted in Figure 2-2.

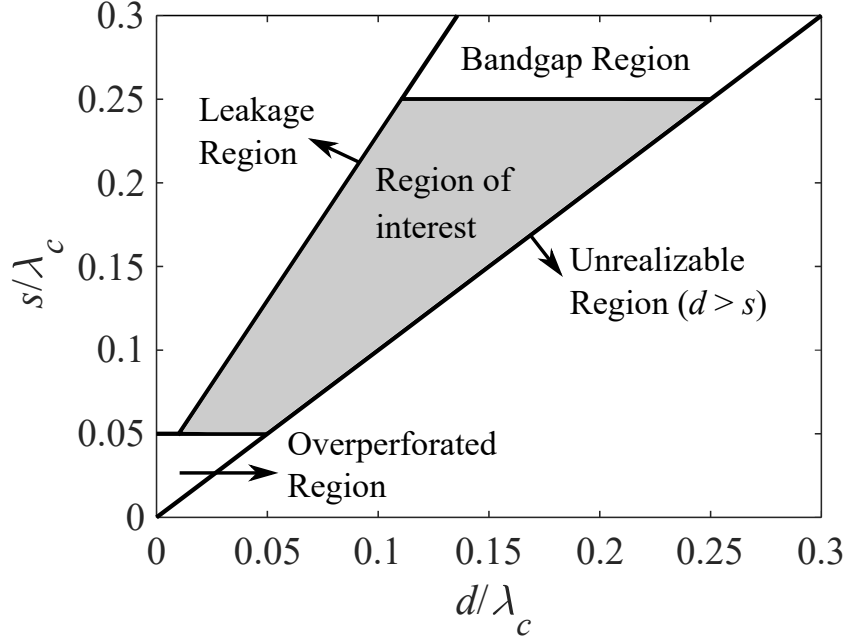


Figure 2-2: Frequency Region of interest for the SIW in the plane of d/λ_c and s/λ_c [69].

2.2 E-wall varied SIW transmission lines Design

Schematic diagrams of the proposed E-wall varied structures are shown in Figures 2-3 and 2-4. In this work, the width between the metallic walls (i.e., via-hole locations) is varied to obtain predefined electrical properties under physical constraints including ports matching and machining limitations. As mentioned earlier, by using w_{eff} , existing design models and analysis equations associated with rectangular waveguide theory can be utilized in a straightforward manner for the development of SIW components. Here, the expression given in (2.2) is used due to its accuracy in modeling the various SIW parameters.

Two types of end-terminations are studied; specifically, with and without SIW-to-microstrip transitions. In this section, the general design guidelines to design SIW transmission lines are discussed. Then, the design methodology of SIW-based BPFs without SIW-to-microstrip transitions (i.e., Figure 2-3) is considered in Section

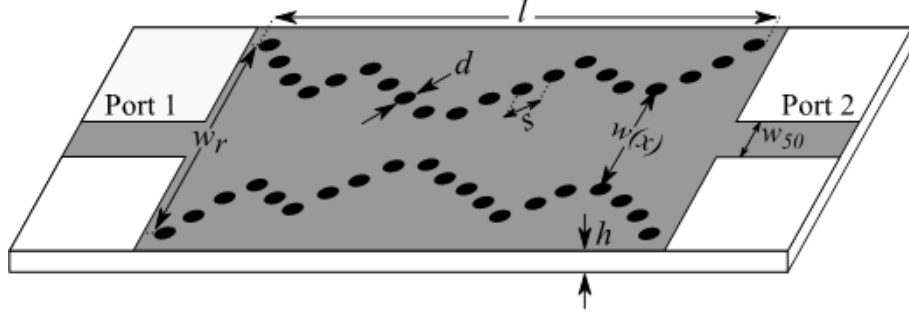


Figure 2-3: A schematic diagram of the proposed SIW-based structure with varying via-hole walling without SIW-to-microstrip transitions. White, grey and black colors represent the substrate, metal and via-holes, respectively.

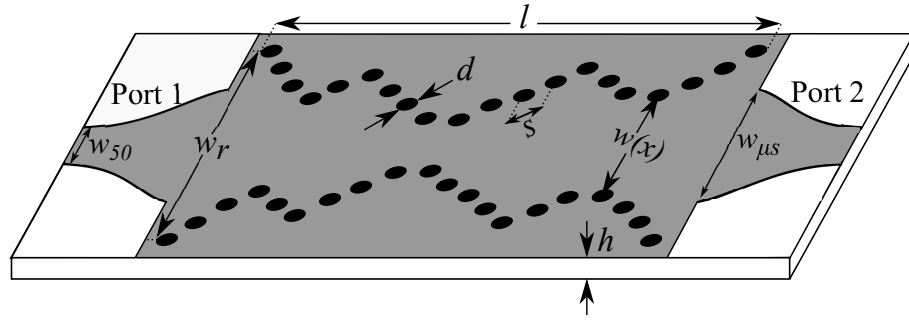


Figure 2-4: A schematic diagram of the proposed SIW-based structure with varying via-hole walling with SIW-to-microstrip transitions. White, grey and black colors represent the substrate, metal and via-holes, respectively.

2.3.1; whereas the design guideline of SIW-based BPFs taking into account SIW-to-microstrip transitions (i.e., Figure 2-4) is given in Section 2.3.2. The response of a conventional SIW structure with these two types of end-terminations are plotted in Figure 2-5. In contrast to the case where no matching networks are used, an SIW with a tapered SIW-to-microstrip transitions results in a highpass response as its equivalent rectangular waveguide.

The effective width, $w_{eff}(x)$, is divided into M uniform SIW segments, each of a length $\Delta x = l/M$, where l is a predefined length chosen to achieve a compact layout. M is chosen such that $\Delta x \ll \lambda_g$, where λ_g is the guided wavelength at the

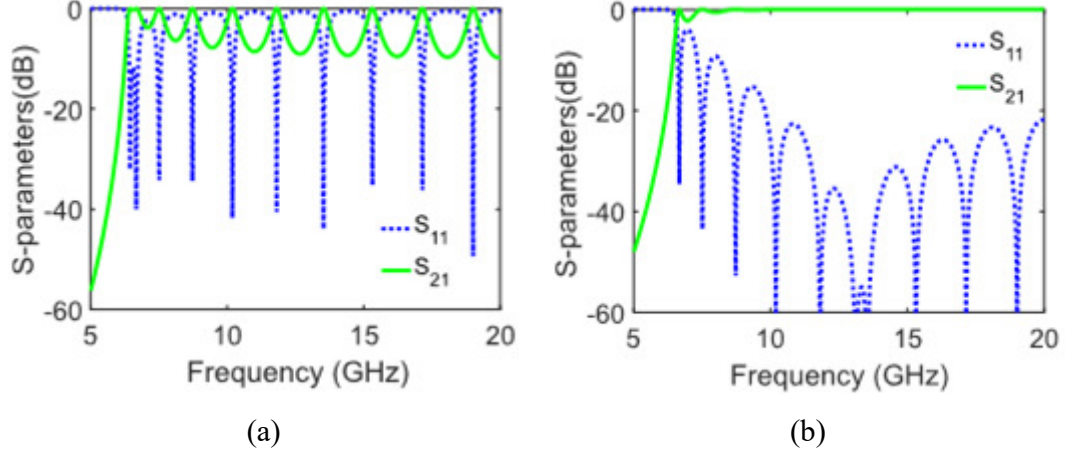


Figure 2-5: S -parameters of a conventional SIW structure: (a) without SIW-to-microstrip transition, and (b) with a Klopfenstein tapered SIW-to-microstrip transition.

center frequency of the design bandwidth. Figure 2-6 shows the variations of w_{eff} and f_c , calculated at the center of each segment, $\Delta x_m = [m - 0.5]\Delta x$, where $m = \{1, 2, \dots, M\}$, vs. the physical length of the SIW structure. It can be noted that some segments will have a cut-off frequency below the passband (i.e., propagation mode); whereas others will have a cut-off frequency higher than the passband (i.e., evanescent mode). These variations in f_c will lead to the desired passband/stopband response. For simplicity, Figure 2-6 is plotted with M and l equal to 20 and 20 mm, respectively. Thus, $\Delta x = 1$ mm.

Then, $w_{eff}(x)$ is modeled in a truncated Fourier series that has the following form [94]:

$$w_{eff}(x) = w_r \exp \left[\sum_{n=0}^N a_n \cos \frac{2\pi nx}{l} \right] \quad (2.9)$$

where N is the number of the series coefficients and w_r is a reference effective width obtained based on f_c as given in [87]. The resulting $w_{eff}(x)$ should adhere to reason-

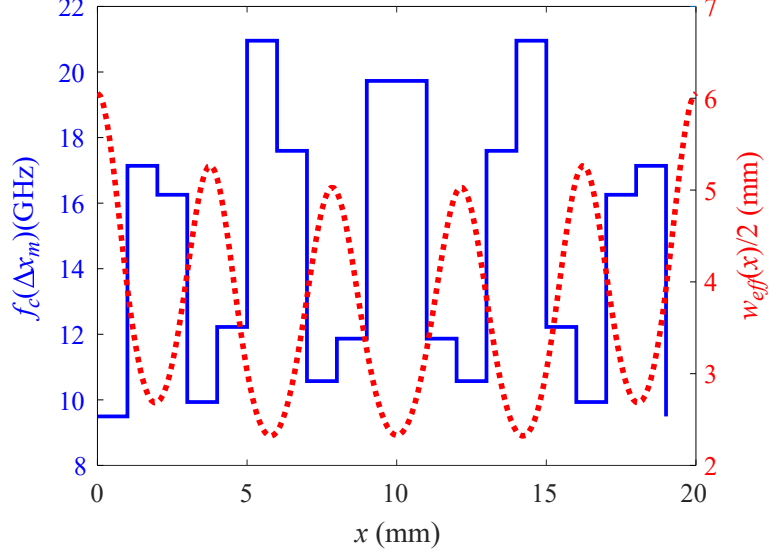


Figure 2-6: Cutoff frequency and width variations at the center of each SIW segment vs. physical length. Solid blue and dotted red represent f_c and $w_{eff(x)}/2$, respectively.

able fabrication limits and meet the following matching conditions:

$$w_{min} \leq w_{eff}(x) \leq w_r \quad (2.10a)$$

$$w_{eff}(0) = w_{eff}(l) = w_r \quad (2.10b)$$

The constraint in (2.10a) limits the variation of $w_{eff}(x)$ within a maximum value $w_{max} = w_r$ and a minimum value $w_{min} > 5d$ to satisfy the condition given in (2.3b); whereas the constraint (2.10b) enforces equal widths at both ends of the SIW structure, and is realized by satisfying the following condition:

$$\sum_{n=0}^N a_n = 0 \quad (2.11)$$

In order to apply transmission line theory to the waveguide, the phase constant, β , and the characteristic impedance, Z_0 , should be calculated for each segment. For

the dominant mode in a rectangular waveguide, β can be calculated as [95]:

$$\beta(\Delta x_m) = \sqrt{\omega^2 \mu \epsilon - \left(\frac{\pi}{w_{eff}(\Delta x_m)} \right)^2} \quad (2.12)$$

where $\Delta x_m = [m - 0.5]\Delta x$ represents the center of the m^{th} segment, ω is the radian frequency, ϵ is the permittivity, and μ is the permeability. While there is no unique definition for the characteristic impedance of a waveguide, the available definitions differ by a constant, k , term [96, 97]. When a waveguide is matched to a uniquely defined impedance (e.g., coaxial cable, microstrip feedline), the value of the constant becomes significant. Initially, the power-current definition is used, which is given as follows [96]:

$$Z_{0,pi}(\Delta x_m) = k \frac{h}{w_{df}(\Delta x_m)} \sqrt{\frac{\mu_r}{\epsilon_r}} \frac{\lambda_g(\Delta x_m)}{\lambda} \quad (2.13)$$

where h is the substrate thickness, $k = 465$ for the power-current definition, and λ_g/λ can be expressed as:

$$\frac{\lambda_g(\Delta x_m)}{\lambda} = \frac{1}{\sqrt{1 - (f_c(\Delta x_m)/f)^2}} \quad (2.14)$$

It is found that there is a discrepancy between the simulated power-current characteristic impedance and $Z_{0,pi}$ obtained from (2.13). Such differences become more significant around the cutoff frequency. In addition, the change in some design parameters (e.g., w_{eff} , ϵ_r , h) necessitates a different constant to guarantee the best agreement between the analytical and simulated/measured responses. Hence, the constant value is changed to match the simulation results. By substituting λ_g and λ in (2.13) with $2\pi/\beta(\Delta x_m)$ and $1/\sqrt{\mu\epsilon}$, respectively, it can be written as:

$$Z_{0,pi}(\Delta x_m) = k \frac{h}{w_{df}(\Delta x_m)} \sqrt{\frac{\mu_r}{\epsilon_r}} \frac{2\pi}{\beta(\Delta x_m)} f \sqrt{\mu\epsilon} \quad (2.15)$$

which can be expressed in the following form

$$Z_{0,pi}(\Delta x_m) = k \frac{h}{w_{df}(\Delta x_m)} \frac{\omega \mu_r \sqrt{\mu_0 \epsilon_0}}{\beta(\Delta x_m)} \quad (2.16)$$

where $\omega = 2\pi f$. Then, the right-hand side is multiplied by the factor $\sqrt{\epsilon_0/\mu_0} \times \sqrt{\mu_0/\epsilon_0}$, leading to:

$$Z_{0,pi}(\Delta x_m) = \left(k \sqrt{\frac{\epsilon_0}{\mu_0}} \right) \frac{h}{w_{df}(\Delta x_m)} \frac{\omega \mu_r \sqrt{\mu_0 \epsilon_0}}{\beta(\Delta x_m)} \sqrt{\frac{\mu_0}{\epsilon_0}} \quad (2.17)$$

Since $k \sqrt{\epsilon_0/\mu_0}$ is constant, it is denoted as k' . Then, (2.17) is written in the following form, considering that $\mu = \mu_0 \mu_r$:

$$Z_0(\Delta x_m) = k' \frac{h}{w_{df}(\Delta x_m)} \frac{\omega \mu}{\beta(\Delta x_m)} \quad (2.18)$$

Finally, provided that $Z_{wave}(\Delta x_m) = \omega \mu / \beta(\Delta x_m)$, the expression in (2.18) can be written as:

$$Z_0(\Delta x_m) = k' \frac{h}{w_{eff}(\Delta x_m)} Z_{wave}(\Delta x_m) \quad (2.19)$$

where $k' = 1.2343$ matches the power-current definition given in (2.13) (i.e., $k = 465$). Then, simulated Z_0 and Z_{wave} are used to find the value of k' that matches the simulated response.

The waveguide characteristic impedance expressions in (2.13) and (2.19) are plotted in Figure 2-7 together with the simulated impedance from ANSYS Electronics Desktop [98] for different w_{eff} and h values and for $\epsilon_r = 3.55$. Figure 2-7 shows that the accuracy of (2.19) outperforms that of (2.13), which validates the use of the former in the proposed procedure. Once Z_0 is evaluated for all M segments, the $ABCD$

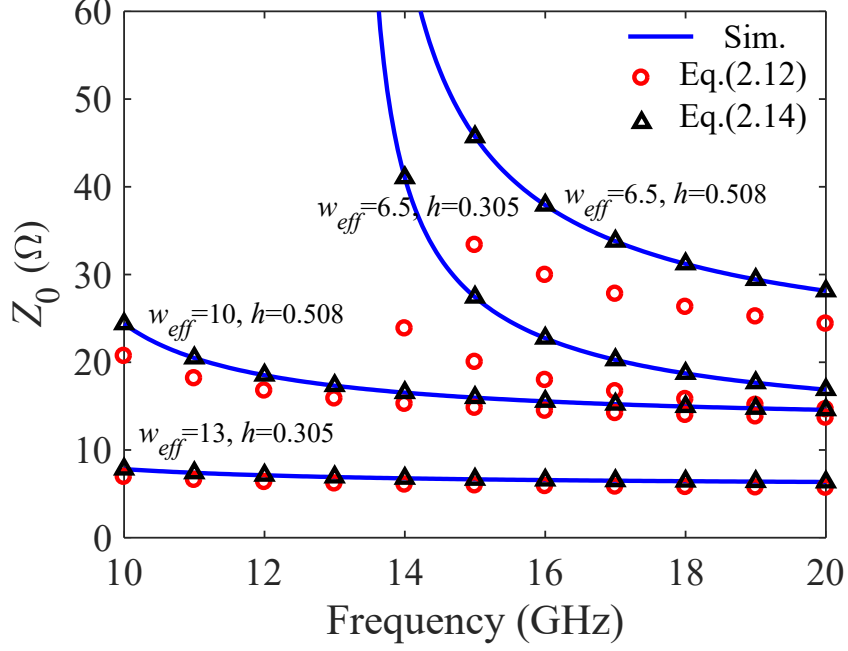


Figure 2-7: Simulated versus analytical Z_0 based on expressions (2.13) and (2.19) plotted for different w_{eff} and h (units in mm).

parameters of the m^{th} segment are obtained as follows:

$$A_m = D_m = \cos [\Delta x \cdot \beta (\Delta x_m)] \quad (2.20a)$$

$$B_m = Z_0^2 (\Delta x_m) C_m = j Z_0 (\Delta x_m) \sin [\Delta x \cdot \beta (\Delta x_m)] \quad (2.20b)$$

Then, the $ABCD$ matrix of the SIW structure is found by multiplying the $ABCD$ matrices of all M segments as follows:

$$[A \ B; C \ D] = \prod_{m=1}^M [A \ B; C \ D]_m \quad (2.21)$$

The resulting overall $ABCD$ matrix is used to express the input port matching, S_{11} , and the transmission parameter, S_{21} , of the SIW-based structure, which are given

as [95]:

$$S_{11} = \frac{AZ_l + B - CZ_s Z_l - DZ_s}{AZ_l + B + CZ_s Z_l + DZ_s} \quad (2.22a)$$

$$S_{21} = \frac{2(AD - BC)\sqrt{Z_s Z_l}}{AZ_l + B + CZ_s Z_l + DZ_s} \quad (2.22b)$$

where Z_s and Z_l are the source and load impedances connected to the SIW structure (e.g. microstrip feedlines or SIW-to-microstrip transitions). Once the S -parameters are expressed in terms of the $ABCD$ matrix of the SIW structure, an error function can be used to achieve a desired performance as will be discussed in the next section.

2.3 SIW Bandpass Filtering with Fourier-varying Via-hole Walling

In this section, several BPFs with and without SIW-to-microstrip transitions are designed, simulated, and measured as shown in Figures 2-3 and 2-4. The design of BPFs with these two-end terminations is discussed in details in the following two subsections.

2.3.1 Filter Design without Matching Networks

According to Figure 2-3, no matching network is incorporated in the SIW structure in order to reduce the overall filter dimensions. The design procedure for such filters is continued from (2.22) by setting $Z_{s,l} = 50\Omega$. Then, the following error function is

established for a bandpass filtering response:

$$E = \begin{cases} \sqrt{(|S_{11}| - 1)^2 + \alpha |S_{21}|^2}, & f_{\min} \leq f \leq f_{cL} \\ & f_{cH} \leq f \leq f_{\max} \\ \sqrt{\alpha |S_{11}|^2 + (S_{21} - 1)^2}, & f_{cL} \leq f \leq f_{cH} \end{cases} \quad (2.23)$$

where f_{cL} and f_{cH} are the lower and higher cutoff frequencies of the passband, respectively, and α is a weighting factor used to minimize the reflection coefficient in the passband and increase the lower/upper stopband rejection levels. Here, f_{\min} and f_{\max} are minimum and maximum frequencies of the optimization process, respectively. The error vector resulting from applying (2.23) to all frequency points within $[f_{\min}, f_{\max}]$ is used to establish the following objective function:

$$\text{Objective} = \sqrt{\frac{1}{M_f} \sum_{i=0}^{M_f} E(f_{\min} + i\Delta f)} \quad (2.24)$$

where M_f is the number of frequency points given by

$$M_f = \frac{f_{\max} - f_{\min}}{\Delta f} + 1 \quad (2.25)$$

where Δf is a frequency increment. Ideally, Δf should be as close as possible to zero, but this will increase the optimization time considerably. In this context, Δf is chosen to be 0.05 GHz.

The Fourier coefficients, a_n , that result in an optimum bandpass filtering response are found by minimizing (2.24). A genetic algorithm (GA) is used for its applications in microwave and mm-wave front-ends design and optimization [99–102]. Table 2.1 illustrates the adopted optimization settings. It is noteworthy to mention that there is no unique solution for the coefficients (i.e., different a_n 's in each run). The coefficients with the optimal response, in combination with a width profile $w_{eff}(x)$ that

Table 2.1: List of Optimization Parameters

Parameter	Value
No. of GA generations	700
GA population size	200
GA crossover rate	0.7
GA mutation rate	0.1
Lower/Upper bounds of the coefficients	-1/1
Function Tolerance	1×10^{-20}

Table 2.2: List of Physical Dimensions of the SIW BPFs

Parameter	Value (mm)	Parameter	Value (mm)
d	0.50	w_{min}	2.50
s	0.90	l	40.0
$w(x = 0, l)$	13.0	w_{50}	0.68
$w_r = w_{max}$	12.7		

satisfies (2.10) is considered in the following design steps. In the proposed design, the separation between the centers of the via-holes, s , is calculated based on the Euclidean distance, not the horizontal distance.

Three examples are optimized based on the outlined analysis considering a 0.3048-mm-thick Rogers RO4003C substrate with $\epsilon_r = 3.55$. The physical dimensions of these filters are listed in Table 2.2. The three designs have a center frequency of 14 GHz and FBWs of 2.5%, 5.8%, and 18.2%. The number of the series coefficients, N , and the uniform segments, M , are set to 7 and 80, respectively. Finally, k' is set to 1.265; whereas α is chosen to be 30.

Figure 2-8 illustrates the analytical results of the three designs, which all show input port matching better than -20 dB and passband transmission better than -0.2 dB. Figure 2-9 shows the width profiles of the three design examples, which are constrained by the predefined w_{min} and w_{max} . In addition, the end terminations

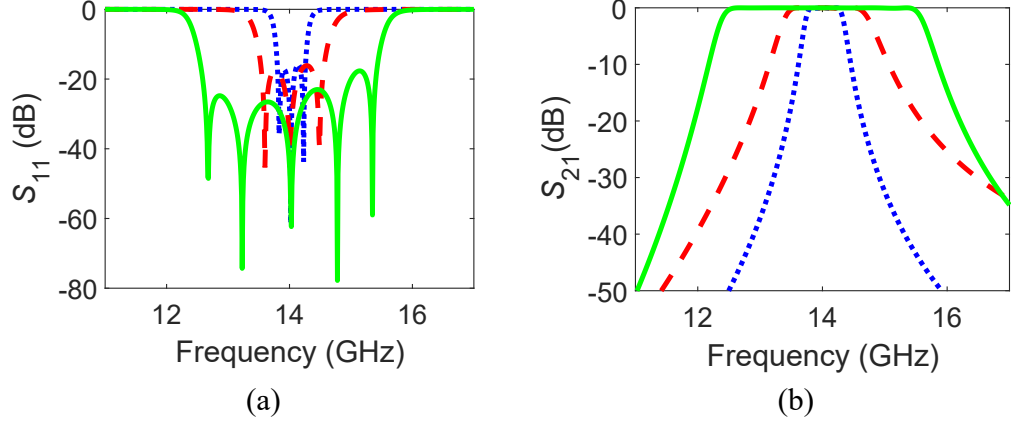


Figure 2-8: Analytical results of three SIW-based BPFs with different passbands. Blue dotted, red dashed, and green solid lines represent passbands of 13.8–14.2 GHz, 13.5–14.5 GHz, and 12.5–15.5 GHz, respectively.

of the three profiles equal w_r . Hence, the results of the three designs validate the proposed methodology.

2.3.2 Filter Design with Klopfenstein Matching Network

Here, Klopfenstein tapered lines [103] are utilized to match the characteristic impedance of the SIW filter to the 50- Ω microstrip feedlines as shown in Figure 2-4. The characteristic impedances at end-terminations, $Z_0(x = 0, l)$, are found using (2.19). Then, (2.22) is calculated, where $Z_{s,l} = Z_0(x = 0, l)$. The Klopfenstein taper is expressed as [104, 105]:

$$\ln \left(\frac{Z(x)}{Z_s} \right) = 0.5 \ln \left(\frac{Z_l}{Z_s} \right) \left[1 + G \left(B, 2 \left(\frac{x}{d_t} - 0.5 \right) \right) \right] \quad (2.26)$$

where Z_s and Z_l represent the source and load impedances at the two ends of the tapered line (i.e., $Z_s = 50\text{-}\Omega$, $Z_l = Z_{\mu s}$), respectively, and d_t is the taper length, and

$$G(B, \xi) = \frac{B}{\sinh B} \int_0^\xi I_0 \left(B \sqrt{1 - \xi'^2} \right) d\xi' \quad (2.27)$$

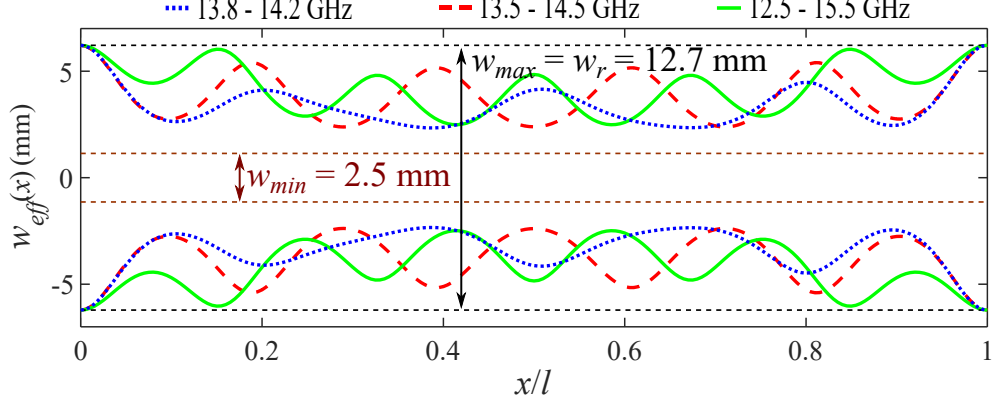


Figure 2-9: Width-varying profiles of the BPFs as a function of the normalized length.

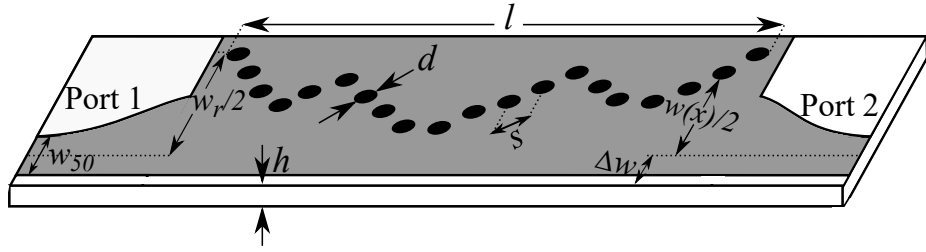


Figure 2-10: Width-varying profiles of the BPFs as a function of the normalized length.

where B is a predefined design parameter that determines the tapered profile and $I_0(x)$ represents the modified zero-order Bessel function. Higher B values improve the input matching at the expense of a longer taper. For a given taper line, the maximum input return loss (in dB) is given as [104, 105]:

$$|RL_{\text{input}}|_{\text{max}} = -20 \log \left[\tanh \left(\frac{B}{\sinh B} \right) (0.21723) \ln \left(\sqrt{\frac{Z_l}{Z_s}} \right) \right] \quad (2.28)$$

Moreover, a HMSIW filter configuration is also proposed with tapered lines to facilitate the necessary impedance matching as shown in Figure 2-10. HMSIW is adopted to reduce the filter dimensions [106]. For an optimum HMSIW operation, the substrate width should be increased slightly to mitigate the fringing effects. The

necessary width increase is found empirically as follows [107]:

$$\begin{aligned} \Delta w = h \times & \left(0.05 + \frac{0.3}{\varepsilon_r} \right) \\ & \times \ln \left(7.9 \times 10^{-4} \frac{w_r^2}{h^3} + \frac{0.104w_r - 2.61 \times 10^{-4}}{h^2} + \frac{0.038}{h} + 2.77 \right) \end{aligned} \quad (2.29)$$

Thus, the effective width of the HMSIW structure is given as:

$$w_{eff,HM}(x) = \frac{w_{eff}(x)}{2} + \Delta w \quad (2.30)$$

Since $w_{eff,HM} < w_{eff}$, $Z_{0,HM}$ is higher than Z_0 in the conventional SIW structure. Hence, for better matching, the transition width of the HMSIW filter, $w_{\mu s,HM}$, is approximately $w_{\mu s}/2$ [108].

2.4 Simulations and Measurements

In this section, simulations and measurements for three BPF prototypes are presented. Prototype (1) is optimized for a 5.8% FBW at 14 GHz center frequency following the procedure presented in Section 2.3.1. Prototype (2) is interfaced with Klopfenstein tapered lines as discussed in Section 2.3.2, and is optimized for a 2.5% FBW at 12 GHz center frequency. Finally, Prototype (3) demonstrates the HM-SIW layout of prototype (2). It is noteworthy to mention that the optimization parameters and physical dimensions listed in Tables 2.1 and 2.2 are adopted in the three designed prototypes. ANSYS Electronics Desktop [98] is used for simulations; whereas measurements are performed with Agilent E8362C network analyzer. Short-open-load-thru calibration is performed to the network analyzer ports with Keysight 3.5 mm mechanical calibration kit to shift the reference plane to the output of the coaxial cables.

The simulated and measured S -parameters of prototype (1) are shown in Figure

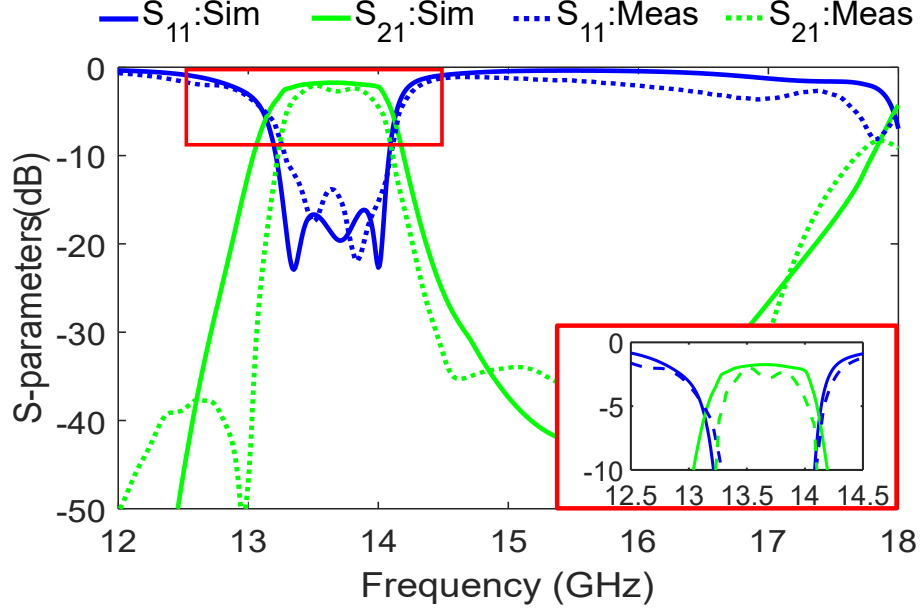


Figure 2-11: Simulations and measurement of the designed SIW-based BPF with a FBW of 5.8% and 14 GHz center frequency.

2-11. The filter has passband port matching and transmission loss better than -15 dB and -2.5 dB, respectively. The maximum upper rejection level is better than -40 dB with a rejection better than -20 dB for 3 GHz after the operating band. The roll-off factor of the filter is 49.9 dB/GHz.

Similarly, the simulated and measured S -parameters of prototype (2) are shown in Figure 2-12. Here, a highly-selective narrowband filter is interfaced with tapered lines. The characteristic impedance in this example is found to be $Z_0 = 7.5\text{-}\Omega$ at the center frequency, which results in $w_{\mu s} = 7.46$ mm. The length of the tapered lines and the value of B are set to 10 mm and 2.5, respectively. Here, passband input port matching and transmission loss better than -19 dB and -3.0 dB, respectively, are obtained. The roll-off factor of this BPFs is 85.8 dB/GHz. This filter address the challenge design of SIW-based BPFs with $\text{FBW} < 5\%$ with a roll-off factor better than the first prototype.

Finally, the simulated and measured S -parameters of prototype (3) are shown in

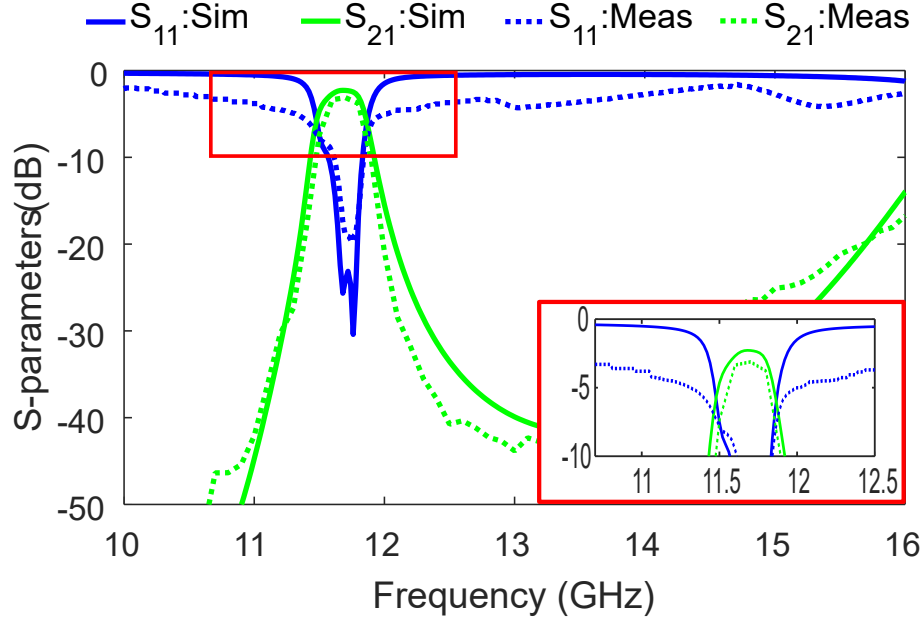


Figure 2-12: Simulations and measurement of the designed SIW-based BPF with a FBW of 2.5% and 12 GHz center frequency.

Figure 2-13 Simulations and measurements are in good agreement. Both the SIW and HMSIW filters have the same order. However, the latter has a slightly broader bandwidth and lower stopband rejection level due to power leakage from the open side aperture in the HMSIW layout, resulting in higher radiation losses near the cutoff frequency [107]. Discrepancies between the simulated and measured results in all prototypes, including the shift in the center frequency, are attributed to the fabrication tolerance, SMA connectors, as well as substrate permittivity and thickness tolerances.

Photographs of the three prototypes are shown in Figure 2-14. Table 2.3 shows the optimized series coefficients and the value of (2.24) for the three prototypes. Table 2.4 represents a comparison between the proposed methodology and other state-of-the-art techniques. The proposed method shows acceptable electrical characteristics as compared to other reported efforts. It is worth mentioning that narrowband filters impose higher insertion losses as observed in prototypes 2 and 3 [27]. In addition, the

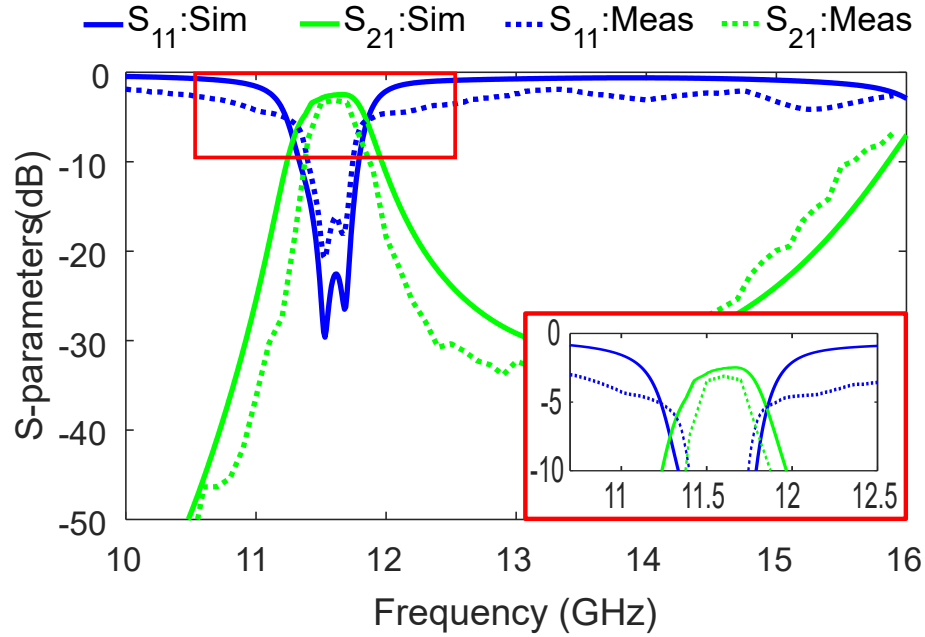


Figure 2-13: Simulations and measurements of the designed HMSIW-based BPF with a FBW of 2.5% and 12 GHz center frequency

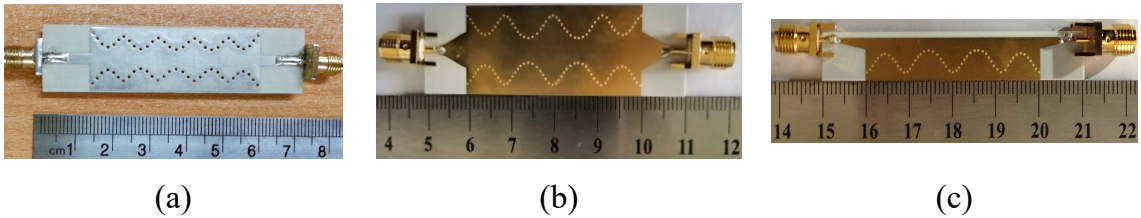


Figure 2-14: Photographs of the three fabricated BPFs: (a) prototype 1, (b) prototype 2, and (c) prototype 3.

demonstrated designs operate at higher center frequencies. This method offers flexibility in FBW redefinition without using extra components (e.g., stubs, resonators, EBG).

The proposed methodology differs from other previous efforts in the following aspects: 1) Unlike [22, 26, 27, 30], all BPF designs presented in this work occupy smaller area and has lower insertion losses due to the absence of higher-order modes of cavities and resonators. 2) In contrast to the multilayer filters elaborated in [23,37], all filter designs presented in this work are planar and implemented on a single layer

Table 2.3: Optimized Fourier Series Coefficients and the Corresponding Objective Function Error Value

	a_0	a_1	a_2	a_3	a_4	a_5	a_6	Value of (2.24)
Prototype (1)	-0.5082	0.0869	0.0417	0.0178	0.0671	0.3733	0.0656	0.6342
Prototype (2&3)	-0.4675	0.0818	0.0311	-0.1765	0.4233	0.0955	0.0125	0.4833

substrate. 3) Although the use of microstrip resonators instead of SIW cavities results in a compact size as presented in [28], this limits the use of such filters for higher-frequency applications as the microstrip losses become very high.

2.5 Conclusion

A systematic methodology is proposed for the design of planar BPFs based on varied SIW and HMSIW via-hole walling governed by a truncated Fourier series expansion. The optimized locations of the via-holes allow predefined bandwidth and acceptable electrical performance. For verification, three prototypes are simulated, fabricated and measured. Simulated and measured results are in a good agreement in both pass- and stop-bands. Differences between simulated and measured results are attributed mainly to the fabrication process and substrate parameters. Klopfenstein tapered lines are used to improve port matching.

The proposed method allows the design of narrowband or wideband BPFs by modifying the optimization parameters. In addition, the proposed method can be utilized in realizing the optimum microstrip-to-SIW transition without performing a parametric study by providing the characteristic end-termination impedances of an SIW structure. Finally, the proposed method can be integrated with other techniques to further enhance the overall electrical performance (i.e., introducing transmission zeros and achieving wide stopband characteristics for wideband BPFs).

Table 2.4: Comparison between the Proposed BPFs and Other State-of-the-art SIW BPFs

Ref.	f_0 (GHz)	FBW (%)	Return Loss (dB)	Insertion Loss (dB)	Stopband BW with rejection >20 (dB)	Area* (λ_g^2)
[22]	10.00	1.2	14.0	3.90	0.30	2.1
[26]	14.87	0.9	14.3	4.20	3.00	4.4
[27]	8.25	1.2	15.0	3.32	2.25	4.0
[28]	5.10	4.2	18.0	2.50	1.00	1.52
[30]	4.85	3.7	17.8	5.00	0.6	2.9
[35]	3.40	25.0	11.4	1.70	2.30	0.45
[37]	3.10	15.5	20.0	1.30	2.70	0.5
Prototype (1)	13.70	5.8	15.0	2.50	3.00	2.94
Prototype (2)	11.70	2.5	19.0	3.00	3.75	1.96
Prototype (3)	11.60	2.5	16.0	3.30	2.95	1.04

* Feedlines are not included in the calculation of the occupied area

Chapter 3

E-wall Varied HMSIW Filtering

Wilkinson Power Divider

This chapter presents a method with clear guidelines to design a compact HMSIW-based WPDs. The design procedure is accomplished by varying the fixed-width of each arm of the conventional WPD. Width variations are governed by a truncated Fourier series with coefficients optimized to achieve predefined frequency matching. The design procedure is divided into two main steps: 1) even-mode analysis, carried out to optimize the series coefficients with predefined bandwidth; 2) odd-mode analysis, utilized to obtain the optimum isolation resistors that guarantee an acceptable isolation and output ports matching over the frequency range of interest. In addition, half-mode configuration is employed for further size reduction. The proposed design procedure leads to miniaturized planar structure without increasing the fabrication complexity.

This chapter is organized as follows: Section 3.1 presents the detailed design procedure of the even-/odd-mode analysis. Simulated results of a designed in-phase equal-split narrowband WPD are given in Section 3.2. Finally, conclusions are given in Section 3.3.

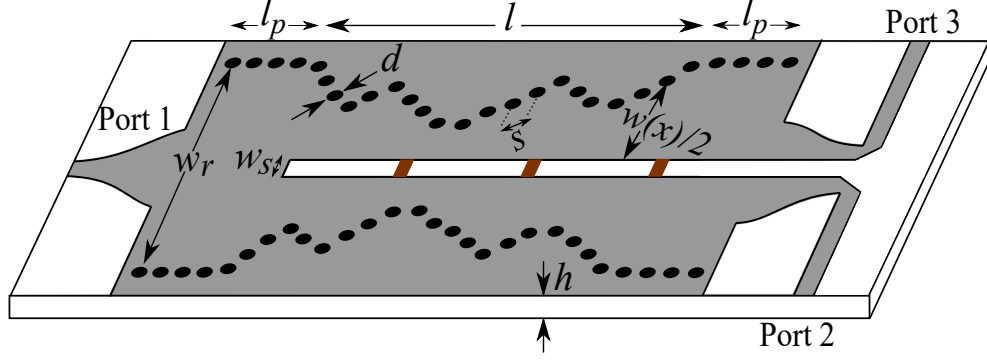


Figure 3-1: A schematic diagram of the proposed HMSIW-based WPD with varying via-hole walling. White, grey, black and brown colors represent the substrate, metal, via-holes, and isolation resistors, respectively.

3.1 WPD Design

A schematic diagram of the proposed HMSIW-based WPD is shown in Figure 3-1. The locations of the metallic via-holes is governed by truncated Fourier series to achieve a predefined performance. These width variations lead to variations in the characteristic impedance, $Z_0(x)$, and propagation constant, $\beta(x)$. Such response is obtained by properly profiling the width of each arm of the proposed SIW divider.

In section 3.1.1, the even-mode analysis is conducted to optimize the Fourier series coefficients to obtain predefined electrical properties under physical constraints including ports matching and machining tolerance; whereas the odd-mode analysis is used to find the optimal values of the isolation resistors to meet proper output ports' matching and isolation levels.

3.1.1 Even-odd Analysis

The even-mode equivalent circuit of the proposed WPD is shown in Figure 3-2. The variable-width transmission line has a length l with a varying characteristic impedance, $Z_0(x)$, and propagation constant, $\beta(x)$, and matches a source impedance,

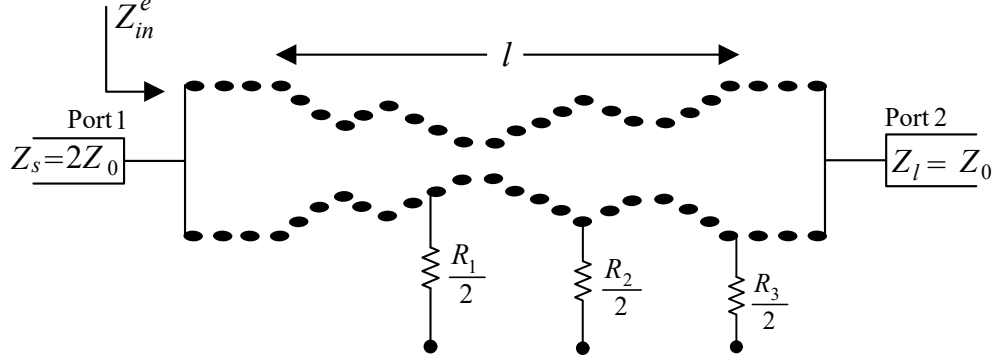


Figure 3-2: The equivalent even-mode circuit of the proposed SIW WPD.

Z_s , to a load impedance Z_l . Due to the symmetric excitation at the two output ports, the isolation resistors $R_j/2$ ($j = 1, 2, 3$) are open-circuited. Thus, they have no effect on finding the optimal Fourier series coefficients. The width profile of the transmission line is governed by the truncated Fourier series given in (2.9). w_{eff} should be restricted by the constraint given in (2.10) stated in Section 2.2. Then, the $ABCD$ matrix is calculated following the design procedure presented in Section 2.2. To design a power divider with filtering response, the S -parameters should be optimized to minimize S_{21} in the passband and maximize it in the stopbands. Hence, the error function in (2.23) and the objective function in (2.24) presented in Section 2.3.1 are used in a similar way. It is worthy to mention that this bound-constrained nonlinear error function in (2.24) is minimized using the GA and the optimization parameters listed in Table 2.1 are applied here also.

As shown in Figure 3-2, $Z_s = 2Z_0$, where Z_0 is calculated as indicated in (2.19). On the other hand, $Z_l = Z_0$. However, since the half-mode structure will be used and it has almost half of the original width, the characteristic impedance of the half-mode structure will be approximately double of the original full structure. Thus, Z_l is set to $2Z_s$ in the optimization. Thus, (2.22) is calculated with $Z_s = Z_l = 2Z_s$.

Table 3.1: Optimized Fourier Series Coefficients and the Corresponding Objective Function Error Value

a_0	a_1	a_2	a_3	a_4	a_5	a_6	Value of (2.24)
-0.5061	0.0645	0.0171	-0.1112	0.4938	0.0467	-0.0049	0.5040

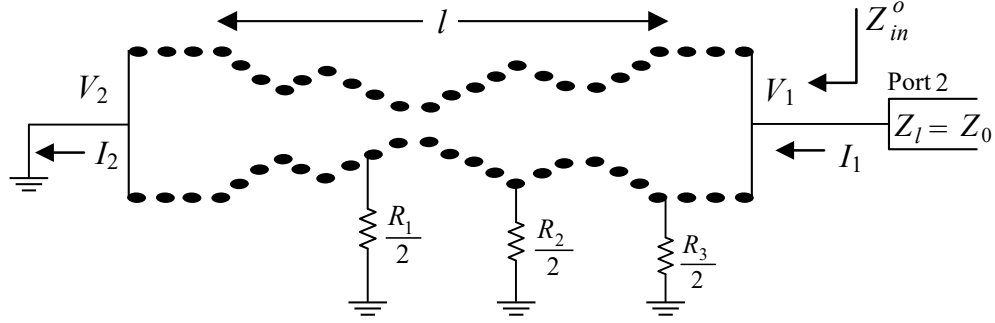


Figure 3-3: The equivalent odd-mode circuit of the proposed SIW WPD.

3.1.2 Odd-odd Analysis

Figure 3-3 shows the equivalent odd-mode circuit of the proposed divider, which is used to obtain the values of the isolation resistors needed to achieve the optimum output ports' isolation and matching conditions. Here, $R_j/2$ resistors are terminated with a short circuit due to the asymmetric excitation of the output ports. Once the optimum Fourier series coefficients in (2.9) are found, three isolation resistors are distributed uniformly. Then, the $ABCD$ matrix of each segment is calculated using (2.20). Then, the total $ABCD$ matrix of the whole network is calculated by modifying (2.21) to include the effect of the resistors as follows:

$$\begin{aligned}
 [A \ B; C \ D]_{\text{Total}} &= [A \ B; C \ D]_{\frac{R_3}{2}} \cdot \prod_{m=80}^{55} [AB; CD]_m \cdot [A \ B; C \ D]_{\frac{R_2}{2}} \\
 &\prod_{m=54}^{28} [A \ B; C \ D]_m \cdot [A \ B; C \ D]_{\frac{R_1}{2}} \cdot \prod_{m=27}^1 [A \ B; C \ D]_m
 \end{aligned} \tag{3.1}$$

It is paramount to point out that the product starts from the load side and this

explains why the product is done in descending order. Then, as illustrated in Figure 3-3, the following equation can be written:

$$\begin{bmatrix} V_1 \\ I_1 \end{bmatrix} = \begin{bmatrix} A & B \\ C & D \end{bmatrix}_{\text{Total}} \begin{bmatrix} V_2 \\ I_2 \end{bmatrix} \quad (3.2)$$

By setting V_2 in (3.2) to zero and solving for V_1/I_1 , one obtains:

$$\frac{V_1}{I_1} = \frac{B}{D} = Z_{in}^o \quad (3.3)$$

For perfect output port matching, the following condition should be satisfied:

$$\Gamma_{\text{out}}(f_k) = \frac{Z_{\text{in}}^o(f_k) - Z_l}{Z_{\text{in}}^o(f_k) + Z_l} = 0 \quad (3.4)$$

where f_k ($k = 1, 2, \dots, n$) denotes the frequencies at which (3.4) is calculated. Therefore, for a perfect output ports matching over the desired range, the following error should be minimized:

$$\text{Error}_{\text{out}} = \sum_{k=1}^K |\Gamma_{\text{out}}(f_k)|^2 \quad (3.5)$$

This optimization problem is solved keeping in mind that R_1 , R_2 , and R_3 are the optimization variables to be determined.

3.2 Results

Based on the design procedure presented in Section 3.1, an example of an equal-split filtering PD is designed and simulated. The design is optimized taking into account a 0.3048-mm-thick Rogers RO4003C substrate with a relative permittivity $\epsilon_r = 3.55$. The physical parameters are listed in Table 3.2. The PD has a center frequency of 12.0 GHz and fractional bandwidth (FBW) of 3.3%. The number of the

Table 3.2: List of Physical Dimensions of the HMSIW WPD

Parameter	Value (mm)	Parameter	Value (mm)
d	0.50	w_{min}	2.50
s	0.90	l	35.0
$w(x = 0, l)$	13.0	w_{50}	0.68
$w_r = w_{max}$	12.4	$w_{\mu s}$	1.5
l_p	4.5	w_s	1.0

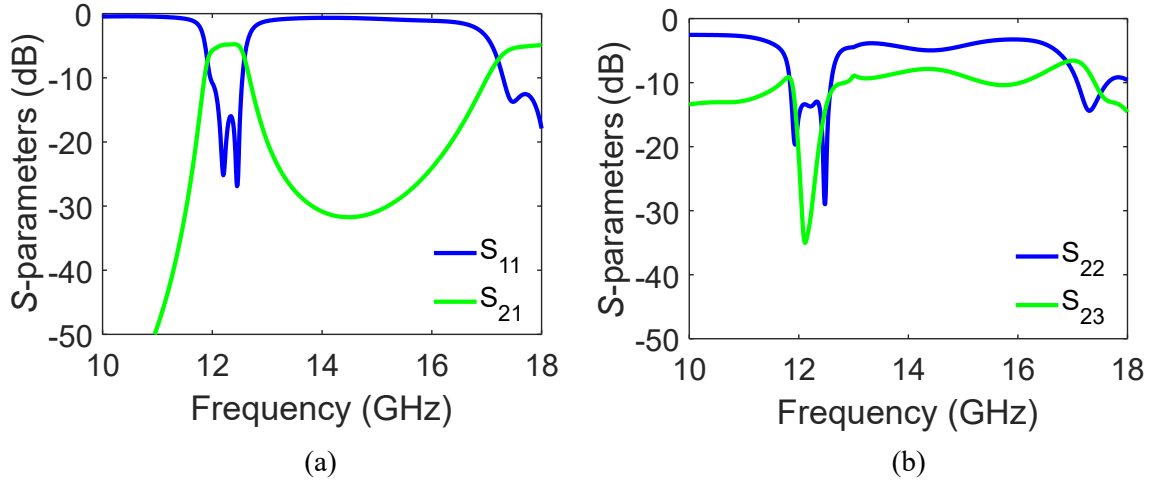
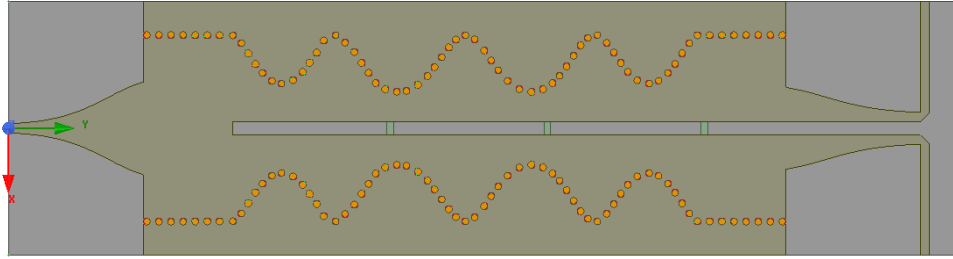


Figure 3-4: Simulated S -Parameters of the designed HMSIW-based filtering PD: (a) S_{11} and S_{21} and (b) S_{22} and S_{23} .

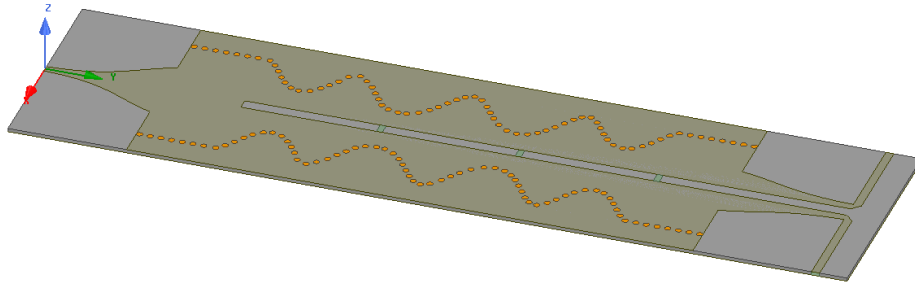
Fourier series coefficients, N , and the uniform segments, M , are chosen to be 13 and 25, respectively. The optimum values of the isolation resistors are found to be $R_1 = 500\Omega$, $R_2 = 100\Omega$, $R_3 = 350\Omega$.

Simulated input port matching and transmission parameters are presented in Figure 3-4(a), whereas output port matching and isolation are shown in Figure 3-4(b). The PD has input port matching and transmission loss better than -16 dB and -2.5 dB, respectively. The output port matching and isolation between the output ports are better than -13 dB and -16 dB, respectively, across the operating band. Figure 3-5 shows the simulated layout using ANSYS Electronics Desktop [98].

Table 3.3 presents a comparison between the proposed HMSIW PD and other



(a)



(b)

Figure 3-5: Simulated layout of the designed HMSIW-based PD: (a) top view and (b) trimetric view.

state-of-the-art PDs. The proposed methodology shows competitive electrical performance as compared to other reported techniques. The proposed PD has the maximum input matching and isolation levels among the reported PDs. Although insertion losses are higher for narrowband SIW filters/PDs [27], the proposed design has acceptable insertion loss compared to other broader PDs. The proposed technique offers design flexibility and bandpass redefinition without using extra components (e.g., stubs, lumped elements).

3.3 Conclusion

This chapter presented a novel procedure for designing filtering WPDs based on E-wall-varied SIW transmission lines governed by a truncated Fourier series expansion with the series coefficients being variables to be optimized. The even-mode analysis

was used to optimize the transmission lines that operate well across predefined bandwidth, whereas three isolation resistors were calculated using the odd mode circuit. Furthermore, half-mode structure is used to cut down the size of the PD in half. The proposed methodology is systematic and results in planar PDs with competitive electrical characteristics. For verification purposes, a PD is designed and simulated. Simulated results are in a good agreement and show a matching better than -13 dB and competitive transmission losses in both pass- and stop-bands.

Table 3.3: Comparison between the Proposed filtering PD and Other State-of-the-art SIW PDs

Ref.	f_0 (GHz)	10-dB FBW (%)	Ports Matching (dB)	Isolation (dB)	Insertion loss (dB)	Area* (λ_g^2)	Filtering Response
[41]	10.1	21.7	12.0	15.0	3.6	2.4	No
[43]	12.6	4.4	N/A	N/A	3.8	8.6	Yes
[44]	5.5	3.6	N/A	N/A	5.0	0.4	Yes
[45]	5.2	9.7	17.0	15.0	4.6	2.4	Yes
[46]	8.9	2.6	12.0	16.0	6.5	3.4	Yes
[47]	11.0	2.4	20.0	25.0	6.0	4.4	Yes
[48]	10.0	3.5	11.0	N/A	5.5	3.0	Yes
[56]	18.00	11.1	10.0	10.0	8.0	2.6	No
This Work	12.2	3.3	13.0	18.0	5.5	2.1	Yes

* Feedlines and ports are not included in the calculation of the occupied area

Chapter 4

Impedance-varying N -way Microstrip Wilkinson Power Divider

In this chapter, a systematic procedure for designing a multi-way WPD with bandwidth redefinition characteristics. The designed structure is compact and planar. Quarter-wave matching uniform transmission lines in the conventional design are replaced with non-uniform transmission lines (NTLs) governed by a truncated Fourier series. Even-mode analysis is adopted to obtain NTLs with predefined bandwidth functionalities; whereas several isolation resistors are optimized in the odd mode analysis to achieve proper isolation and output ports matching over the frequency range of interest. Compactness is achieved by incorporating only one quarter-wave wideband NTL transformer, with a length computed at the center frequency, in each arm.

This chapter is organized as follows: Section 4.1 presents the detailed design procedure of the proposed wideband NTL N -way WPD. Analytical, simulated, and measured results of 3- and 4-way WPDs across different design bands are presented in Section 4.2. Finally, conclusions are drawn in Section 4.3.

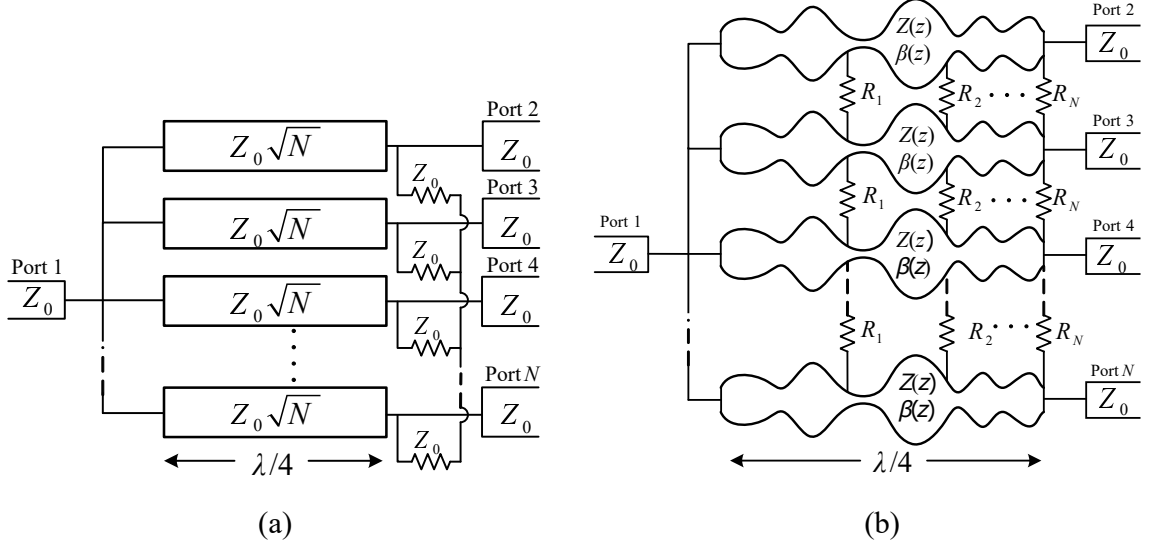


Figure 4-1: Schematic diagrams of N -way WPDs: (a) conventional single-frequency and (b) proposed wideband.

4.1 N -way Microstrip WPD Design

In this section, the design procedure of a compact wideband microstrip-based WPD is elaborated. A schematic diagram of a single frequency conventional N -way WPD along with its counterpart proposed wideband divider are shown in Figure (4-1). The proposed approach is based on replacing the uniform quarter-wave transformers by impedance-varying transmission lines that operate across predefined bands. The design starts by reducing the N -way divider to its equivalent 2-way model [109]. Hence, the even-/odd-mode analysis can be adopted.

To reduce the N -way divider to its 2-way equivalent model, the first branch is assumed to be the n^{th} branch, whereas the second is a combination of the remaining $N - 1$ branches, as shown in Figure 4-2. The analysis starts by assigning the power split ratio at each output port, then applying the combining technique presented in [109] to find the characteristic impedance of each n^{th} branch. For simplicity, the equal-split power divider is considered. Thus, each port will receive $1/N$ fraction of the total input power. The power at the other branch in the equivalent 2-way model

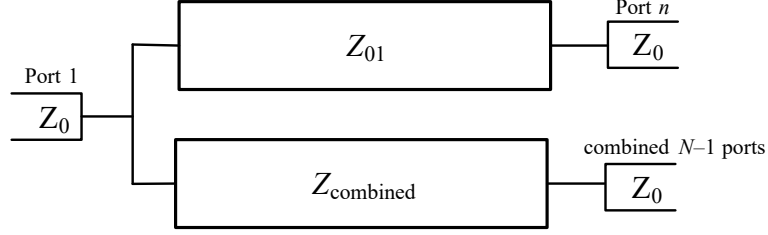


Figure 4-2: 2-way equivalent model of the N -way WPD.

is the sum of the power ratios of the rest of the $N - 1$ branches; or in other words, $(N - 1)/N$. Once the characteristic impedance of the n^{th} branch is determined, the process is repeated until the characteristic impedances of all N original branches are found. In this context, the equivalent 2-way model is developed only once as the power is split equally between the N output ports (i.e., same characteristic impedances for all N branches). 3- and 4-way WPD configurations will be considered to continue the design procedure. For the 3-way WPD, each uniform quarter-wave transformer has a characteristic impedance of $Z_0\sqrt{3} = 86.6\Omega$ (assuming a port impedance of 50Ω). To obtain the characteristic impedance of the first branch, Z_{01} , for the equivalent 2-way model shown in Figure 4-2, we combine branches 2 and 3 (i.e., ports 3 and 4), where $k_2 = P_{3,4}/P_2$. The combined power of ports 3 and 4 is twice the power of port 2, so $k^2 = 2$, and Z_{01} is be found to be $Z_0\sqrt{k(1+k_2)} = 103\Omega$ [109]. Since the proposed design is of equal split, the other branches will have the same value of Z_{01} . Similarly, $k^2 = 3$ and $Z_{01} = 131.6$ for the 4-way divider.

4.1.1 Even-mode Analysis

The even-mode equivalent circuit of the proposed N -way divider is shown in Figure 4-3. The NTL has a length d with a varying characteristic impedance $Z(x)$ and propagation constant $\beta(x)$, and matches a source impedance Z_s to a load impedance Z_l . The isolation resistors $R_j/2$, where $j = 1, 2, 3$, are terminated with an open circuit as a result of the symmetric excitation at the two equivalent output ports. To

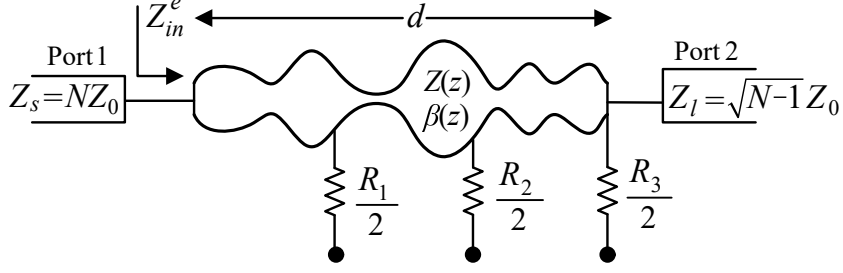


Figure 4-3: 2-way equivalent even-mode circuit of the proposed NTL N -way WPD.

design the NTL, the magnitude of the reflection coefficient, $|\Gamma|$, should be zero (or very small) over the frequency range of interest. $|\Gamma|$ at the input port is expressed in terms of Z_{in}^e shown in Figure 4-3, where Z_{in}^e is calculated after obtaining the $ABCD$ parameters of the NTL.

In a similar analysis presented in Section 2.2, the $ABCD$ parameters of the wide-band matching NTL are calculated by subdividing it into $K = 50$ uniform short segments each of length $\Delta x = d/K$ where $\Delta x \ll \lambda$, where λ is the guided wavelength at the center frequency. Then, the $ABCD$ matrix of the whole NTL is obtained by multiplying the $ABCD$ parameters of all sections as follows:

$$[A \ B; C \ D]_{Z(x)} = \prod_{i=1}^K [A \ B; C \ D]_i \quad (4.1)$$

where the $ABCD$ parameters of the i^{th} ($i = 1, 2, \dots, K$) segment are [95]:

$$A_i = D_i = \cos(\Delta\theta) \quad (4.2a)$$

$$B_i = Z^2((i - 0.5)\Delta x)C_i = jZ((i - 0.5)\Delta x) \sin(\Delta\theta) \quad (4.2b)$$

$$\Delta\theta = \frac{2\pi}{\lambda}\Delta x = \frac{2\pi}{c}f\sqrt{\epsilon_{eff}}\Delta x \quad (4.2c)$$

where c is the speed of light and f is the center frequency of the design bandwidth. The effective dielectric constant, ϵ_{eff} , of each section is found using the well-known

microstrip line formula [95]:

$$\epsilon_{eff} = \frac{\epsilon_r + 1}{2} + \frac{\epsilon_r - 1}{2} \frac{1}{\sqrt{1 + 12h/W}} \quad (4.3)$$

where h is the dielectric substrate thickness and W is the width of the microstrip line. Given Z_0 and dielectric constant ϵ_r , the ratio h/W in (4.3) can be found as:

$$\frac{W}{h} = \begin{cases} \frac{8e^A}{e^{2A}-2} & \text{for } W/h < 2 \\ \frac{2}{\pi} \left[B - 1 - \ln(2B - 1) + \frac{\epsilon_r - 1}{2\epsilon_r} \left\{ \ln(B - 1) + 0.39 - \frac{0.61}{\epsilon_r} \right\} \right] & \text{for } W/h > 2 \end{cases} \quad (4.4)$$

where

$$A = \frac{Z_0}{60} \sqrt{\frac{\epsilon_r + 1}{2}} + \frac{\epsilon_r - 1}{\epsilon_r + 1} \left(0.23 + \frac{0.11}{\epsilon_r} \right) \quad (4.5a)$$

$$B = \frac{377\pi}{2Z_0\sqrt{\epsilon_r}} \quad (4.5b)$$

The term $x = (i - 0.5)\Delta x_i$ in (4.2) represents the center of each segment, i . Furthermore, the non-uniform impedance profile is governed by a truncated Fourier series that is expressed as:

$$Z(x) = Z_{01} \exp \left[c_0 + \sum_{m=1}^M \left(a_m \cos \left[\frac{2\pi m x}{d} \right] + b_m \sin \left[\frac{2\pi m x}{d} \right] \right) \right] \quad (4.6)$$

where $Z_{01} = \sqrt{Z_s Z_l}$ is the characteristic impedance of the WPD branch. It is worthy to mention that (2.9) is a reduced form from (4.6). Although the downgraded series form in (2.9) reduces the optimization time considerably, the usage of (4.6) leads to a better performance due to allowing more impedance variations along the NTL.

An optimum designed NTL has its reflection coefficient magnitude over the fre-

quency range of interest, with an increment of Δf as close as possible to zero. In this context, Δf is chosen to be 0.2 GHz. Therefore, the optimum values of the Fourier coefficients can be obtained through minimizing the following error function [110]:

$$\text{Error}_{\text{in}} = \max (E_{f_1}^{\text{in}}, \dots, E_{f_k}^{\text{in}}, \dots, E_{f_n}^{\text{in}}) \quad (4.7)$$

where

$$E_{f_k}^{\text{in}} = |\Gamma_{\text{in}}(f_k)|^2 \quad (4.8)$$

$$\Gamma_{\text{in}}(f_k) = \frac{Z_{\text{in}}^e(f_k) - Z_s}{Z_{\text{in}}^e(f_k) + Z_s} \quad (4.9)$$

$$Z_{\text{in}}^e(f_k) = \frac{A(f_k)Z_l + B(f_k)}{C(f_k)Z_l + D(f_k)} \quad (4.10)$$

The resulting $Z(x)$ must be within reasonable fabrication tolerances and meet matching conditions. That is, the following physical constraints are set:

$$Z_{\text{min}} \leq Z(x) \leq Z_{\text{max}} \quad (4.11)$$

To minimize the non-linear bound-constrained error function in (4.7) across a predefined bandwidth, an optimization procedure is carried out, in which the series coefficients, c_0, a_m, b_m , are set as the variables to be optimized. It is noteworthy to point out that such coefficients $\in [-1, 1]$. In this context MATLAB built-in function "fmincon.m" is used due to its ability to converge in a relatively small optimization time.

4.1.2 Odd-mode Analysis

Figure 4-4 shows the equivalent odd-mode circuit of the proposed divider which is used to obtain the optimum values of the isolation resistors that achieve acceptable output ports isolation and matching conditions. Due to the asymmetric excitation of

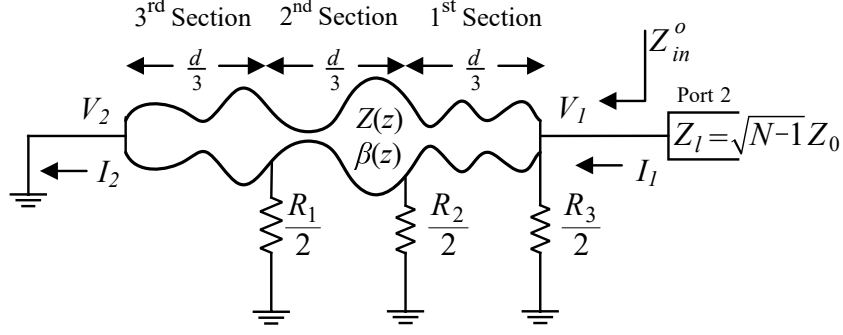


Figure 4-4: 2-way equivalent odd-mode circuit of the proposed NTL N -way WPD.

the output ports, each $R_j/2$ resistor will be terminated with a short circuit.

After determining the optimum values of the Fourier series coefficients in (4.6), the NTL transformer is subdivided into 3 sections, and the $ABCD$ matrix for each section is calculated by employing (4.1) and (4.2). Then, the total $ABCD$ matrix of the whole network shown in Figure 4-4 can be calculated as follows:

$$\begin{aligned}
 [A \ B; C \ D]_{\text{Total}} &= [A \ B; C \ D]_{\frac{R_3}{2}} \cdot [A \ B; C \ D]_{\text{1st Section}} \cdot [A \ B; C \ D]_{\frac{R_2}{2}} \cdot \\
 & [A \ B; C \ D]_{\text{2nd Section}} \cdot [A \ B; C \ D]_{\frac{R_1}{2}} \cdot [A \ B; C \ D]_{\text{3rd Section}}
 \end{aligned} \tag{4.12}$$

It is worth to point out here that the locations of the resistors are distributed uniformly. Finally, and as illustrated in Figure 4-4, the following equation can be written:

$$\begin{bmatrix} V_1 \\ I_1 \end{bmatrix} = \begin{bmatrix} A & B \\ C & D \end{bmatrix}_{\text{Total}} \begin{bmatrix} V_2 \\ I_2 \end{bmatrix} \tag{4.13}$$

By setting V_2 in (4.13) to zero and solving for V_1/I_1 , one obtains:

$$\frac{V_1}{I_1} = \frac{B}{D} = Z_{in}^o \tag{4.14}$$

For perfect output port matching, the following condition should be satisfied:

$$\Gamma_{\text{out}}(f_k) = \frac{Z_{\text{in}}^{\circ}(f_k) - Z_l}{Z_{\text{in}}^{\circ}(f_k) + Z_l} = 0 \quad (4.15)$$

where f_k ($k = 1, 2, \dots, n$) denotes the frequencies at which (4.15) is calculated. Therefore, for a perfect output ports matching over the desired range, the following error should be minimized [110]:

$$\text{Error}_{\text{out}} = \max(E_{f_1}^{\text{out}}, \dots, E_{f_k}^{\text{out}}, \dots, E_{f_n}^{\text{out}}) \quad (4.16)$$

where

$$E_{f_k}^{\text{out}} = |\Gamma_{\text{out}}(f_k)|^2 \quad (4.17)$$

This optimization problem is solved keeping in mind that R_1 , R_2 , and R_3 are the optimization variables to be determined.

4.2 Results

In this section, based on the design procedure provided in Section 4.1, 3- and 4-way WPDs operating at different frequency bands are demonstrated followed by simulated and measured results for further verification.

4.2.1 Analytical Results

3- and 4-way WPDs operating at 6–8 GHz, 5–9 GHz, and 4–10 GHz, which correspond to FBWs of 28%, 57%, and 86%, respectively, are designed. All design examples are carried out using Rogers RO4003C substrate with a thickness of 0.813 mm, relative permittivity of 3.55, and loss tangent of 0.0027. The length of each NTL transformer of the proposed WPDs is set to 10 mm. The characteristic impedance of

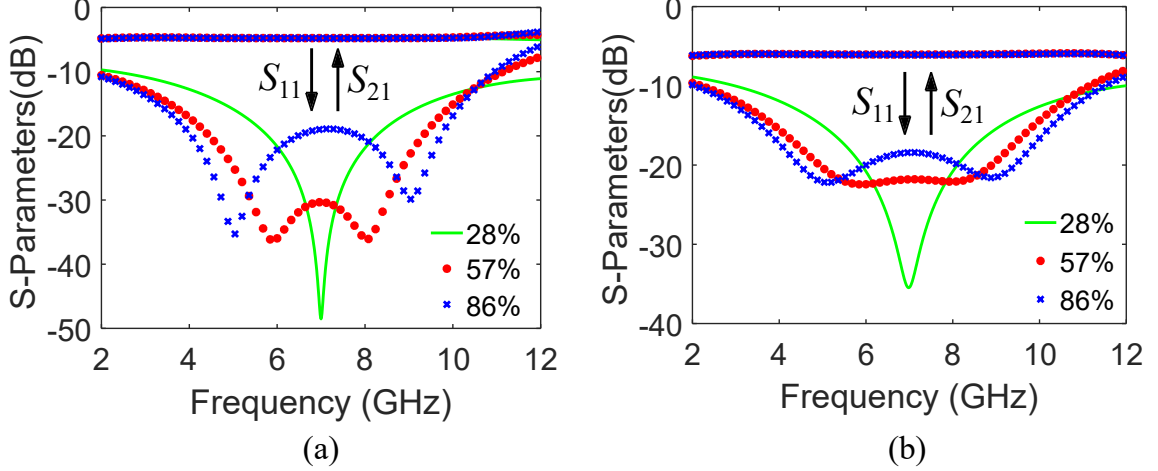


Figure 4-5: S-parameters (S_{11} and S_{21}) for the wideband NTL matching transformers across the design bands 6-8 GHz, 5-9 GHz, and 4-10 GHz: (a) 3-way case: $Z_s = 150\Omega$, $Z_l = 70.71\Omega$, and (b) 4-way case: $Z_s = 200\Omega$, $Z_l = 86.6\Omega$.

the conventional 3-way WPD arm, z_{01} , is calculated in Section 4.1 and is found to be equal 103Ω , whereas it equals to 131.6Ω in the 4-way divider example. Z_{min} and Z_{max} in (4.11) are chosen to be 21Ω and 138Ω , respectively. The resulting Fourier coefficients and the associated optimization error in each case are presented in Tables 4.1 and 4.2 for the 3- and 4-way cases, respectively.

Figure 4-5 shows the analytical response of the input port matching and transmission parameters, S_{11} and S_{21} , respectively, for the wideband NTL matching transformers across the design bands: 6–8 GHz, 5–9 GHz, and 4–10 GHz. The S -parameters are calculated using the following equations (assuming lossless transmission lines):

$$S_{11} = 20 \log \left(\frac{A_{Z(z)}Z_l + B_{Z(z)} - C_{Z(z)}Z_sZ_l - D_{Z(z)}Z_s}{A_{Z(z)}Z_l + B_{Z(z)} + C_{Z(z)}Z_sZ_l + D_{Z(z)}Z_s} \right) \quad (4.18a)$$

$$S_{21} = 20 \log \left(\sqrt{(1 - S_{11}^2)/N} \right) \quad (4.18b)$$

where $Z_s = NZ_0$ and $Z_l = \sqrt{N-1}Z_0$ are the source and load impedances, respec-

Table 4.1: Fourier Coefficients for the Impedance-varying Profiles of Three
3-Way WPD Examples

FBW (%)	c_0	a_1	a_2	a_3	a_4	a_5	b_1	b_2	b_3	b_4	b_5	Error
28	-0.0053	-0.0079	0.0537	0.0240	-0.0309	-0.0184	-0.0270	0.0017	-0.0021	0.0013	-0.0079	0.0035
57	-0.0139	-0.0346	0.2613	0.1229	-0.1907	-0.0921	-0.1491	0.0125	-0.0260	0.0069	-0.0413	0.0067
86	-0.0127	-0.0267	0.2175	0.0972	-0.2300	-0.0732	-0.1594	0.0176	-0.0119	0.0362	-0.0286	0.0127

Table 4.2: Fourier Coefficients for the Impedance-varying Profiles of Three
4-Way WPD Examples

FBW (%)	c_0	a_1	a_2	a_3	a_4	a_5	b_1	b_2	b_3	b_4	b_5	Error
28	-0.1343	-0.1155	0.1813	-0.0059	0.0877	-0.0015	0.0439	-0.0049	0.0100	0.0137	0.0207	0.0059
57	-0.0980	-0.0213	0.2159	0.1052	0.0074	-0.0123	-0.0311	-0.0046	0.0114	0.0032	-0.0003	0.0083
86	-0.0777	-0.0061	0.1914	0.0876	0.0060	0.0016	-0.0089	0.0143	0.0008	0.0004	-0.0070	0.0206

tively, found in the even-mode analysis. Input port matching is below -17 dB for the 3-way dividers, and the transmission parameters are in close proximity to their theoretical value of -4.77 dB over the bands of interests. Furthermore, the input port matching is below -16 dB over the three bands in all $N = 4$ divider examples and the transmission parameters are close to their theoretical value of -6 dB over the bands of interests.

4.2.2 Simulations and Measurements

In this section, 3- and 4-way WPDs with FBWs of 57% are simulated. Simulations are performed with the finite element method-based tool ANSYS HFSS [98]. Furthermore, a 3-way WPD with a FBW of 86% is fabricated and measured. Figure 4-6(a) illustrates the simulated results for the input port matching and transmission parameters of the 3-way WPD over a band of 5–9 GHz (i.e. FBW of 57%). It should be indicated that $S_{21} = S_{41}$ due to structure symmetry. Simulation results show that input port matching is below -15 dB and the transmission parameters equal -4.9 ± 1 dB over 5–9 GHz. Output port matching and isolation parameters are all below -15 dB in the assigned band as depicted in Figure 4-6(b). It should be noted that $S_{22} = S_{44}$ and $S_{23} = S_{34}$ due to structural symmetry. The optimum values of the isolation resistors are found to be $R_1 = 120 \Omega$, $R_2 = 660 \Omega$, and $R_3 = 360 \Omega$.

The input port matching and transmission parameters for the 4-way WPD across a band of 5–9 GHz are presented in Figure 4-7(a); whereas the output port matching and isolation parameters are provided in Figure 4-7(b). Due to structural symmetry, $S_{21} = S_{51}$ and $S_{31} = S_{41}$. Simulated input port matching is below -14 dB and the transmission parameters are equal to -6.2 ± 1 dB. All output port matching and isolation parameters are below -13 dB over 5–9 GHz as depicted in Figure 4-7(b). It should be noted that $S_{22} = S_{44}$ and $S_{34} = S_{23}$. Four resistors between each two NTLs are used in this 4-way WPD and their values are found to be $R_1 = 200 \Omega$,

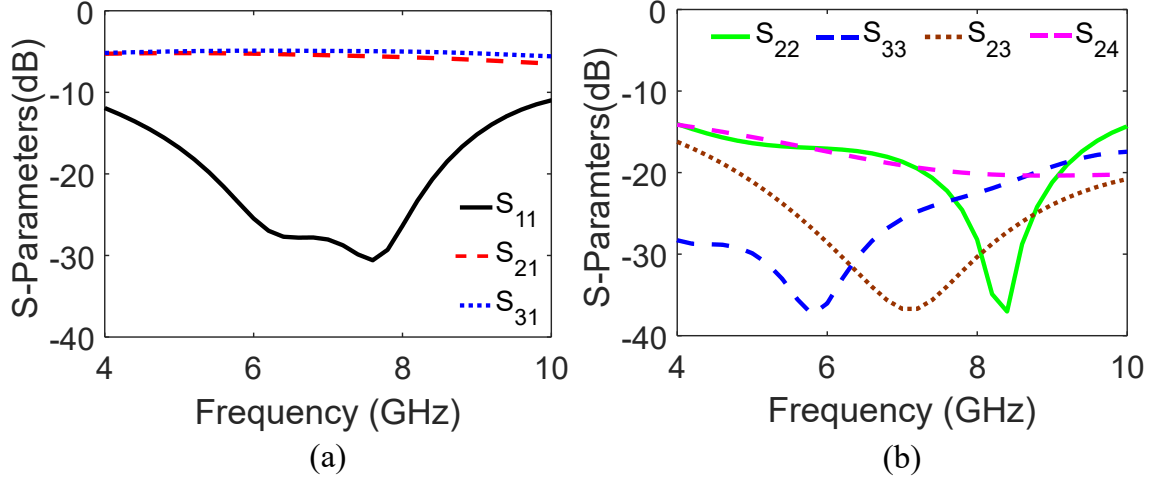


Figure 4-6: Simulated S -parameters of the wideband 3-way WPD with FBW of 57%: (a) input port matching and transmission parameters, and (b) output port matching and isolation parameters.

$R_2 = 980 \Omega$, $R_3 = 370 \Omega$, and $R_4 = 160 \Omega$.

Figure 4-8 shows a photograph of the fabricated 3-way power divider built with the previously mentioned substrate. The optimum values of the resistors are found to be $R_1 = 120 \Omega$, $R_2 = 480 \Omega$, and $R_3 = 320 \Omega$. Figure 4-9 represents the simulated and measured S -parameters of the 3-way WPD with fractional bandwidths of 86%.

Simulations and measurements show that the input port matching is less than -12 dB over the band of interest. The transmission parameters are equal to -4.9 ± 1 dB over 4–10 GHz. The small discrepancies between the simulated and measured results are thought to be due to fabrication tolerances, soldering and measurement errors.

Simulated and measured output ports matching and isolation parameters of the 4–10 GHz 3-way WPD are given in Figure 4-10, which indicates a good agreement between both results, and show output ports matching and isolation of below -13 dB over the desired frequency range.

Structural symmetry of the fabricated prototype is assessed by measuring the magnitude and the phase imbalances. As shown in Figure 4-11(a), the measured

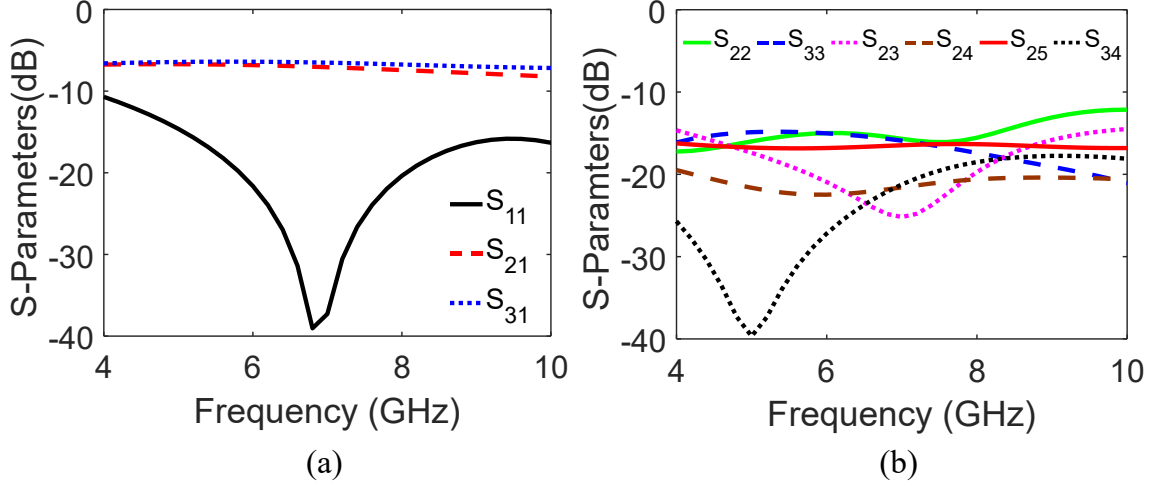


Figure 4-7: Simulated S -parameters of the proposed 4-way WPD with a FBW of 57%: (a) input port matching and transmission parameters and (b) output port matching and isolation parameters.

magnitude imbalance equals ± 0.37 dB; whereas the phase imbalance is measured to be $\pm 5.4^\circ$ over the design bandwidth as indicated in Figure 4-11(b). Such results indicate an excellent symmetry of the fabricated layout. In addition, measured group delays of the fabricated 3-way divider are depicted in Figure 4-12. Measured results show almost constant response of 0.18 ns for both S_{21} and S_{31} over the 4–10 GHz band.

Table 4.3 provides a comparison between the measured and simulated results of the proposed wideband 3- and 4-way WPDs, respectively, and other state-of-the-art N -way power dividers. It can be shown from table 4.3 that our proposed dividers operate over wider frequency bands as compared to many previously proposed WPDs and at the same time have small arm lengths (i.e. compact size. Since insertion loss is proportional to frequency, the proposed dividers have higher losses as their frequency of operation extends to 10 GHz).

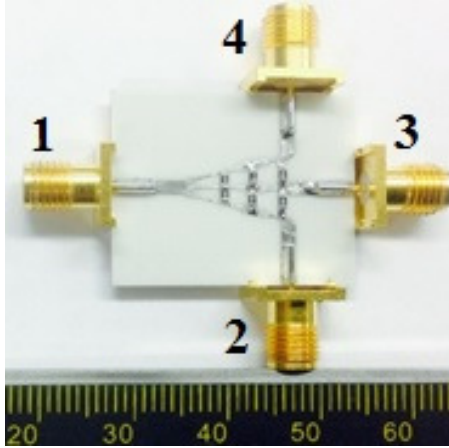


Figure 4-8: Photograph of the fabricated 3-way WPD structure operating over a band of 4–10 GHz.

4.3 Conclusions

The concept of Fourier-based impedance-varying profiles of wideband frequency matching characteristic is adopted in the design of compact wideband N -way WPDs. A combining technique was used to reduce the N -way divider to its equivalent 2-way model. Then, the even mode analysis was used to obtain the NTLs that operate well across predefined wideband. The isolation resistors were calculated using the odd mode circuit. For verification purposes, three power dividers were designed and simulated. Furthermore, a 3-way power divider with fractional bandwidth of 86% was fabricated and measured. The good agreement between both simulation and measurement results over the assigned frequency band proves the validity of the design procedure. The differences between simulation and experimental results could be due to the fabrication process, the effect of the connectors, and measurement errors.

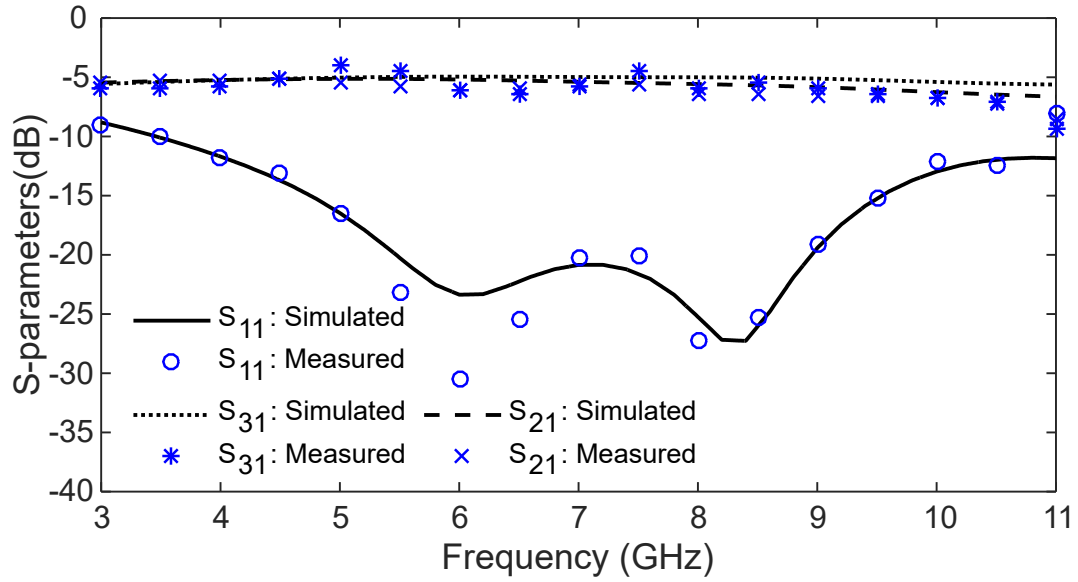


Figure 4-9: Simulated and measured S -parameters of the 3-way WPD with FBW of 86%.

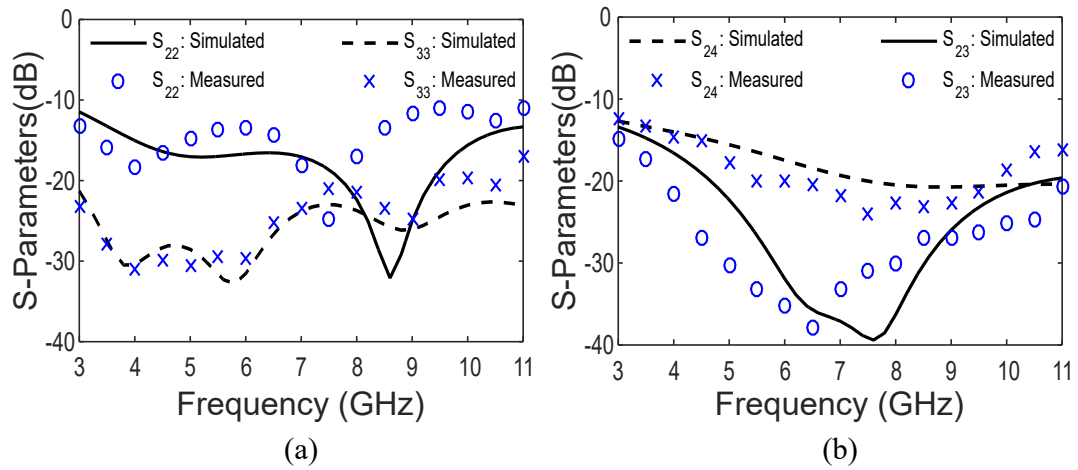


Figure 4-10: Simulated and measured results of: (a) output ports matching, and (b) isolation of the proposed wideband 3-way WPD.

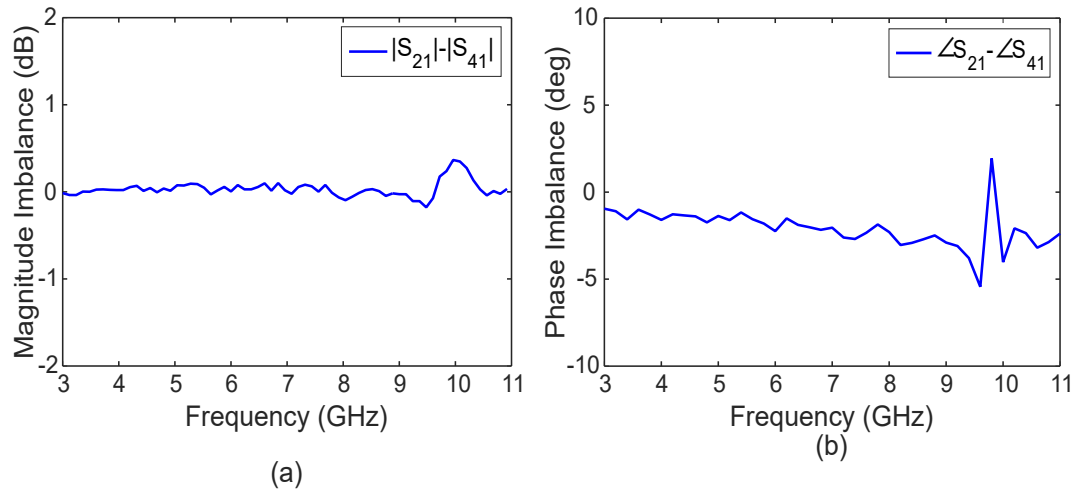


Figure 4-11: Measured imbalance of the proposed wideband 3-way WPD: (a) magnitude and (b) phase.

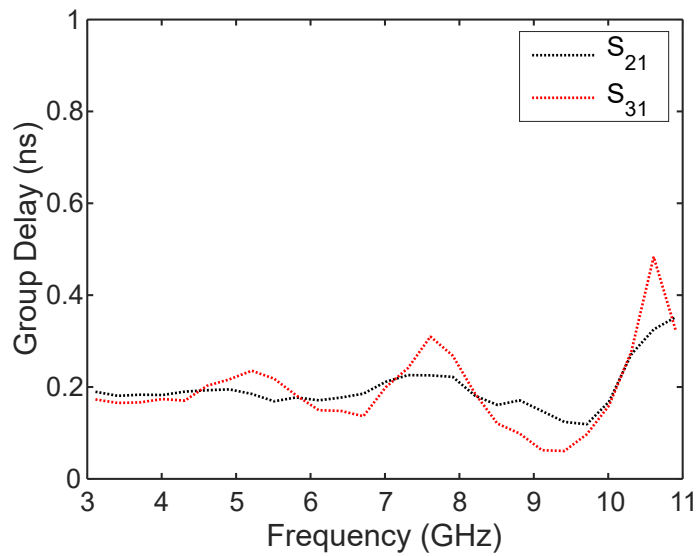


Figure 4-12: Measured group delays of the proposed 3-way WPD over the 4-10 GHz band.

Table 4.3: Comparison between Electrical and Physical properties of the Proposed NTLs N -Way WPDs and recent Wideband Power Dividers

Ref.	Design approach	f_c (GHz)	Operating BW (GHz)	Ports matching (dB)	Insertion variations (dB)	No. of stages	Total arm length (in terms of λ_c)
[57]	2-way hybrid WPD using capacitive and inductive elements in both stages	1.55	0.3-2.8	-10	0.3	2	$\lambda_c/2$
[58]	2-way 180° WPD implemented in parallel-strip-line	4.5	0.6-8.0	-10	1.1	3	$3\lambda_c/4$
[59]	2-way WPD based on replacing each quarter-wave branch by 4 transmission line sections*	2.25	0.5-4.0	-12	0.24	4	λ_c
[62]	3-way power divider based on microstrip coupled line technology	2.6	1.6-3.6	-10	0.3	1	$\lambda_c/4$
[63]	3-way WPD using tapered line transformers	7.0	2-12	-10	1.8	1	$0.9\lambda_c$
[64]	4-way divider by cascading 3 WPDs in two stages connected by transmission lines with lengths of $5\lambda_c/4$	6.0	4-8	-10	1.2	2	$7\lambda_c/4$
[65]	8-way divider by cascading 7 WPDs in three stages connected by transmission lines with lengths of $3\lambda_c/4$ and $\lambda_c/4$	5.75	2.9-8.6	-15	1.5	3	$7\lambda_c/4$
This Work	3-way WPD using impedance-varying profiles governed by truncated Fourier series	7.0	4-10	-12	1.2	1	$\lambda_c/4$
This Work	4-way WPD using impedance-varying profiles governed by truncated Fourier series*	7.0	5-9	-13	1.3	1	$\lambda_c/4$

Chapter 5

Coplanar Waveguide Transformers for RF Circuitries on Flexible Substrates

Impedance matching transformers are widely utilized as matching networks for many microwave components, such as antennas, power dividers, and power amplifiers. However, conventional transformers can achieve perfect impedance matching at only a single frequency. Consequently, broadening the operating bandwidth while maintaining same desired scattering parameters is of utmost importance. In this chapter, a novel approach for developing miniaturized CPW transformers is presented. The proposed transformers match a load impedance, Z_l , to a source impedance, Z_s at single-, multi-, and wide-band. Moreover, the proposed CPW-based transformers are implemented on liquid crystal polymer (LCP), which is a widely used flexible substrate that is being explored for high frequency applications [71, 111]. Liquid crystal polymer (LCP) substrate was used here due to its excellent performance at high-frequency, characterized by the low loss, near hermetic nature, and low cost.

The remaining of this chapter is organized as follows: Section 5.1 discusses the analytical equations and the proposed optimization-driven framework to design the

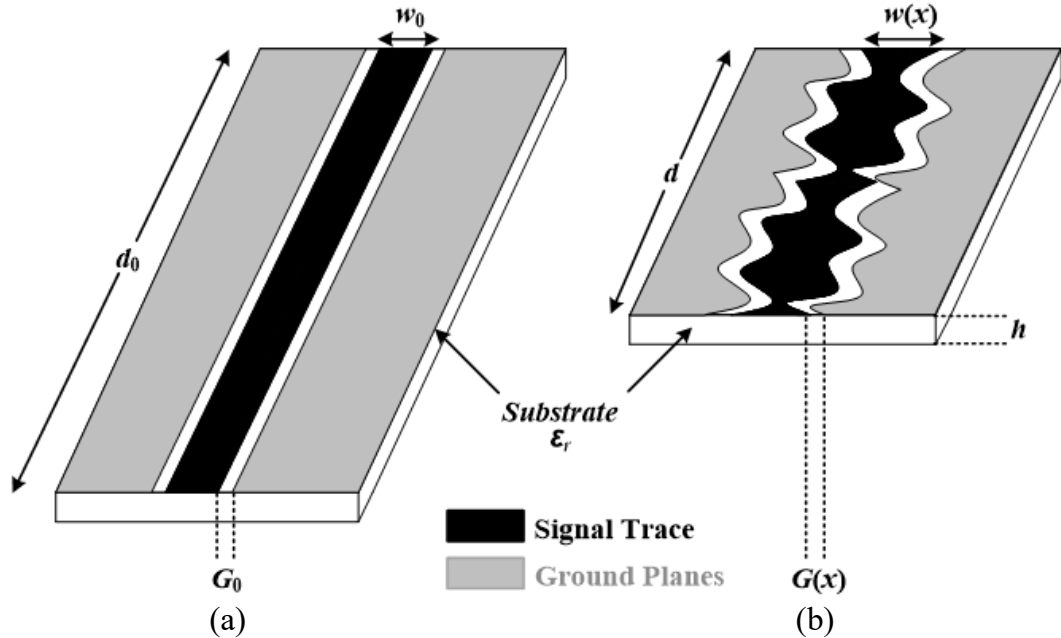


Figure 5-1: A CPW impedance matching transformer that matches a load impedance, Z_l , to a source impedance, Z_s : (a) conventional and (b) proposed miniaturized transformers.

CPW transformers. EM Simulations and measurements are given in Section 5.2. In section 5.3, conclusions are drawn.

5.1 CPW Matching Transformers Design

Schematic diagrams of the CPW-based conventional and proposed matching transformers are shown in Figure 5-1. It can be noted that the signal trace and the adjacent ground planes in the conventional CPW structure are width-modulated along the propagation path of the EM wave while maintaining a constant ground-trace separation. The design starts by subdividing the width-modulated signal trace, $w(x)$, into U uniform CPW segments each of length Δx , and then modeled in a truncated Fourier series form given as [94]:

$$w(x) = w_{ref} \exp \left[c_0 + \sum_{n=1}^N \left(a_n \cos \left[\frac{2\pi n x}{d} \right] + b_n \sin \left[\frac{2\pi n x}{d} \right] \right) \right] \quad (5.1)$$

where w_{ref} is a reference width, N is the number of series coefficients and d is a predefined length of the compact matching transformer. The effective dielectric constant, ϵ_{eff} , of each segment is given by [112]:

$$\epsilon_{eff} = 1 + \frac{\epsilon_r - 1}{2} \frac{K(k_1)}{K(k_1')} \frac{K(k')}{K(k)} \quad (5.2)$$

where

$$k = \frac{W(x)}{W(x) + 2G(x)}$$

$$k_1 = \frac{\sinh \left(\frac{\pi W(x)}{4h} \right)}{\sinh \left(\frac{(W(x) + 2G(x))\pi}{4h} \right)} \quad (5.3)$$

where $k' = \sqrt{1 - k^2}$ and K is the complete elliptic integral of the first kind k' and it can be approximated by [113]:

$$\frac{K(k)}{K(k')} \approx \begin{cases} \frac{1}{2\pi} \ln \left[2 \frac{\sqrt{1+k} + \sqrt[4]{4k}}{\sqrt{1+k} - \sqrt[4]{4k}} \right] & \text{for } 1 \leq \frac{K}{K'} \leq \infty \quad \text{and} \quad \frac{1}{\sqrt{2}} \leq k \leq 1 \\ \frac{2\pi}{\ln \left[2 \frac{\sqrt{1+k'} + \sqrt[4]{4k'}}{\sqrt{1+k'} - \sqrt[4]{4k'}} \right]} & \text{for } 0 \leq \frac{K}{K'} \leq 1 \quad \text{and} \quad 0 \leq k \leq \frac{1}{\sqrt{2}} \end{cases} \quad (5.4)$$

Upon determining the effective permittivity at point x in the transmission line according to the corresponding width variation, the characteristic impedance, $Z(x)$, can then be calculated as follows [112]:

$$Z(x) = \frac{30\pi}{\sqrt{\epsilon_{eff}}} \frac{K(k')}{K(k)} \quad (5.5)$$

Once ϵ_{eff} and Z_0 are found, the $ABCD$ parameters of the i^{th} segment ($i =$

1, 2, \dots, U) is obtained such that [95]:

$$A_i = D_i = \cos(\Delta\theta) \quad (5.6a)$$

$$B_i = Z^2((i - 0.5)\Delta x)C_i = jZ((i - 0.5)\Delta x) \sin(\Delta\theta) \quad (5.6b)$$

$$\Delta\theta = \frac{2\pi}{\lambda} \Delta x = \frac{2\pi}{c} f \sqrt{\epsilon_{eff}} \Delta x \quad (5.6c)$$

The $ABCD$ matrix of the whole matching transformer in Figure 5-1(b) is found by multiplying the $ABCD$ parameters of all U segments as follows:

$$[A \ B; C \ D]_{Z(x)} = \prod_{i=1}^K [A \ B; C \ D]_i \quad (5.7)$$

The resulting overall $ABCD$ matrix of the matching transformer and the load impedance are utilized to calculate the input impedance, Z_{in} , which is given as:

$$Z_{in} = \frac{AZ_l + B}{CZ_l + D} \quad (5.8)$$

The input and the source impedances are used to express the input reflection coefficient, Γ_{in} , which is defined as:

$$\Gamma_{in} = \frac{Z_{in} - Z_s}{Z_{in} + Z_s} \quad (5.9)$$

Then, a *cost* function is minimized such that:

$$cost = \alpha |\Gamma_{in}|^2 \quad (5.10)$$

where α is a weighting factor used for faster convergence and the series coefficients (c_0, a_n, b_n) are the optimization variables. Width variations are constrained within

physically realizable ranges. In this context, width variations are chosen to be within $0.15 \text{ mm} \leq w(x) \leq 8 \text{ mm}$ to guarantee easy fabrication. Finally, the bound-constrained nonlinear cost function is minimized across the desired frequencies, function “fmincon.m” is used.

5.2 Results

To verify the proposed procedure, a single-frequency matching transformer operating at 1 GHz, a multi-frequency matching transformer operating at 0.9, 3.6, 5.4 GHz, and a wideband matching transformer operating over a band of 1–3 GHz are designed and simulated. All design examples are carried out using LCP flexible substrate with a thickness of 0.1 mm, relative permittivity of 2.9, and loss tangent of 0.0025. The length of the single-frequency transformer is set to 40 mm which is 42% less than the conventional CPW transformer. For the multi-frequency and wideband transformers, compactness is achieved setting their length as $\lambda/4$, where λ is the wavelength, at the lowest design frequency for the multi-frequency transformer and at the center frequency of the design band for the wideband one. The length of the multi-frequency and wideband transformers are 57 mm and 46 mm, respectively. The values of α are 1, 1/3, and 1/11 for the single-, multi-, and wideband transformers, respectively. All proposed transformers match a load impedance, $Z_l = 50 \Omega$, to a source impedance, $Z_s = 100 \Omega$.

Figure 5-2 illustrates the analytical and simulated scattering parameters for the single-frequency matching transformer at 1 GHz. Input port matching, S_{11} , equals to -28 dB at the design frequency. Furthermore, odd harmonics are suppressed in the proposed structure due to enforcing the *cost* function to fulfill matching conditions only at the design frequency. Transmission parameter, S_{21} , is better than -0.1 dB . The resulting analytical and simulated scattering parameters for the multi-frequency

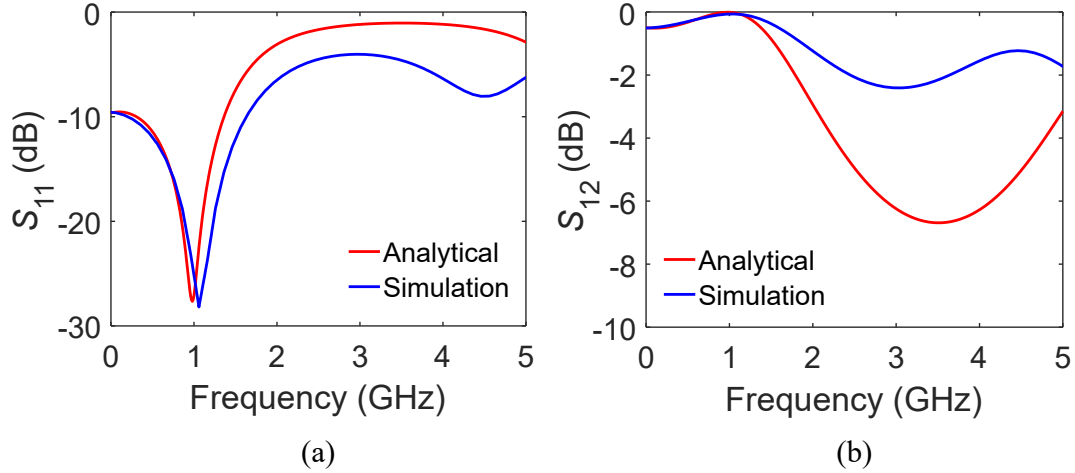


Figure 5-2: Analytical and simulated S -parameters for the single-frequency transformer operating at 1 GHz: (a) S_{11} (b) S_{21} .

matching transformer are depicted in Figure 5-3. S_{11} values at the three desired frequencies are below -23 dB; whereas S_{21} values are in the range of -0.2 dB. Figure 5-4 shows the analytical and simulation scattering parameters for the wideband matching transformer. Analytical results show a matching of -25 dB across the operating band (i.e., 1–3 GHz); simulated ones are below -15 dB. S_{21} values are better than -0.25 dB across the whole operating band.

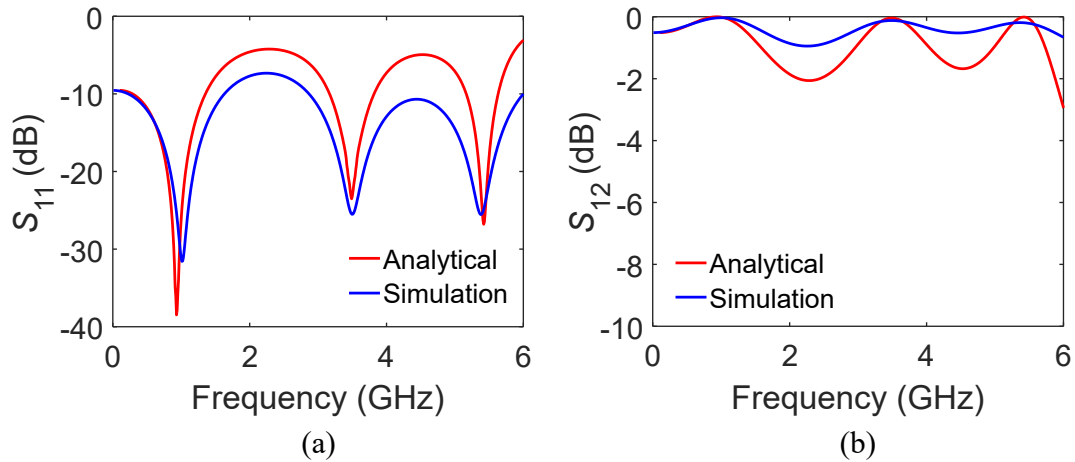


Figure 5-3: Analytical and simulated S -parameters for the multi-frequency transformer operating at 0.9, 3.6, 5.4 GHz: (a) S_{11} (b) S_{21} .

The simulated structures of the proposed transformers are given in Figure 5-5.

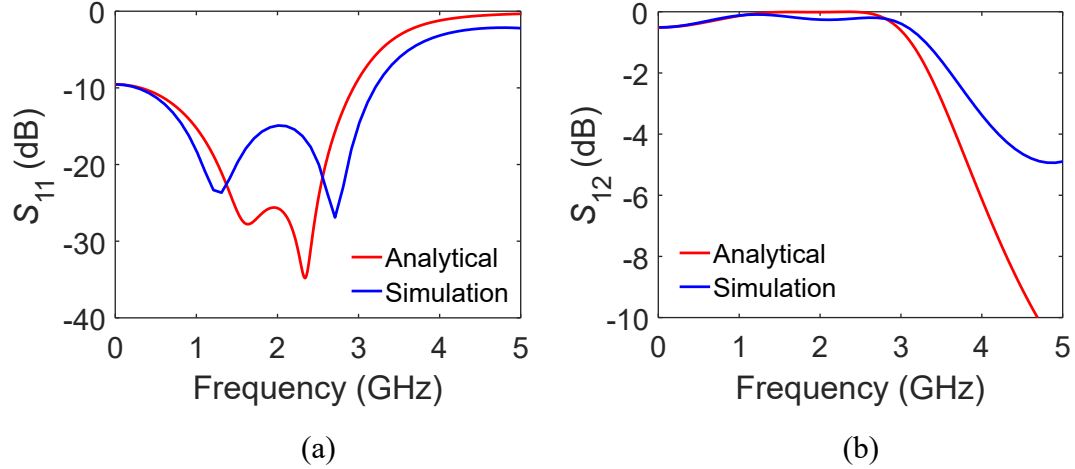


Figure 5-4: Analytical and simulated S -parameters for the wideband transformer operating over 1–3 GHz band: (a) S_{11} (b) S_{21} .

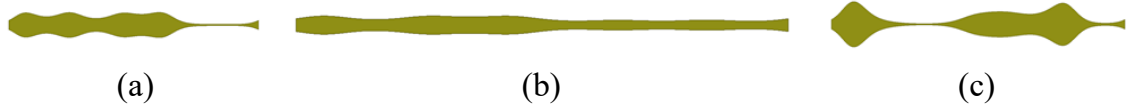


Figure 5-5: Signal trace of the proposed transformers: (a) single-frequency, (b) multi-frequency, and (c) wideband.

5.3 Conclusion

In this chapter, a new procedure for designing miniaturized matching transformers based on CPW-based structures is presented. The signal trace and the adjacent ground planes in the conventional CPW design are width-modulated with profiles governed by a truncated Fourier series expansion. For verification purposes, three matching transformers operating at different frequency bands were designed and simulated. The good agreement between both analytical and simulation results over the assigned frequency bands proves the validity of the design procedure. Simulations show that S_{11} values are below -23 dB for the single- and multi-frequency transformers, whereas they are below -15 dB for the wideband one. S_{21} values are better than -0.25 dB for all designed transformers.

Chapter 6

Conclusions and Future Work

6.1 Summary

The main goal of this dissertation was to introduce novel systematic approaches to design microwave and mm-wave front-end components with enhanced frequency response and bandwidth accessibility. Furthermore, the resulting structures were designed by avoiding any increase in the structural complexity, circuitry size, as well as manufacturing cost.

Chapter 2 started by presenting the mathematical derivations of designing SIW-based E-wall-varied transmission lines. The width between the metallic walls of via-holes was governed by a truncated Fourier series to achieve a predefined pass-band/stopband performance. The theory of rectangular waveguide was used to establish the optimization framework and obtain the series coefficients under predefined physical constraints. For better agreement between the calculated and simulated characteristic impedance, the constant k' is adopted.

Then, these E-wall-varied transmission lines were utilized to design SIW- and HMSIW-based BPFs with and without matching networks (i.e., SIW-to-microstrip transitions). The proposed design procedure resulted in compact, planar, and easy-to-fabricate structures. To validate the proposed methodology, two Ku-band BPF

prototypes with 2.5% and 5.8% 15-dB FBW were designed, simulated, and measured. Furthermore, the HMSIW concept was incorporated in one prototype to facilitate a miniaturized physical structure. Simulations and measurements were in close proximity with passband matching and transmission losses better than -15 dB and -2.5 dB, respectively. The proposed methodology allows for designing BPFs with predefined wideband or narrowband FBW by modifying the underlying physical constraints and optimization parameters. In addition, the proposed method can be utilized in realizing the optimum microstrip-to-SIW transition without performing a parametric study by providing the characteristic end-termination impedances of an SIW structure.

Chapter 3 illustrated another application of the E-wall-varied transmission lines, which was the filtering WPD. The basic idea of the proposed procedure depended on substituting the highpass uniform transmission lines in each arm of the conventional design by width-varying transmission lines of flexible bandwidth allocation and matching levels. Variations were governed by a truncated Fourier series with series coefficients optimized to achieve a predefined electrical performance. Moreover, the half-mode concept was employed to reduce the size of the PD by 50%. The even-mode analysis was utilized to optimize the Fourier series coefficients according to the desired performance; whereas the odd-mode analysis was carried out to obtain the optimum isolation resistors that achieve a proper isolation and output ports matching levels. The proposed design procedure resulted in a miniaturized, planar, single-layered, in-phase, and equal-split WPD. For verification purposes, a HMSIW-based PD with a center frequency of 12.2 GHz and 3.3% 15-dB fractional bandwidth was designed and simulated. Results showed that passband matching and transmission losses are better than -14 dB and -3.0 dB, respectively.

Chapter 4 presented the use of optimized microstrip NTLs to design in-phase, equal-split N -way WPD with bandwidth redefinition characteristics. Quarter-wave matching uniform transmission lines in the conventional design were replaced with

NTLs governed by a truncated Fourier series. A combining technique was used to reduce the N -way divider to its equivalent 2-way model. Then, even-mode analysis was adopted to obtain NTLs with predefined bandwidth functionalities; whereas several isolation resistors were optimized in the odd-mode analysis to achieve proper isolation and output ports matching over the frequency range of interest. Compactness was achieved by incorporating only one quarter-wave wideband NTL transformer, with a length computed at the center frequency, in each arm. For verification purposes, two 3-way WPDs with different frequency bands (i.e., 5–9 GHz and 4–10 GHz) and one 5–9 GHz 4-way divider examples were designed and simulated. In addition, the 3-way divider with 86% FBW was fabricated and measured. The good agreement between both simulation and measurement results over the assigned frequency band proved the validity of the design procedure. Results showed input and output ports matching and isolation below -15 dB, and transmission parameters in the range of $[-4.9, -6.2]$ dB and $[-6, -7.5]$ dB across the operating band of the 3-way and 4-way WPDs, respectively.

Chapter 5 presented a novel systematic approach to design compact CPW transformers to match predefined source and load impedances at single- and multi-frequency bands. The signal trace and the adjacent ground planes in the conventional CPW structure were width-modulated along the propagation path of the electromagnetic wave while maintaining a constant ground-trace separation. Validation was carried out by designing and simulating several matching transformers at different frequency bands. Specifically, single-, multi-, and wide-band transformers operating at 1 GHz, 0.9, 3.6, 5.4 GHz, and 1–3 GHz, respectively, were designed and simulated. The good agreement between both analytical and full-wave simulation results over the assigned frequency bands proved the validity of the design procedure. Simulations showed that S_{11} values were below -23 dB for single- and multi-frequency transformers, whereas they were below -15 dB for the wideband one. S_{21} values were better

than -0.25 dB for all designed transformers.

Chapter 6 concludes this dissertation and suggests future research paths that are aligned with the scope of this investigation. It also summarizes the scientific contribution of this study and lists the resulting publications.

6.2 Impact on Different Disciplines

Research outcomes demonstrated in this dissertation have a significant merit in adding values to the existing scientific, educational, and industrial fields. The presented studies complement other interdisciplinary areas of electrical engineering, and equally contribute in the development of futuristic technologies.

The highly-condensed radio frequency spectrum motivates and accelerates the research work toward mm-wave bands where more spectrum is available for various applications and higher data rates can be achieved. This research demonstrated the applicability of state-of-the-art technologies such as SIW and flexible substrates for developing mm-wave RF front-ends such as matching transformers, filters, and power dividers/combiners. Further, these manufacturing methodologies show promises performances by addressing the demanding requirements of future wireless systems such as high Q-factor, low cost, small size, and better power handling.

The Ku-band designs proposed in this research such as the SIW-based BPFs and filtering WPD/WPC tackle congestion of the scarce frequency spectrum by proposing front-ends that support emerging technologies aiming to exploit the higher frequency bands with ability to select/reject specific frequency bands. Such proposed structures satisfy the increasingly sophisticated microwave and mm-wave requirements of modern wireless systems. Specifically, such structures can be used for satellite communications, NASA's tracking and data relay satellite, SpaceX's Starlink satellites, and very-small-aperture terminal systems on ships.

In addition, the compact wideband N -way WPD and single- and multi-band matching transformers address enhancing access to the radio spectrum (EARS). Underlined investigations directly tackle congestion of the scarce frequency spectrum by proposing front-ends that support emerging technologies such as cellular RF front-ends and cognitive radios aiming to exploit the underutilized bandwidth. Compatible front-ends presented in this work enable multi-/wideband functionalities for spectrum scanning, determination of inactive frequency band(s), and transmitting/receiving at unexploited channels. Moreover, the multi-way WPD/WPC can be used in antenna arrays, multiple-input and multiple-output (MIMO), and PAs which are basic blocks in most of the modern wireless systems.

The presented research creates a platform for joint collaborations among different areas in electronics/communications engineering to explore solutions to the impending spectral insufficiency problem and facilitate novel approaches for mm-wave deployment for recent wireless applications. Moreover, the conceptual focus on this avenue furnishes guiding principles to undergraduate and graduate students seeking more knowledge on width-modulated transmission lines and their advantages over conventional lines.

The studies demonstrated in this work benefit both students and scholars by presenting a comprehensive analysis of widely used front-ends and their design using different manufacturing technologies. The components presented are communicated in almost any RF, microwave, and mm-wave engineering field. Besides, the proposed designs are illustrated through in-depth investigations of well-known design theories (e.g., transmission line theory). Clear mathematical guidelines are shown in this effort and are systematically-driven from theory to practice through engineering reasoning, professional simulations, and competent measurements. This research helps paving the way for new researchers in this field toward applying science, technology, engineering, and math (STEM) in their own research activities.

In addition, this research introduced compact, low cost, and easy to fabricate front-ends of various designs engineered to be compatible with the emerging solutions for better spectrum utilization. Thus, the developed techniques are also useful to the industrial market in the sense that they have the potential to enable better spectrum utilization, which facilitates higher data rates and allows more connected devices simultaneously.

6.3 Future Work

Research concepts presented in this dissertation can be further extended. The proposed methodologies, which led to proof-of-principle designs, have the potential of being redefined to contribute toward futuristic real-world applications.

In Chapter 2, a novel optimization-driven methodology to design compact BPFs with predefined bandwidth was proposed. The fixed-width transmission lines in the conventional structure were replaced by E-wall-varied transmission lines to achieve the predefined functionalities. Research on Fourier-varying via-hole walling BPFs can be extended in several ways. Examples include: *Wideband BPFs with high selectivity and wide stopband* – The width variations in the transmission line can be utilized in the design of wideband BPFs with improved out-of-band rejection levels. Higher-order modes of cavities and/or resonators can be used jointly with the proposed Fourier-varying via-hole walling transmission lines to further improve the electrical performance of BPFs by introducing transmission zeros to improve the selectivity of such filters. *SIW dual-band BPFs* – With the demanding requirements of modern wireless communication systems, having dual-band BPFs is a must. Such filters provide the functionality of two separate filters, but in the size of a single filter. *Fourier-varying via-hole walling slow-wave SIW dual-band BPFs* – Slow-wave SIW is a new concept for designing SIW-based structures and it allows decreasing the

longitudinal dimension by at least 40% [114]. Thus, further miniaturization can be achieved. In addition, complementary split ring resonators (CSRRs) can be used to achieve a dual-band response. *Tunable SIW BPFs* – Tunable BPFs play a vital role in recent wireless systems such as cognitive and software-defined radios. Such filters can be realized using a plasma material. Combining the E-wall varied SIW with a switchable post can lead to superior performance.

In Chapter 3, a highly-selective filtering WPD was proposed. The E-wall-varied transmission lines were adopted in the design of such dividers with predefined bandwidths. Research on SIW-based WPDs can be extended in many way. Examples include: *Fourier-varying slow-wave HMSIW WPDs* – As the half-mode concept was used to cut the structure in half in the transverse direction, the slow-wave concept can be used to cut it in the longitudinal dimension by at least 40%. Thus, we can achieve excellent electrical performance with at least 70% size reduction. *Multi-way Fourier-varying WPDs* – The E-wall-varied transmission lines can be used in the design of WPDs with narrowband/wideband matching and multiple output ports. In this scenario, optimized resistors between each two adjacent arms are required to maintain acceptable isolation and output ports matching conditions. *Unequal-split Fourier-varying WPDs* – Based on how the widths of the arms are varied, compact WPDs with unequal-split ratios can be designed. However, a different odd-mode analysis than the one presented in this work is required to optimize the values of the isolation resistors. Furthermore, matching transformers are required to match the resulting asymmetric output ports to 50Ω (i.e., impedance of the SMA connectors). *Fourier-varying HMSIW Couplers* – The design procedure used in Chapter 3 can be further extended to be applied on designing Fourier-varying via-hole walling couplers. Such configurations find use in many modern front-end circuits such as radar telemetry, power monitoring, and measurement setups. *Tunable HMSIW PDs* – As for the SIW BPFs, the proposed PD can be extended to be a tunable one using a plasma

material by controlling plasma parameters.

In Chapter 4, a detailed design procedure of multi-way WPDs was illustrated utilizing NTLs with a wideband matching nature. This concept can be extended and applied to several topologies. Examples include: *Wideband multi-way unequal-split WPDs* – As for the SIW-based WPDs, microstrip WPDs with unequal-split ratios can be designed. Nonetheless, the odd-mode analysis will be different than that presented in this dissertation. Extra NTLs with wideband characteristics are required to match the resulting asymmetric output ports to 50Ω . Moreover, optimized resistors between each two adjacent arms are required to maintain acceptable isolation and output ports matching conditions. *Half-width multi-way WPDs* – As the half-mode SIW structure is used to reduce the size of the original SIW structure by 50%, half-width microstrip line can be used here in a similar way to further decrease the size of such dividers [115].

In Chapter 5, a design procedure of single-, multi- and wide-band width-modulated CPW matching transformers were proposed. The designs were carried out on flexible substrates. The research on width-modulated CPW can be extended in many ways: Examples include: *CPW-based transformers for wearable devices* – These transformers can be implemented with bent surface structures with choosing the appropriate substrate to use in wearable devices applications. *CPW-based LPFs* – The CPW transmission lines can be used to build LPFs with improved passband/stopband characteristics. Such performance can be achieved by enforcing an error function over the intended frequency range. *CPW-based WPDs* – By replacing the uniform transmission lines of each arm in the conventional design, one can design compact wideband dividers.

6.4 Research Publications and Outcomes

1. **O. Hussein**, K. Al Shamaileh, N. Dib, A. Nosrati, S. Abushamleh, D. Georgiev, and V. Devabhaktuni, “Substrate integrated waveguide bandpass filtering with Fourier-varying via-hole walling,” *IEEE Access*, in press, August 2020.
2. **O. Hussein**, K. Al Shamaileh, S. Abushamleh, and V. Devabhaktuni, “A Fourier-varying substrate integrated waveguide filtering power divider with high isolation,” *IEEE Microwave and Wireless Components Letters* (manuscript draft is ready; waiting for measurement validation)
3. **O. Hussein**, K. Al Shamaileh, A. Sahu, B. Keneni, and V. Devabhaktuni, “Optimization of miniaturized single- and multi-band CPW-based matching transformers for RF circuitry on LCP substrates,” *IEEE 30th Canadian Conference on Electrical and Computer Engineering (CCECE)*, Windsor, ON, 2017, pp. 1–3.
4. **O. Hussein**, K. Al Shamaileh, and V. Devabhaktuni, “General design of impedance-varying multi-way Wilkinson power divider with bandwidth redefinition characteristics,” *International Journal of RF and Microwave Computer-Aided Engineering*, vol. 27, no. 5, pp. 1–9, Jan. 2017.
5. **O. Hussein**, K. Al Shamaileh, V. Devabhaktuni, and P. Aaen, “Wideband impedance-varying n -way Wilkinson power divider/combiner for RF power amplifiers,” 88th *ARFTG Microwave Measurement Conference (ARFTG)*, Austin, TX, 2016, pp. 1–4.

References

- [1] Annual Survey — Highlights. CITA, 2019. [Online]. Available: <https://api.ctia.org/wp-content/uploads/2019/06/2019-Annual-Survey-Highlights-FINAL.pdf>
- [2] “RF front end modules and components for cellphones,” Yole Development, Tech. Rep., March 2017.
- [3] X. Chen and K. Wu, “Substrate integrated waveguide filter: Basic design rules and fundamental structure features,” *IEEE Microwave Magazine*, vol. 15, no. 5, pp. 108–116, 2014.
- [4] R. Simons, E. Wintucky, J. Freeman, and C. Chevalier, “High-efficiency Ka-band MMIC SSPA power compiner for NASA’s space communication,” *International Journal of High Speed Electronics and Systems*, vol. 20, no. 03, pp. 405–415, 2011.
- [5] K. Wu, “Integration and interconnect techniques of planar and non-planar structures for microwave and millimeter-wave circuits - current status and future trend,” in *Asia-Pacific Microwave Conference*, vol. 2, 2001, pp. 411–416.
- [6] A. Sahu, P. Aaen, and V. Devabhaktuni, “Advanced technologies for next-generation rf front-end modules,” *International Journal of RF and Microwave Computer-Aided Engineering*, vol. 29, no. 6, pp. 1–17, 2019.
- [7] F. Wang and T. Arslan, “Inkjet-printed antenna on flexible substrate for wearable microwave imaging applications,” in *Loughborough Antennas & Propagation Conference (LAPC)*, 2016, pp. 1–4.

- [8] Z. Peng, J. Muñoz-Ferreras, R. Gómez-García, L. Ran, and C. Li, “24-ghz biomedical radar on flexible substrate for isar imaging,” in *IEEE MTT-S International Wireless Symposium (IWS)*, 2016, pp. 1–4.
- [9] A. Sahu, V. Devabhaktuni, A. Lewandowski, P. Barnuta, T. M. Wallis, M. Shkunov, and P. H. Aaen, “Microwave characterization of ink-jet printed cpw on pet substrates,” in *86th ARFTG Microwave Measurement Conference*, 2015, pp. 1–4.
- [10] A. Furniturewalla, M. Chan, J. Sui, K. Ahuja, and M. Javanmard, “Fully integrated wearable impedance cytometry platform on flexible circuit board with online smartphone readout,” *Microsystems & Nanoengineering*, vol. 4, no. 20, 2018.
- [11] D. Thompson, O. Tantot, H. Jallageas, G. Ponchak, M. Tentzeris, and J. Papapolymerou, “Characterization of liquid crystal polymer (lcp) material and transmission lines on lcp substrates from 30 to 110 ghz,” *IEEE Transactions on Microwave Theory and Techniques*, vol. 52, no. 4, pp. 1343–1352, 2004.
- [12] D. Choudhary and R. Chaudhary, “A compact SIW based filtering power divider with improved selectivity using CSRR,” in *Progress in Electromagnetics Research Symposium - Fall (PIERS)*, 2017, pp. 1334–1337.
- [13] X. Chen, K. Wu, and D. Drolet, “Substrate integrated waveguide filter with improved stopband performance for satellite ground terminal,” *IEEE Transactions on Microwave Theory and Techniques*, vol. 57, no. 3, pp. 674–683, 2009.
- [14] B. Zhang, R. Li, L. Wu, H. Sun, and Y. Guo, “A highly integrated 3-D printed metallic K-band passive front end as the unit cell in a large array for satellite communication,” *IEEE Antennas and Wireless Propagation Letters*, vol. 17, no. 11, pp. 2046–2050, 2018.

- [15] X. Wang, X. Zhu, L. Tian, P. Liu, W. Hong, and A. Zhu, "Design and experiment of filtering power divider based on shielded HMSIW/QMSIW technology for 5G wireless applications," *IEEE Access*, vol. 7, pp. 72 411–72 419, 2019.
- [16] E. Al Abbas, A. Abbosh, and K. Bialkowski, "Tunable in-phase power divider for 5G cellular networks," *IEEE Microwave and Wireless Components Letters*, vol. 27, no. 6, pp. 551–553, 2017.
- [17] F. Oktafiani, Y. Wahyu, and Y. P. Saputera, "Fabrication of integrated power divider and filter for X band radar applications," in *International Conference on Electrical Engineering and Computer Science (ICECOS)*, 2018, pp. 33–38.
- [18] S. Wong, R. S. Chen, K. Wang, Z. Chen, and Q. Chu, "U-shape slots structure on substrate integrated waveguide for 40-GHz bandpass filter using LTCC technology," *IEEE Transactions on Components, Packaging and Manufacturing Technology*, vol. 5, no. 1, pp. 128–134, 2015.
- [19] X. Chen and K. Wu, "Self-packaged millimeter-wave substrate integrated waveguide filter with asymmetric frequency response," *IEEE Transactions on Components, Packaging and Manufacturing Technology*, vol. 2, no. 5, pp. 775–782, 2012.
- [20] K. Wang, S. Wong, G. Sun, Z. Chen, L. Zhu, and Q. Chu, "Synthesis method for substrate-integrated waveguide bandpass filter with even-order Chebyshev response," *IEEE Transactions on Components, Packaging and Manufacturing Technology*, vol. 6, no. 1, pp. 126–135, 2016.
- [21] S. Wong, K. Wang, Z. Chen, and Q. Chu, "Electric coupling structure of substrate integrated waveguide (SIW) for the application of 140-GHz bandpass filter on LTCC," *IEEE Transactions on Components, Packaging and Manufacturing Technology*, vol. 4, no. 2, pp. 316–322, 2014.

- [22] X. Chen, W. Hong, T. Cui, J. Chen, and K. Wu, "Substrate integrated waveguide (SIW) linear phase filter," *IEEE Microwave and Wireless Components Letters*, vol. 15, no. 11, pp. 787–789, 2005.
- [23] K. Chin, C. Chang, C. Chen, Z. Guo, D. Wang, and W. Che, "LTCC multilayered substrate-integrated waveguide filter with enhanced frequency selectivity for system-in-package applications," *IEEE Transactions on Components, Packaging and Manufacturing Technology*, vol. 4, no. 4, pp. 664–672, 2014.
- [24] A. Azad and A. Mohan, "Substrate integrated waveguide dual-band and wide-stopband bandpass filters," *IEEE Microwave and Wireless Components Letters*, vol. 28, no. 8, pp. 660–662, 2018.
- [25] K. Zhou, C. Zhou, and W. Wu, "Substrate integrated waveguide dual-band filter with wide-stopband performance," *Electronics Letters*, vol. 53, no. 16, pp. 1121–1123, 2017.
- [26] R. Li, X. Tang, and F. Xiao, "Design of substrate integrated waveguide transversal filter with high selectivity," *IEEE Microwave and Wireless Components Letters*, vol. 20, no. 6, pp. 328–330, 2010.
- [27] A. Khan and M. Mandal, "Narrowband substrate integrated waveguide bandpass filter with high selectivity," *IEEE Microwave and Wireless Components Letters*, vol. 28, no. 5, pp. 416–418, 2018.
- [28] W. Shen, W. Yin, X. Sun, and L. Wu, "Substrate-integrated waveguide bandpass filters with planar resonators for system-on-package," *IEEE Transactions on Components, Packaging and Manufacturing Technology*, vol. 3, no. 2, pp. 253–261, 2013.
- [29] D. Guan, P. You, Q. Zhang, K. Xiao, and S. Yong, "Hybrid spoof surface plasmon polariton and substrate integrated waveguide transmission line and its

- application in filter,” *IEEE Transactions on Microwave Theory and Techniques*, vol. 65, no. 12, pp. 4925–4932, 2017.
- [30] L. Szydłowski, A. Jedrzejewski, and M. Mrozowski, “A trisection filter design with negative slope of frequency-dependent crosscoupling implemented in substrate integrated waveguide (SIW),” *IEEE Microwave and Wireless Components Letters*, vol. 23, no. 9, pp. 456–458, 2013.
- [31] M. Le Coq, E. Rius, J. Favennec, C. Quendo, B. Potelon, L. Estagerie, P. Moroni, B. Bonnet, and A. El Mostrah, “Miniaturized C-band SIW filters using high-permittivity ceramic substrates,” *IEEE Transactions on Components, Packaging and Manufacturing Technology*, vol. 5, no. 5, pp. 620–626, 2015.
- [32] X. Li, K. Dhvaj, and T. Itoh, “Single-layer slow-wave substrate integrated waveguide with enhanced capacitance,” in *2018 IEEE/MTT-S International Microwave Symposium - IMS*, June 2018, pp. 316–318.
- [33] M. Bertrand, Z. Liu, E. Pistono, D. Kaddour, and P. Ferrari, “A compact slow-wave substrate integrated waveguide cavity filter,” in *IEEE MTT-S International Microwave Symposium*, 2015, pp. 1–3.
- [34] A. Sahu, O. Hussein, B. Keneni, K. Alshamaileh, and V. Devabhaktuni, “A slow-wave substrate integrated waveguide dual-band filter,” in *IEEE 30th Canadian Conference on Electrical and Computer Engineering (CCECE)*, 2017, pp. 1–3.
- [35] J. de Dios Ruiz, F. Martinez-Viviente, A. Alvarez-Melcon, and J. Hinojosa, “Substrate integrated waveguide (SIW) with koch fractal electromagnetic bandgap structures (KFEBG) for bandpass filter design,” *IEEE Microwave and Wireless Components Letters*, vol. 25, no. 3, pp. 160–162, 2015.

- [36] W. Shen, "Extended-doublet half-mode substrate integrated waveguide band-pass filter with wide stopband," *IEEE Microwave and Wireless Components Letters*, vol. 28, no. 4, pp. 305–307, 2018.
- [37] P. Li, H. Chu, and R. Chen, "Design of compact bandpass filters using quarter-mode and eighth-mode SIW cavities," *IEEE Transactions on Components, Packaging and Manufacturing Technology*, vol. 7, no. 6, pp. 956–963, 2017.
- [38] X. Wang, X. Zhu, Z. H. Jiang, Z. Hao, Y. Wu, and W. Hong, "Analysis of eighth-mode substrate-integrated waveguide cavity and flexible filter design," *IEEE Transactions on Microwave Theory and Techniques*, vol. 67, no. 7, pp. 2701–2712, 2019.
- [39] Z.-Y. Zhang and K. Wu, "Broadband half-mode substrate integrated waveguide (HMSIW) Wilkinson power divider," in *2008 IEEE MTT-S International Microwave Symposium Digest*, 2008, pp. 879–882.
- [40] T. Djerafi, D. Hammou, K. Wu, and S. O. Tatu, "Ring-shaped substrate integrated waveguide Wilkinson power dividers/combiners," *IEEE Transactions on Components, Packaging and Manufacturing Technology*, vol. 4, no. 9, pp. 1461–1469, 2014.
- [41] A. Moulay and T. Djerafi, "Wilkinson power divider with fixed width substrate-integrated waveguide line and a distributed isolation resistance," *IEEE Microwave and Wireless Components Letters*, vol. 28, no. 2, pp. 114–116, 2018.
- [42] K. Sarhadi and M. Shahabadi, "Wideband substrate integrated waveguide power splitter with high isolation," *IET Microwaves, Antennas Propagation*, vol. 4, no. 7, pp. 817–821, 2010.
- [43] J. Hui, W. Feng, and W. Che, "Balun bandpass filter based on multilayer sub-

- strate integrated waveguide power divider,” *Electronics Letters*, vol. 48, no. 10, pp. 571–573, 2012.
- [44] X. Shen, W. Feng, H. Chen, and W. Che, “Narrowband filtering balun power divider based on SIW and CSRRs,” in *2018 International Conference on Microwave and Millimeter Wave Technology (ICMMT)*, 2018, pp. 1–3.
- [45] K. Song, Y. Zhu, and F. Zhang, “Single- and dual-band filtering-response power dividers embedded SIW filter with improved output isolation,” *Scientific Reports*, vol. 7, no. 3361, 2017.
- [46] A. Moznebi and K. Afrooz, “Substrate integrated waveguide (SIW) filtering power divider/combiner with high selectivity,” *Wireless Personal Communications*, vol. 97, pp. 1117–1127, 2017.
- [47] U. Rosenberg, M. Salehi, J. Bornemann, and E. Mehrshahi, “A novel frequency-selective power combiner/divider in single-layer substrate integrated waveguide technology,” *IEEE Microwave and Wireless Components Letters*, vol. 23, no. 8, pp. 406–408, 2013.
- [48] H. Chu, J. Chen, and Y. Guo, “Substrate integrated waveguide differential filtering power divider with good common-mode suppression and high selectivity,” *Electronics Letters*, vol. 51, no. 25, pp. 2115–2117, 2015.
- [49] M. Pasian, L. Silvestri, C. Rave, M. Bozzi, L. Perregri, A. F. Jacob, and K. K. Samanta, “Substrate-integrated-waveguide E-plane 3-dB power-divider/combiner based on resistive layers,” *IEEE Transactions on Microwave Theory and Techniques*, vol. 65, no. 5, pp. 1498–1510, 2017.
- [50] Y. Huang, W. Jiang, H. Jin, Y. Zhou, S. Leng, G. Wang, and K. Wu, “Substrate-integrated waveguide power combiner/divider incorporating absorbing mate-

- rial,” *IEEE Microwave and Wireless Components Letters*, vol. 27, no. 10, pp. 885–887, 2017.
- [51] A. Khan and M. Mandal, “Miniaturized substrate integrated waveguide (SIW) power dividers,” *IEEE Microwave and Wireless Components Letters*, vol. 26, no. 11, pp. 888–890, 2016.
- [52] A. Moznebi, K. Afrooz, M. Danaeian, and P. Mousavi, “Four-way filtering power divider using SIW and eighth-mode SIW cavities with ultrawide out-of-band rejection,” *IEEE Microwave and Wireless Components Letters*, vol. 29, no. 9, pp. 586–588, 2019.
- [53] U. Gysel, “A new N -way power divider/combiner suitable for high-power applications,” in *IEEE-MTT-S International Microwave Symposium*, 1975, pp. 116–118.
- [54] F. Lin, Q. Chu, Z. Gong, and Z. Lin, “Compact broadband Gysel power divider with arbitrary power-dividing ratio using microstrip/slotline phase inverter,” *IEEE Transactions on Microwave Theory and Techniques*, vol. 60, no. 5, pp. 1226–1234, 2012.
- [55] H. Chen, X. Wang, W. Che, Y. Zhou, and Q. Xue, “Development of compact HMSIW Gysel power dividers with microstrip isolation networks,” *IEEE Access*, vol. 6, pp. 60 429–60 437, 2018.
- [56] H. Chen, W. Che, X. Wang, and W. Feng, “Size-reduced planar and nonplanar SIW Gysel power divider based on low temperature co-fired ceramic technology,” *IEEE Microwave and Wireless Components Letters*, vol. 27, no. 12, pp. 1065–1067, 2017.
- [57] A. Wentzel, V. Subramanian, A. Sayed, and G. Boeck, “Novel broadband

- Wilkinson power combiner,” in *European Microwave Conference*, 2006, pp. 212–215.
- [58] L. Chiu, T. Y. Yum, Q. Xue, and C. H. Chan, “A wideband compact parallel-strip 180° Wilkinson power divider for push-pull circuitries,” *IEEE Microwave and Wireless Components Letters*, vol. 16, no. 1, pp. 49–51, 2006.
- [59] N. Dib and M. Khodier, “Design and optimization of multi-band Wilkinson power divider,” *International Journal of RF and Microwave Computer-Aided Engineering*, vol. 18, no. 1, pp. 14–20, 2008.
- [60] H. Oraizi and A.-R. Sharifi, “Design and optimization of broadband asymmetrical multisection Wilkinson power divider,” *IEEE Transactions on Microwave Theory and Techniques*, vol. 54, no. 5, pp. 2220–2231, 2006.
- [61] Y.-S. Lin and J.-H. Lee, “Miniature ultra-wideband power divider using bridged T-coils,” *IEEE Microwave and Wireless Components Letters*, vol. 22, no. 8, pp. 391–393, 2012.
- [62] J.-C. Chiu, J.-M. Lin, and Y.-H. Wang, “A novel planar three-way power divider,” *IEEE Microwave and Wireless Components Letters*, vol. 16, no. 8, pp. 449–451, 2006.
- [63] D. Hawatmeh, N. Dib, and K. Al Shamaileh, “Design and analysis of a 3-way unequal split ultra-wideband Wilkinson power divider,” in *Proceedings of the 2012 IEEE International Symposium on Antennas and Propagation*, 2012, pp. 1–2.
- [64] J. Zhou and K. Morris, “Effects of interconnecting transmission lines on four-way Wilkinson power divider,” *Microwave and Optical Technology Letters*, vol. 51, no. 12, pp. 2850–2852, 2009.

- [65] J. Zhou, K. Morris, and M. Lancaster, “General design of multiway multisection power dividers by interconnecting two-way dividers,” *IEEE Transactions on Microwave Theory and Techniques*, vol. 55, no. 10, pp. 2208–2215, 2007.
- [66] Y. Xu and R. Bosisio, “Design of multiway power divider by using stepped-impedance transformers,” *IEEE Transactions on Microwave Theory and Techniques*, vol. 60, no. 9, pp. 2781–2790, 2012.
- [67] A. Abbosh, “A compact UWB three-way power divider,” *IEEE Microwave and Wireless Components Letters*, vol. 17, no. 8, pp. 598–600, 2007.
- [68] J. Chen and Q. Xue, “Novel 5:1 unequal Wilkinson power divider using offset double-sided parallel-strip lines,” *IEEE Microwave and Wireless Components Letters*, vol. 17, no. 3, pp. 175–177, 2007.
- [69] M. Rabbani and H. Ghafouri-Shiraz, “Liquid crystalline polymer substrate-based THz microstrip antenna arrays for medical applications,” *IEEE Antennas and Wireless Propagation Letters*, vol. 16, pp. 1533–1536, 2017.
- [70] Y. Zhang, F. Wang, S. Shi, R. Martin, P. Yao, and D. Prather, “Ultra-wideband microstrip line-to-microstrip line transition in multilayer LCP substrate at millimeter-wave frequencies,” *IEEE Microwave and Wireless Components Letters*, vol. 27, no. 10, pp. 873–875, 2017.
- [71] Y. Yu, P. Jin, K. Ding, and M. Zhang, “A flexible UWB CPW-fed antenna on liquid crystal polymer substrate,” in *Asia-Pacific Microwave Conference (APMC)*, vol. 2, 2015, pp. 1–3.
- [72] B. Kim, S. Nikolaou, G. Ponchak, Y.-S. Kim, J. Papapolymerou, and M. Tentzeris, “A curvature CPW-fed ultra-wideband monopole antenna on liquid crystal polymer substrate using flexible characteristic,” in *IEEE Antennas and Propagation Society International Symposium*, 2006, pp. 1667–1670.

- [73] D. Senior, A. Rahimi, P. Jao, and Y. Yoon, “Flexible liquid crystal polymer based complementary split ring resonator loaded quarter mode substrate integrated waveguide filters for compact and wearable broadband rf applications,” in *2014 IEEE 64th Electronic Components and Technology Conference (ECTC)*, 2014, pp. 789–795.
- [74] Y. Zhang, S. Shi, R. Martin, and D. Prather, “Broadband SIW-to-waveguide transition in multilayer LCP substrates at W-band,” *IEEE Microwave and Wireless Components Letters*, vol. 27, no. 3, pp. 224–226, 2017.
- [75] L. Pazin and Y. Leviatan, “A compact 60-GHz tapered slot antenna printed on LCP substrate for WPAN applications,” *IEEE Antennas and Wireless Propagation Letters*, vol. 9, pp. 272–275, 2010.
- [76] S. Nikolaou, G. Ponchak, J. Papapolymerou, and M. Tentzeris, “Conformal double exponentially tapered slot antenna (DE TSA) on LCP for UWB applications,” *IEEE Transactions on Antennas and Propagation*, vol. 54, no. 6, pp. 1663–1669, 2006.
- [77] N. Kingsley, G. Ponchak, and J. Papapolymerou, “Reconfigurable RF MEMS phased array antenna integrated within a liquid crystal polymer (LCP) system-on-package,” *IEEE Transactions on Antennas and Propagation*, vol. 56, no. 1, pp. 108–118, 2008.
- [78] S. Qian, Z. Hao, J. Hong, J. Parry, and D. Hand, “Design and fabrication of a miniature highpass filter using multilayer LCP technology,” in *41st European Microwave Conference*, 2011, pp. 187–190.
- [79] L. Hepburn and J. Hong, “Compact integrated lumped element LCP filter,” *IEEE Microwave and Wireless Components Letters*, vol. 26, no. 1, pp. 19–21, 2016.

- [80] L. Han and X. Gao, "Modeling of bending characteristics on micromachined RF MEMS switch based on LCP substrate," *IEEE Transactions on Electron Devices*, vol. 63, no. 9, pp. 3707–3712, 2016.
- [81] M. Chen, A.-V. Pham, N. Evers, C. Kapusta, J. Iannotti, W. Kornrumpf, J. Maciel, and N. Karabudak, "Design and development of a package using LCP for RF/microwave MEMS switches," *IEEE Transactions on Microwave Theory and Techniques*, vol. 54, no. 11, pp. 4009–4015, 2006.
- [82] E. Juntunen, W. Khan, C. Patterson, S. Bhattacharya, D. Dawn, J. Laskar, and J. Papapolymerou, "An LCP packaged high-power, high-efficiency CMOS millimeter-wave oscillator," in *IEEE MTT-S International Microwave Symposium*, 2011, pp. 1–4.
- [83] E. Juntunen, D. Dawn, J. Laskar, and J. Papapolymerou, "High-power, high-efficiency CMOS millimetre-wave oscillators," *IET Microwaves, Antennas Propagation*, vol. 6, no. 10, pp. 1158–1163, 2012.
- [84] Y. Cassivi, L. Perregrini, P. Arcioni, M. Bressan, K. Wu, and G. Conciauro, "Dispersion characteristics of substrate integrated rectangular waveguide," *IEEE Microwave and Wireless Components Letters*, vol. 12, no. 9, pp. 333–335, 2002.
- [85] A. Sahu, V. Devabhaktuni, R. Mishra, and P. Aaen, "Recent advances in theory and applications of substrate-integrated waveguides: A review," *International Journal of RF and Microwave Computer-Aided Engineering*, vol. 26, no. 2, pp. 129–145, 2015.
- [86] M. Bozzi, A. Georgiadis, and K. Wu, "Review of substrate-integrated waveguide circuits and antennas," *IET Microwaves, Antennas Propagation*, vol. 5, no. 8, pp. 909–920, 2011.

- [87] F. Xu and K. Wu, "Guided-wave and leakage characteristics of substrate integrated waveguide," *IEEE Transactions on Microwave Theory and Techniques*, vol. 53, no. 1, pp. 66–73, 2005.
- [88] M. Salehi and E. Mehrshahi, "A closed-form formula for dispersion characteristics of fundamental SIW mode," *IEEE Microwave and Wireless Components Letters*, vol. 21, no. 1, pp. 4–6, 2011.
- [89] Z. Kordiboroujeni and J. Bornemann, "Designing the width of substrate integrated waveguide structures," *IEEE Microwave and Wireless Components Letters*, vol. 23, no. 10, pp. 518–520, 2013.
- [90] D. Deslandes and K. Wu, "Accurate modeling, wave mechanisms, and design considerations of a substrate integrated waveguide," *IEEE Transactions on Microwave Theory and Techniques*, vol. 54, no. 6, pp. 2516–2526, 2006.
- [91] M. Bozzi, L. Perregrini, and K. Wu, "Modeling of conductor, dielectric, and radiation losses in substrate integrated waveguide by the boundary integral-resonant mode expansion method," *IEEE Transactions on Microwave Theory and Techniques*, vol. 56, no. 12, pp. 3153–3161, 2008.
- [92] M. Bozzi, M. Pasian, L. Perregrini, and Ke Wu, "On the losses in substrate integrated waveguides," in *European Microwave Conference*, 2007, pp. 384–387.
- [93] M. Pasian, M. Bozzi, and L. Perregrini, "Crosstalk in substrate integrated waveguides," *IEEE Transactions on Electromagnetic Compatibility*, vol. 57, no. 1, pp. 80–86, 2015.
- [94] K. Alshamaileh, V. Devabhaktuni, and N. Dib, "Impedance-varying broadband 90° branch-line coupler with arbitrary coupling levels and higher order harmonic suppression," *IEEE Transactions on Components, Packaging and Manufacturing Technology*, vol. 5, no. 10, pp. 1507–1515, 2015.

- [95] D. M. Pozar, *Microwave engineering*. New York, NY, USA: Wiley, 2012.
- [96] P. A. Rizzi, *Microwave engineering: passive circuits*. Englewood Cliffs, NJ: Prentice Hall, 1988.
- [97] F. Ishihara and S. Iiguchi, “Equivalent characteristic impedance formula of waveguide and its applications,” *Electronics and Communications in Japan (Part II: Electronics)*, vol. 75, no. 5, pp. 54–66, 1992.
- [98] ANSYS-High Frequency Structure Simulator (HFSS), Ansys Inc., PA, USA, 2016.
- [99] H. Ghorbaninejad and R. Heydarian, “New design of waveguide directional coupler using genetic algorithm,” *IEEE Microwave and Wireless Components Letters*, vol. 26, no. 2, pp. 86–88, 2016.
- [100] P. Kumar, A. Kedar, and A. Singh, “Design and development of low-cost low sidelobe level slotted waveguide antenna array in X-band,” *IEEE Transactions on Antennas and Propagation*, vol. 63, no. 11, pp. 4723–4731, 2015.
- [101] H. Cheng, I. Chung, and W. Chen, “Thermal chip placement in MCMs using a novel hybrid optimization algorithm,” *IEEE Transactions on Components, Packaging and Manufacturing Technology*, vol. 2, no. 5, pp. 764–774, 2012.
- [102] J. Kim, T. Yoon, J. Kim, and J. Choi, “Design of an ultra wide-band printed monopole antenna using FDTD and genetic algorithm,” *IEEE Microwave and Wireless Components Letters*, vol. 15, no. 6, pp. 395–397, 2005.
- [103] R. W. Klopfenstein, “A transmission line taper of improved design,” *Proceedings of the IRE*, vol. 44, no. 1, pp. 31–35, 1956.

- [104] K. Al Shamaileh, N. Dib, and A. Abbosh, "Analysis and design of ultra-wideband unequal-split Wilkinson power divider using tapered lines transformers," *Electromagnetics*, vol. 32, no. 7, pp. 426–437, 2012.
- [105] C. Chiang and B.-K. Chung, "Ultra wideband power divider using tapered line," *Progress In Electromagnetics Research*, vol. 106, pp. 61–73, 2010.
- [106] W. Hong, B. Liu, Y. Wang, Q. Lai, H. Tang, X. Yin, Y. Dong, Y. Zhang, and K. Wu, "Half mode substrate integrated waveguide: A new guided wave structure for microwave and millimeter wave application," in *Joint 31st International Conference on Infrared Millimeter Waves and 14th International Conference on Terahertz Electronics*, 2006, pp. 219–219.
- [107] Q. Lai, C. Fumeaux, W. Hong, and R. Vahldieck, "Characterization of the propagation properties of the half-mode substrate integrated waveguide," *IEEE Transactions on Microwave Theory and Techniques*, vol. 57, no. 8, pp. 1996–2004, 2009.
- [108] B. Liu, W. Hong, Y. Wang, Q. Lai, and K. Wu, "Half mode substrate integrated waveguide (HMSIW) 3-dB coupler," *IEEE Microwave and Wireless Components Letters*, vol. 17, no. 1, pp. 22–24, 2007.
- [109] A. Qaroot and N. Dib, "General design of N -way multi-frequency unequal split planar Wilkinson power divider," *Progress In Electromagnetics Research*, vol. 14, pp. 115–129, 2010.
- [110] K. Al Shamaileh, M. Almalkawi, V. Devabhaktuni, N. Dib, B. Henin, and A. Abbosh, "Fourier-based transmission line ultra-wideband Wilkinson power divider for EARS applications," in *IEEE 56th International Midwest Symposium on Circuits and Systems (MWSCAS)*, 2013, pp. 872–875.

- [111] W. Xiao, T. Mei, Y. Lan, Y. Wu, R. Xu, and Y. Xu, "Triple band-notched UWB monopole antenna on ultra-thin liquid crystal polymer based on ESCSRR," *Electronics Letters*, vol. 53, no. 2, pp. 57–58, 2017.
- [112] R. Simons, *Coplanar waveguide circuits, components, and systems*. New York, NY, USA: J. Wiley & Sons, 2001.
- [113] W. Hilberg, "From approximations to exact relations for characteristic impedances," *IEEE Transactions on Microwave Theory and Techniques*, vol. 17, no. 5, pp. 259–265, 1969.
- [114] A. Niembro-Martín, V. Nasserddine, E. Pistono, H. Issa, A. Franc, T. Vuong, and P. Ferrari, "Slow-wave substrate integrated waveguide," *IEEE Transactions on Microwave Theory and Techniques*, vol. 62, no. 8, pp. 1625–1633, 2014.
- [115] N. Nguyen-Trong and C. Fumeaux, "Half-mode substrate-integrated waveguides and their applications for antenna technology: A review of the possibilities for antenna design," *IEEE Antennas and Propagation Magazine*, vol. 60, no. 6, pp. 20–31, 2018.
- [116] R. Collin, *Field Theory of Guided Waves*. Piscataway, NJ, USA: IEEE Press, 1991.
- [117] M. Pasian, M. Bozzi, and L. Perregrini, "A formula for radiation loss in substrate integrated waveguide," *IEEE Transactions on Microwave Theory and Techniques*, vol. 62, no. 10, pp. 2205–2213, 2014.
- [118] F. Grine, T. Djerafi, M. T. Benhabiles, K. Wu, and M. L. Riabi, "High-q substrate integrated waveguide resonator filter with dielectric loading," *IEEE Access*, vol. 5, pp. 12 526–12 532, 2017.

Appendix A

Losses in Microstrip, CPW, and SIW lines

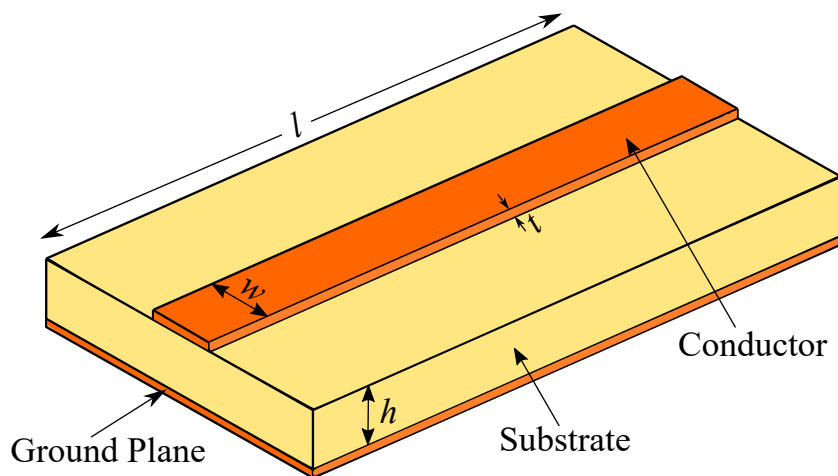


Figure A-1: A schematic diagram of a microstrip line.

In this appendix, different types of losses and their formulas for the microstrip, CPW, and SIW lines are discussed. A schematic of a microstrip line is shown in Figure A-1, which consists of a strip conductor of width, w , and thickness, t , fabricated on a grounded dielectric substrate with a relative permittivity, ϵ_r , and a thickness, h . The total losses of the microstrip line is attributed mainly to the dielectric loss and conductor loss in the substrate and the strip conductor, respectively. The dielectric loss (in Np/m) of a microstrip line supporting a quasi-TEM mode can be expressed

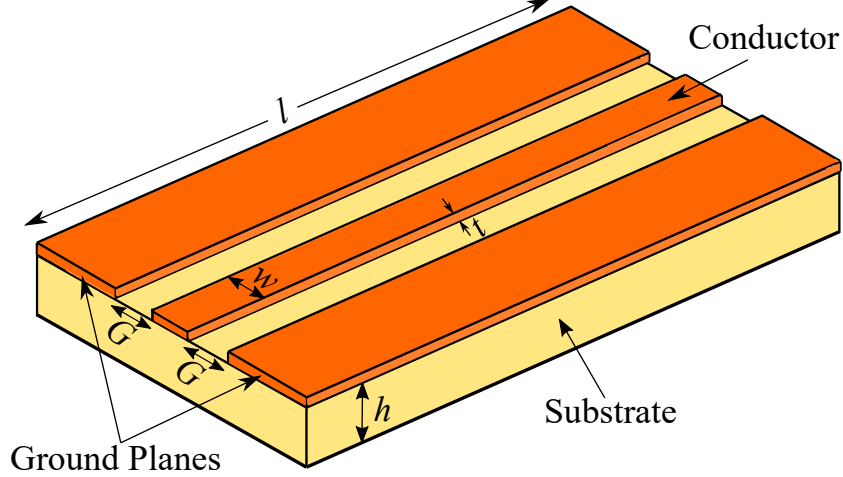


Figure A-2: A schematic diagram of a CPW.

as [95]:

$$\alpha_d = \frac{k_0 \epsilon_r (\epsilon_{eff} - 1) \tan \delta}{2 \sqrt{\epsilon_{eff}} (\epsilon_r - 1)} \quad (\text{A.1})$$

where $\tan \delta$ is the loss tangent of the dielectric substrate, k_0 is the wave number in free space and it is given by $k_0 = \omega \sqrt{\mu_0 \epsilon_0}$, and ϵ_{eff} is given in (4.3). On the other hand, the conductor loss (in Np/m) is given approximately by [95]:

$$\alpha_c = \frac{R_s}{Z_0 w} \quad (\text{A.2})$$

where $R_s = \sqrt{\omega \mu_0 / 2 \sigma}$ is the surface resistivity of the conductor and Z_0 is microstrip characteristic impedance given by

$$Z_0 = \begin{cases} \frac{60}{\sqrt{\epsilon_{eff}}} \ln \left(\frac{8d}{w} + \frac{w}{4d} \right) & \text{for } w/d \leq 1 \\ \frac{120\pi}{\sqrt{\epsilon_{eff}} [w/d + 1.393 + 0.667 \ln(w/d + 1.444)]} & \text{for } w/d \geq 1 \end{cases} \quad (\text{A.3})$$

Thus, total losses in a microstrip line is given by $\alpha_t = \alpha_d + \alpha_c$.

Figure 5-5 shows a schematic diagram of a CPW, which consists of a strip conductor of width, w , separated from two ground planes, fabricated on a dielectric substrate

with a relative permittivity, ϵ_r , and a thickness, h . As in microstrip lines, the major sources of losses are the dielectric loss in the substrate and the conductor loss in the strip conductor and ground planes. The attenuation constant (in Np/m) due to the dielectric loss is expressed as [112]:

$$\alpha_d = \frac{\pi}{\lambda_0} \frac{\epsilon_r}{\sqrt{\epsilon_{eff}}} q \tan \delta \quad (\text{A.4})$$

where λ_0 is the free space wavelength and q is the filling factor given by

$$q = \frac{1}{2} \frac{K(k_1)}{K(k'_1)} \frac{K(k')}{K(k)} \quad (\text{A.5})$$

where k , k_1 , and $K(k_1)/K(k)$ are given in (5.3) and (5.4), respectively. The attenuation constant due to conductor loss is given by [112]:

$$\alpha_c = \frac{R_c + R_s}{2Z_0} \quad (\text{A.6})$$

where Z_0 is the CPW characteristic impedance given in (5.5) and R_c is the series resistance (in Ω per unit length) of the center strip conductor and it is given by

$$R_c = \frac{R_s}{4G(1-k^2)K^2(k)} \left[\pi + \ln \left(\frac{4\pi G}{t} \right) - k \ln \left(\frac{1+k}{1-k} \right) \right] \quad (\text{A.7})$$

and R_g is the distributed series resistance (in Ω per unit length) of the ground planes and it is given by

$$R_g = \frac{kR_s}{4G(1-k^2)K^2(k)} \left[\pi + \ln \left(\frac{4\pi(G+2W)}{t} \right) - \frac{1}{k} \ln \left(\frac{1+k}{1-k} \right) \right] \quad (\text{A.8})$$

where R_s is the skin effect surface resistance (in Ω) given by

$$R_s = \frac{1}{\delta\sigma} \quad (\text{A.9})$$

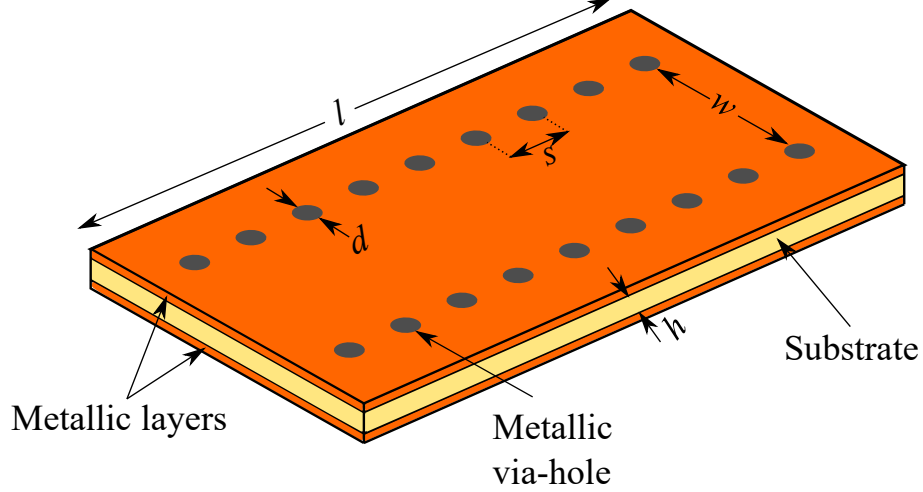


Figure A-3: A schematic diagram of a SIW structure.

where σ is the conductivity of the conductor (in Semens/m) and δ is the skin depth given by

$$\delta = \sqrt{\frac{2}{\omega\mu\sigma}} \quad (\text{A.10})$$

A schematic diagram of a SIW structure is shown in Figure A-3. As mentioned in Section 2.1, the SIW losses come from three main sources, namely, dielectric, conductor, and radiation losses. Thus, the total losses $\alpha_t = \alpha_d + \alpha_c + \alpha_r$. The attenuation constant due to dielectric loss is given by [90, 116]

$$\alpha_d = \frac{k_0^2 \tan \delta}{2\beta} \quad (\text{A.11})$$

where k_0 is the wave number in free space and it is given by $k_0 = \omega\sqrt{\mu_0\epsilon_0}$, $\tan \delta$ is the loss tangent of the dielectric substrate. The attenuation constant due to conductor loss is given by [90]:

$$\alpha_c = \frac{R_m}{w_{eff}\eta\sqrt{1 - \frac{k_c^2}{k_0^2}}} \left[\frac{w_{eff}}{h} + 2\frac{k_c^2}{k_0^2} \right] \quad (\text{A.12})$$

where $R_m = \sqrt{\omega\mu_0/2\sigma}$, $\eta = \sqrt{\mu_0/\epsilon_0\epsilon_r}$, and σ is the conductivity of the metal. Finally, a formula for calculating the SIW radiation loss is given by [117]:

$$\alpha_r = \frac{\frac{1}{w} \left(\frac{d}{w}\right)^{2.84} \left(\frac{s}{d} - 1\right)^{6.28}}{4.85 \sqrt{\left(\frac{2w}{\lambda}\right)^2 - 1}} \quad (\text{A.13})$$

As can be noted, α_r depends on the geometrical parameters of the SIW structure as well as the operating wavelength.

Appendix B

Quality Factor Calculations

Q-factor is one of the important parameters of microwave filters. High Q-factor resonators are crucial for high performance filters and other RF/microwave components. It is well-known the SIW resonator provides significantly higher unloaded Q-factor (Q_u) than its counterpart microstrip resonator.

The unloaded Q-factor (Q_u) of an SIW resonator can be found using the following equation [118]:

$$\frac{1}{Q_u} = \frac{1}{Q_l} + \frac{1}{Q_e} \quad (\text{B.1})$$

where Q_l is the loaded Q-factor of a resonator and is defined as:

$$Q_l = \frac{f_0}{\Delta f_{3dB}} \quad (\text{B.2})$$

where f_0 is the resonant frequency and Δf is the -3 dB bandwidth. Q_e in (B.1) refers to the external Q-factor, which is defined as a function of the insertion loss at the resonant frequency and Q_l :

$$Q_e = \frac{Q_l}{10^{-IL/20}} \quad (\text{B.3})$$